Theoretical and Experimental Study on Mechanical and Electrochemical Properties of Proton Conducting Oxides Originated from Hydration and Influence of Interfaces

藤﨑, 貴也

Doctoral Thesis

Theoretical and Experimental Study on Mechanical and Electrochemical Properties of

Proton Conducting Oxides Originated from Hydration and Influence of Interfaces

プロトン伝導性酸化物の水和に起因する

機械的・電気化学的特性と界面の影響に関する理論・実験研究

Takaya Fujisaki

Molecular and Material Science
Interdisciplinary Graduate School of Engineering Sciences
Kyushu University

March 2019

Table of Contents

-Composition of this Thesis-

This thesis consists of 6 chapters in total. 1st chapter firstly introduces the research field of solid state ionics. The solid state ionics is covering the research field of proton conducting oxides this thesis mainly focuses on. While introducing previous research, this chapter explains problems of proton conducting oxides from the viewpoints of defect equilibrium. In addition, the importance to investigate them from the atomic scale is shown to understand the properties. Furthermore, this chapter explains the necessity of density functional theory in first principle calculation which is the research mostly used.

In the 2nd chapter, to evaluate the physical properties of proton conducting oxides, this study especially performs the first principle calculations as research methods from chapters 3 to 5, and the details of the calculation method is theoretically introduced.

3rd chapter explains the results of the study on chemical expansion by hydration of proton conducting oxides. For proton conduction, hydration must take place in the oxide-ion vacancies in the proton conducting oxides. This chapter clarifies how Ce and Zr contribute to chemical expansion in proton conducting oxides by first principle calculation, thermogravimetric analysis and high temperature X-ray diffraction analysis.

4th chapter investigated why the hydration of proton conducting oxides takes place by first principles calculation. In fact, it is not well understood that the origin of water entering the oxide-ion vacancies with respect to the proton conducting oxides. Even though oxygen vacancies exist among many metal oxides, the hydration reaction does not take place in all of them. The study in this chapter pays attention to bulk Y doped $SrZrO_3$ and Y stabilized ZrO_2, which have oxide-ion vacancies. This research discusses the origin of hydration from the viewpoints of covalency between Zr-O and Ce-O.

In 5th chapter, it attempts to explain the effect of platinum nanoparticles in proton conducting oxides by first principles calculation. Recently, it has been reported that platinum nanoparticles precipitating in the proton conducting oxide affect electric conductivity. The effect of the interface between the platinum nanoparticles and a proton conducting oxide was investigated for the defect equilibrium of protons.

In 6th chapter, experimental investigations were conducted on anomalous electric conductivity observed in dry hydrogen.

This thesis has two topics in appendixes which are Appendix A and B. Firstly, Appendix A shows a social background for the energy supplying system combining renewable energy and hydrogen. The system is known as “hydrogen society” and it attracts attention to compensate the future depletion of fossil fuels. The research and development is divided into three parts, which are hydrogen production, hydrogen storage, and hydrogen utilization, respectively. This appendix exhaustively reviews the all three part.

Appendix B introduce a concept of “Green Paradox”. In recent years, the concept doubts on the idea that introducing renewable energy is not only extending the availability period of fossil fuels but also not directly discharging harmful substances into the atmosphere. According to the concept, the renewable energy introducing accelerates fossil fuels consumption and promotes the increase of harmful substances due to the consumption. Because the number of papers evaluating the Green Paradox is limited and evaluation method is not well established. This paper attempts to evaluate the Green Paradox in Japan following three indicators. The first is the electricity charge, the second is the introduction amount of renewable energy, and the third is the relocation amount of Japanese factories to other countries.

CHAPTER 1

Introduction

1-1 Solid state ionics

Some solid state materials can generate electric current of ions when they are exposed to applied field. Scientific fields for such materials are known as solid state ionics. The solid state ionics covers multidisciplinary fields including chemistry, physics and material science, which investigate ionic transport properties in ceramics, glasses, and so on[1-1]. In this century, the solid state ionics is emerged as one of the most attractive scientific fields for lots of useful technological applications. For example, they are fuel cells[1-2], batteries[1-3], redox flow batteries[1-4], capacitors[1-5], sensors or gas separation membranes[1-6]. The applied fields have been expanded to even information and communication field as seen in Figure 1-1. Many researchers have studied long time in the solid state ionic, and the ionic conduction originates in the discovery of the validity of Faraday's law. The ionic conductors were demonstrated by Warburg *et al.* in 1884 [1-7]. From the viewpoints of atomic scale, ionic conduction in solids is caused by the existence of defects in the solid bulk interior.

These defects are known as point defects and schottky defect. They are formed when oppositely charged ions leave their lattice sites, creating lattice vacancies in crystal structure as seen in Figure 1-2(a). In Kröger-Vink notation, this reaction to create their defects is described as

$$\text{Null} \leftrightarrows V_M^{//} + V_X^{\cdot\cdot} \tag{1-1}$$

, where Null is neutral charge, $V_M^{//}$ is $M(2+)$ vacancy, and $V_X^{\cdot\cdot}$ is $X(2-)$ vacancy. On the other hand, frenkel defect which is also one of the point defect is formed when an ion moves from a lattice point to an interstitial position, creating both a lattice vacancy and an interstitial ion as seen in Figure 1-2(b). In Kröger-Vink notation, this reaction can be described as

$$\text{Null} \leftrightarrows V_M^{//} + V_{\text{i}}^{\cdot\cdot} \quad (1\text{-}2).$$

, where $V_{\text{i}}^{\cdot\cdot}$ is vacancy on interstitial site.

The ionic diffusion mediated via vacancies is generally called as vacancy diffusion mechanism, and the diffusion of interstitial ions are categorized to interstitial diffusion mechanism. The theory of defect thermodynamics in solids was introduced by Joffé Frenkel. The researcher suggests that the concentrations of defects obey the laws of mass action being similar to those holding for dissociation equilibria in liquid electrolytes. In fact, the concept was taken over by Schottky and Wagner, and equilibrium thermodynamics of point defects and their diffusion kinetics in the bulk solids have been well studied and understood[1-8,1-9]. Through their concepts, the development of novel materials based on the fundamental theory described above has become a central concept of solid state ionics. Although schottky defect and frenkel defect are taking place in intrinsic semiconductors, to describe defect equilibria, they are the fundamental ideas.

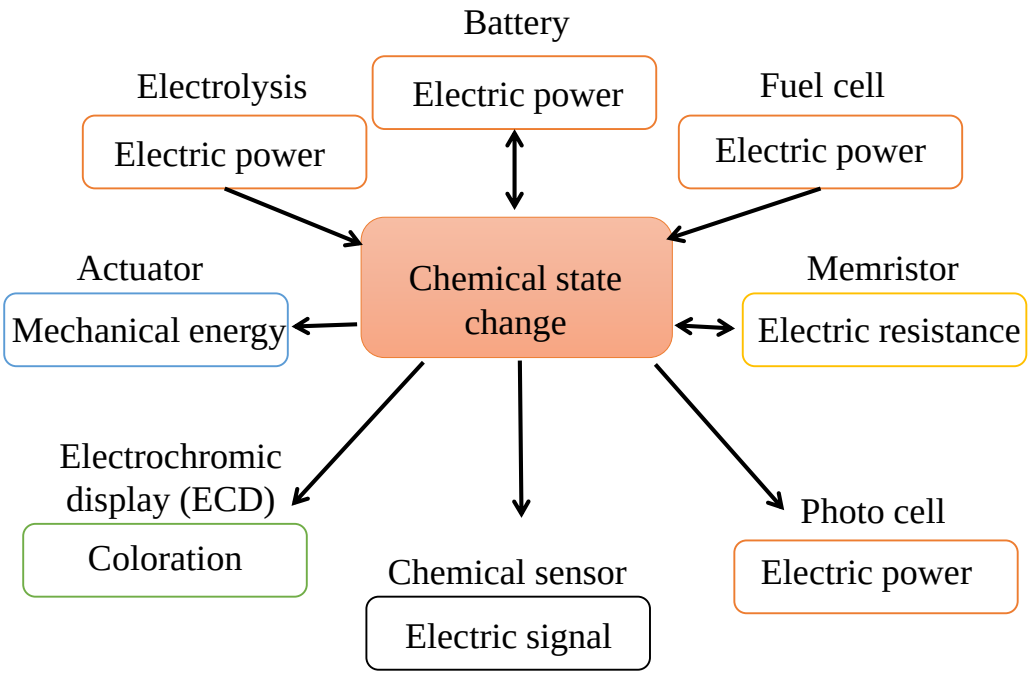

Figure 1-1. Various electrochemical devices with ion conductors. Each black arrow indicates the chemical energy flow.

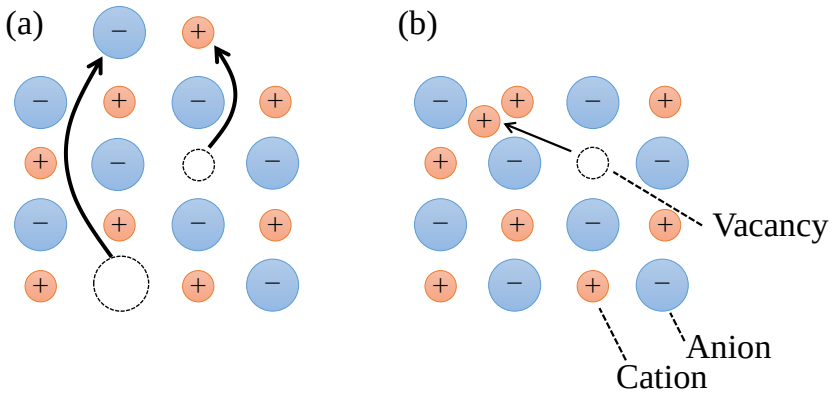

Figure 1-2 Schematic models of schottky defect (a) and frenkel defect (b)

1-2 Fuel cell for the research in solid state ionics

As one of the typical example using ionic conductors, it is suitable to introduce fuel cell for an application example. The fuel cell is a chemical power generation device for directly converting chemical energy produced by an electrochemical reaction of hydrogen and oxygen into electric energy. It was appeared in 1839 by W. Grove in the United Kingdom[1-10]. He demonstrated power generation through the reaction by combining hydrogen and oxygen with a battery using platinum for electrode, glove battery, and dilute sulfuric acid as an electrolyte [1-10]. Because the fuel cell does not undergo heat energy form during conversion process from chemical energy to electric energy, power generation efficiency is theoretically higher than conventional thermal power generation. Furthermore, because it is easy to downsize and can be dispersedly arranged in consuming areas, power transmission loss can be small, and very high energy utilization rate can be attained including the effective utilization of exhaust heat. When hydrogen is used for fuel, the exhaust stuff is mainly water, which provides low impact on the environment[1-11,12].

Because of such advantages, the fuel cell is an energy conversion device that can be applied to various utilization and scales ranging from mobile devices such as laptop computers and cellular phones to mobile bodies such as automobiles and trains. In fact, fuel cell has several types and solid oxide fuel cell (SOFCs) has the highest efficiency because it does not require complicated fuel reforming process [1-13]. The ionic conductors for the electrolyte are applied to two types, which are oxide ion conductors and proton conducting oxides, respectively. In both systems, hydrogen as the fuel and oxygen as oxidizing agent will be consumed by migration of conduction

species in the electrolyte. As shown in Figure 1-3 (a) and (b), the SOFCs (including most fuel cells) mainly consist of electrode for taking place reaction of fuel and oxidizer, and an electrolyte that conducts ions (oxide ions or protons) involved in the electrode reaction. The oxidizer and electrolyte for conducting ions involved in the electrode reaction are represented by an equivalent circuit as shown in the Figure 1-4. The voltage following nernst equation is determined by the Gibbs free energy change of equation (1-3). As seen in the equation (1-4), it shows the relationship between the partial pressure at anode and cathode when water partial pressure on both sides are consistent. The theoretical electromotive force (V_N) depends on the activity (partial pressure) of the reactive species, and the temperature. In addition, when the ionic transport number is 1, the theoretical electromotive force follows equation (1-4).

$$H_2 + 1/2\ O_2 \leftrightarrows H_2O \tag{1-3}$$

$$V_N = \frac{\Delta G^\circ}{2F} - \frac{\Delta G^\circ}{2F} \ln \frac{RT}{2F} \ln \frac{pH_2O}{pH_2 \cdot (pO_2)^2} \tag{1-4}$$

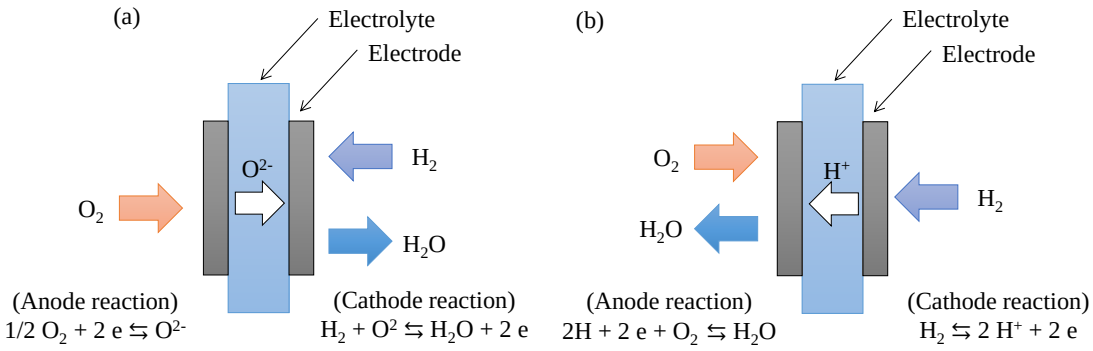

Figure 1-3 Solid oxide fuel cells with oxide ion conductor (a) and proton conducting oxides (b). In those figures, resistance and electrical wires are intentionally removed.

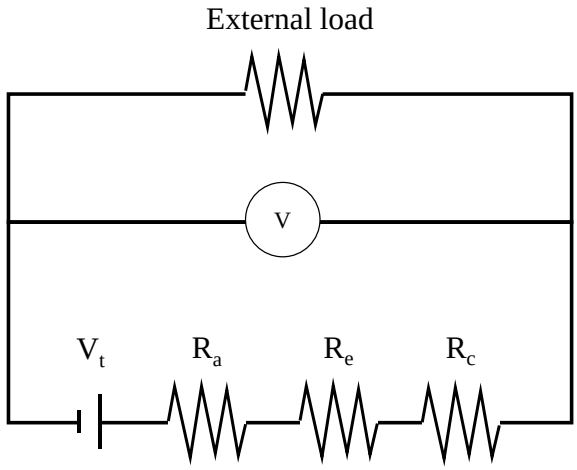

Figure 1-4 Equilibrium circuit of fuel cell. V_t: Open circuit voltage following nernst equation, R_a: resistance of anode, R_e: resistance of electrolyte, R_c: resistance of cathode.

1-3 Solid oxide fuel cells and proton conducting oxides

In addition to the explanation in previous section, SOFCs using oxide ion conductors for electrolyte as shown in Figure 1-3(a) has high energy conversion efficiency and lots of research has been actively carried out because SOFCs have advantage that a precious metal catalyst such as platinum is not required. By contrast, however, it is necessary for the structural components to have high heat resistance due to the high operating temperature of 700-1000 ℃. In addition, such high operation temperature is accompanied by coarsening of particles of the electrode[1-14–16], undesirable element diffusion between crystal phases, formation of large resistance layer by chemical reaction [1-17–20], Cr poisoning [1-21–23], and causing problems of stability over a long period of time. To solve those problems simultaneously, it is essential to have SOFCs operate in lower temperature. To reduce the operating temperature, ionic conductivity of the electrolyte

should be considered firstly. Figure 1-5 shows the temperature dependence of the ionic conductivity of a representative oxide ion conducting oxides and proton conducting oxides [1-24–30].

When a solid electrolyte is used for a device including SOFCs that needs to flow large current, the target value of ionic conductivity is 10^{-2} Scm^{-1} or more [1-13]. One candidate composition which is close to the requirement is yttrium stabilized zirconia (YSZ). The electrolyte with zirconia of parent crystal has high oxide ion conductivity and stability. Then, YSZ becomes the most industrially utilized ionic conductors in SOFCs. However, the ion conductivity rapidly decreases with reducing temperature which is especially lower than 600 ℃, and it becomes difficult to apply to SOFCs having lower operating temperature with YSZ. On the other hand, ceria-based and lanthanum-gallate-based electrolytes has relatively higher oxide ion conductivity that can be used as an electrolyte even in the middle temperature range of 500-750 ℃. However, the ceria-based electrolyte has a problem that oxide-ion transport number is dramatically decreasing in a reducing atmosphere such as hydrogen of fuel [1-31–33]. In addition, with respect to the lanthanum gallate type electrolyte, gallium oxide in the phase easily undergoes volatilization and reduction in the reducing atmosphere. Their phenomena lead to the appearance of the secondary phase and electron conduction [1-34–36].

The oxide ion conductivity as described above drops greatly with decreasing temperature and it is difficult to use them in lower temperature. On the other hand, proton conducting oxides have relatively lower activation energy in comparison with oxide ions conductors. They are not significantly affected by reducing atmosphere lower operating temperature in comparison with oxide ion conductors. Among proton conducting oxides, Y-doped $BaZrO_3$ and $BaCeO_3$ exhibit sufficiently high ionic conductivity in the middle

temperature range between approximately 500 ℃ to 700 ℃.

In recent years, proton conducting ceramic fuel cell (PCFC) using proton conducting oxides for electrolyte has attracted attention as novel fuel cell. In addition to the relatively high ionic conductivity at low temperatures, when the oxide ion conductors are used for the electrolyte, the water vapor formation reaction proceeds on the cathode side as shown in Figure 1-3 (a). In the fuel cell using the oxide ion conductors, since the generation of water vapor proceeds on the cathode side, the fuel (H_2) is diluted with water vapor. On the other hand, when the proton conducting oxides are used for the electrolyte as shown in Figure 1-3 (b), fuel dilution does not take place. In addition, there is an advantage that hydrogen containing no water vapor can be obtained even when hydrogen is produced by steam electrolysis.

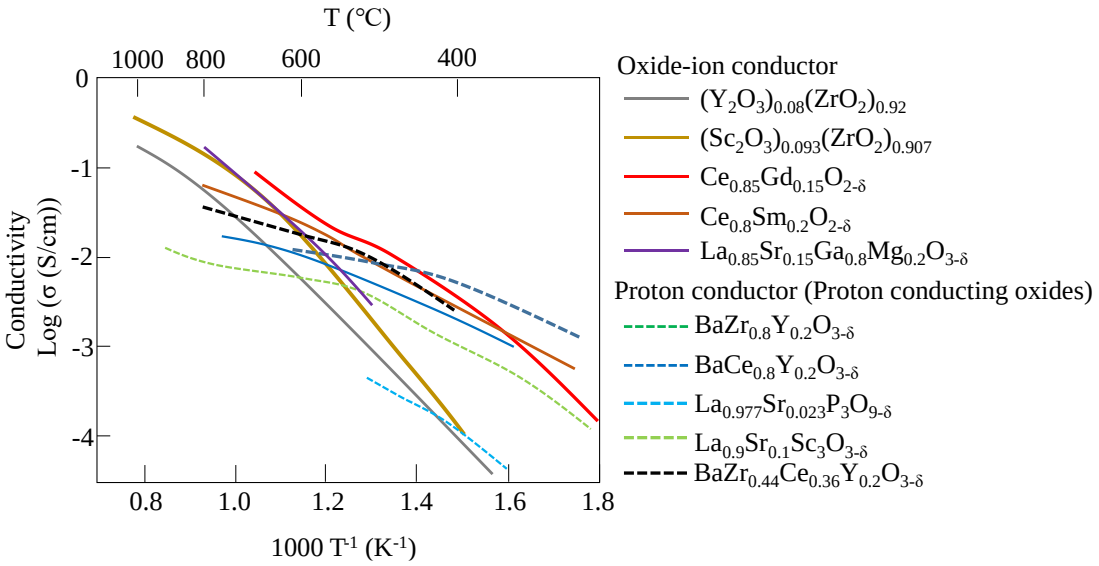

Figure 1-5 Conductivity of typical oxide-ion conductor and proton conductor.

$(Y_2O_3)_{0.08}(ZrO_2)_{0.92}$ [1-30], $(Sc_2O_3)_{0.093}(ZrO_2)_{0.907}$ [1-29], $Ce_{0.85}Gd_{0.15}O_{2-\delta}$ [1-28], $Ce_{0.8}Sm_{0.2}O_{2-\delta}$ [1-27], $La_{0.85}Sr_{0.15}Ga_{0.8}Mg_{0.2}O_{3-\delta}$ [1-26],$BaZr_{0.8}Y_{0.2}O_{3-\delta}$[1-37], $BaCe_{0.8}Y_{0.2}O_{3-\delta}$ [1-25], $La_{0.977}Sr_{0.023}P_3O_{9-\delta}$ [1-24], $La_{0.9}Sr_{0.1}Sc_3O_{3-\delta}$ [1-38], $BaZr_{0.44}Ce_{0.36}Y_{0.2}O_{3-\delta}$ [1-39].

1.4 Proton conduction by hydration and ion probability by oxygen partial pressure

Since high proton conduction of $SrCeO_3$ doped with acceptor has been reported by Iwahara *et al.* in 1981, perovskite type oxides of various compositions showing proton conductivity have been studied [1-40,41]. As shown in Figure 1-6, in the perovskite type oxide, oxide ions occupy each apex position of the unit lattice as cation *A*, body position as cation *B*, and face center position as oxide ion. Here, the site of cation *A* is referred to as *A* site, and the site of cation *B* is referred to as *B* site.

This structure is stable with many complex oxides, and it is significantly stable especially when the sum of the valences of *A* site and *B* site is +6. In short, I-V type $KNbO_3$ having K(1+) at *A* site and Nb(5+) at *B* site, $BaZrO_3$, La(3+) of II - IV type of combination of Ba(2+) and Zr (4+), and $LaGaO_3$ of III - III type of the combination are especially stable. Here, *A* site has 12 coordination and the *B* site has 6 coordination, respectively. The cation having the larger ionic radius enters the *A* site having wider space, and the cation having a smaller ionic radius enters the *B* site having narrow space. This structure can generate oxygen vacancies by permitting the nonstoichiometry of oxygen to some extent and replacing the cation in the lattice with a cation of a lower valence number. For example, when tetravalent Zr site in $BaZrO_3$ is substituted with trivalent Y, it is represented by the following equation.

$$2\,Zr_{Zr}^{X} + Y_2O_3 + O_O^{X} \leftrightarrows 2Y_{Zr}^{/} + 2ZrO_2 + V_O^{\cdot\cdot} \qquad (1\text{-}5)$$

Furthermore, hydration introduces protons as shown in the following formula.

$$H_2O + V_O^{\cdot\cdot} \leftrightarrows 2H_i^{\cdot} + O_O^{X} \qquad (1\text{-}6)$$

Equation (1-5) and (1-6) use Kröger-Vink notation. As seen in equation (1-6), proton enters a stable position around oxygen in the lattice, and migrates under electric field by

rotating or hopping between stable positions [1-42,1-43]. Y doped $BaZrO_3$ ($BaZr_{1-x}Y_xO_{3-\delta}$, BZY) and $BaCeO_3$ ($BaCe_{1-x}Y_xO_{3-\delta}$, BCY) among the various perovskite structure proton conductors show particularly high proton conductivity as shown in Figure 1-5. It has sufficient proton conductivity as an electrolyte material for fuel cells in the medium temperature range. Such solid solution which is described as $BaZr_xCe_{1-x-y}Y_yO_{3-\delta}$ (BZCY) has intermediate properties between BZY and BCY, and it is promising electrolyte candidates due to high conductivity and stability.

Regarding the composition dependence of proton conductivity in rare earth element-doped $BaZrO_3$ and $BaCeO_3$, Wiensträger *et al.* investigated Nd in 1997 [1-44], and Ryu *et al.* investigated Nd and Gd as dopants in 1999 [1-45]. They confirmed that the conductivity decreases as the proportion of Zr increases with any dopants. In the case of using Y as a dopant, Katahira *et al.* reported the proton conductivity of $BaZr_{0.9}Y_{0.1}O_{3-\delta}$(BZY10) and $BaCe_{0.9}Y_{0.1}O_{3-\delta}$(BCY10) and their solid solution which is $BaZr_xCe_{0.9-x}Y_{0.1}O_{3-\delta}$in 2000 [1-45]. BCY10 exhibits high proton conductivity of at least 0.01 Scm^{-1} at 600 ℃, whereas the conductivity decreases as the proportion of Zr increased, and the proton conductivity of BZY 10 was smaller than that of BCY10 by one order of magnitude.

They discussed that the reason why the conductivity of $BaZrO_3$ system is lower than that of $BaCeO_3$ is that large grain boundary resistance is generated due to poor sinterability and small grain size. However, as a result of further improvements in the sintering process and search for sintering aids to be described later in the subsequent research, it is possible to obtain a sintered body having a large particle, so that high proton conductivity has gradually reported. Although some reports that Y doped $BaZrO_3$ prepared by pulsed laser deposition (PLD) has higher proton conductivity than

conventional sintering process, it is still commonly recognized that Y doped $BaCeO_3$ has higher proton conductivity than Y doped $BaZrO_3$ [1-46–51].

Although Y doped $BaCeO_3$ has higher proton conductivity than Y doped $BaZrO_3$, in fact, Y doped $BaCeO_3$ has a problem regarding stability. When comparing them in terms of stability, Y doped $BaCeO_3$ tends to relatively easily react with water vapor and carbon dioxide as compared with Y doped $BaZrO_3$. Figure 1-7 and Figure 1-8 show the standard gibbs free energy change of reactions in which $BaZrO_3$ and $BaCeO_3$ react with H_2O or CO_2. In both reactions, the free energy change of $BaCeO_3$ decomposition is smaller than the free energy change of $BaZrO_3$ decomposition, then $BaCeO_3$ is more unstable than $BaZrO_3$ for both reactions [1-52,53]. Thus thermodynamically there is a problem with stability in BZY rather than BCY [1-54].

On the other hand, sinterability of BZY is a problem in comparison with BCY. To obtain dense electrolyte membrane having a large particle size, the required sintering temperature generally becomes high. Such high sintering temperature provides several problems including the cost of sintering process. Even focusing on the electrolyte itself, proton conductivity, transport number and phase stability due to volatilization of Ba become worse. Furthermore, in the case of co-sintering with the electrode and electrolyte, it cannot be ignored for inter-diffusion of constituent elements, reaction product, and thermal stress caused by difference in thermal expansion coefficient. To improve sinterability, there are two procedures for improvement of BZY synthesis process and addition of sintering aid.

Focusing on the process of synthesis, synthesis of BZY has been conventionally carried out by solid phase reaction method. However, in this method, the temperature required for the synthesis tends to become high because the degree of mixing powders is

insufficient and lots of coarse particles are remained. In recent years, to reduce the temperature required for this synthesis process, novel sintering process are actively adopted such as sol-gel method [1-55–58], combustion synthesis method [1-59,60], precipitation method [1-61], freeze drying method [1-62].

Powders before sintering process can be uniformly mixed through these liquid phase synthesis methods, in comparison with the solid state reaction method. Then, Y doped $BaZrO_3$ powders for sintering can be obtained with relatively lower heat. The sinterability can be improved as compared with the powder prepared by the solid state reaction method. In addition, it has also been reported that sinterability of Y doped $BaZrO_3$ improves by adding NiO, CuO, or ZnO as a sintering aid [1-63–65]. As mentioned above, Y doped $BaZrO_3$ and Y doped $BaCeO_3$ as typical examples of proton conducting oxides have advantages and disadvantages. Therefore, BZCY combining both BCY and BZY to take advantage of both compositions is considered as a few candidates for PCFC electrolyte.

It has been explained about the proton conductivity and stability of the proton conducting oxides with BCY and BZY. Furthermore, as a point to be considered for proton conducting oxides, this session introduces the reduction of proton transport number by oxygen partial pressure. Although BZY and BCY show such high proton conductivity, it has also been reported that oxygen enters the oxygen vacancies in enough oxygen partial pressure and shows hole conductivity as shown in the following equation:

$$V_O^{\cdot\cdot} + 1/2\ O_2 \leftrightarrows h^{\cdot} + O_O^{X} \qquad (1\text{-}7).$$

On the other hand, oxygen goes out of oxygen site and this phenomenon leads to electron conduction following equation:

$$O_O^{X} \leftrightarrows 1/2\ O_2 + V_O^{\cdot\cdot} + 2\ h^{\cdot} \qquad (1\text{-}8).$$

Somekawa *et al.* reported the oxygen partial pressure dependence of electron conductivity and hole conductivity [1-66]. In addition, under reducing atmosphere, Y doped $BaCeO_3$ shows electron conductivity with reduction of Ce following equation [1-48–50].

$$Ce_{Ce}^{X} + e^{/} \leftrightarrows Ce_{Ce}^{/} \quad (1\text{-}9)$$

When the ion transport rate of the electrolyte in the fuel cell decreases, electron current (leakage current) flows in the electrolyte, resulting in decrease in the electromotive force and also decrease in the fuel utilization rate. In an actual cell, one of the electrolyte (fuel electrode side) is exposed to a reducing atmosphere (H_2) and the another side (oxygen electrode side) is exposed to an oxidizing atmosphere (O_2). When the interior of the electrolyte is thick enough and has a high ion transport number, the interior becomes a blocking layer against electron conduction and leakage current. However, when the thickness of electrolyte is decreased a lot to reduce the resistance or the conductivity of holes and electrons is increased sufficiently, the influence of leakage current becomes remarkable [1-47].

For this reason, attention should be paid to the ion transport number of the electrolyte, especially if it is considered to utilize the cell for electrolysis hydrogen production. Also, when conducting measurements using symmetric cells to evaluate electrode performance, it is difficult to properly evaluate electrode performance due to leakage current if the ion transport number is low [1-46].

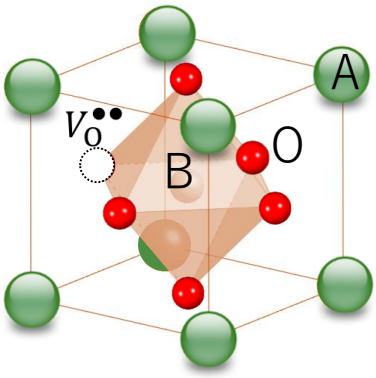

Figure 1-6 Perovskite structure of proton conducting oxides (ABO_3)

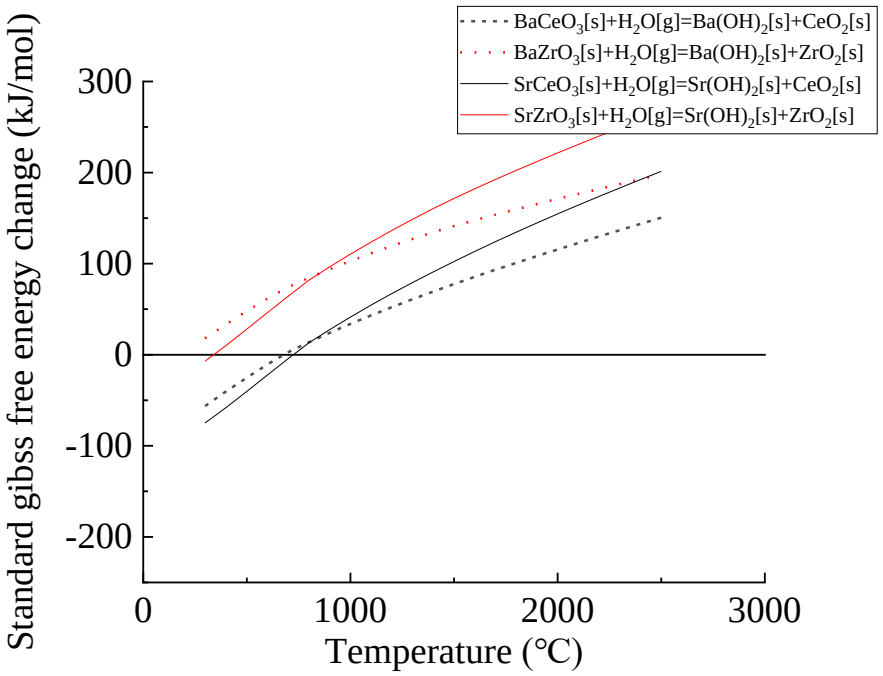

Figure 1-7 Gibbs energy change of hydrolysis reaction of $BaZrO_3$ and $BaCeO_3$ at $p(H_2O) = 0.03$ atm. [1-52]

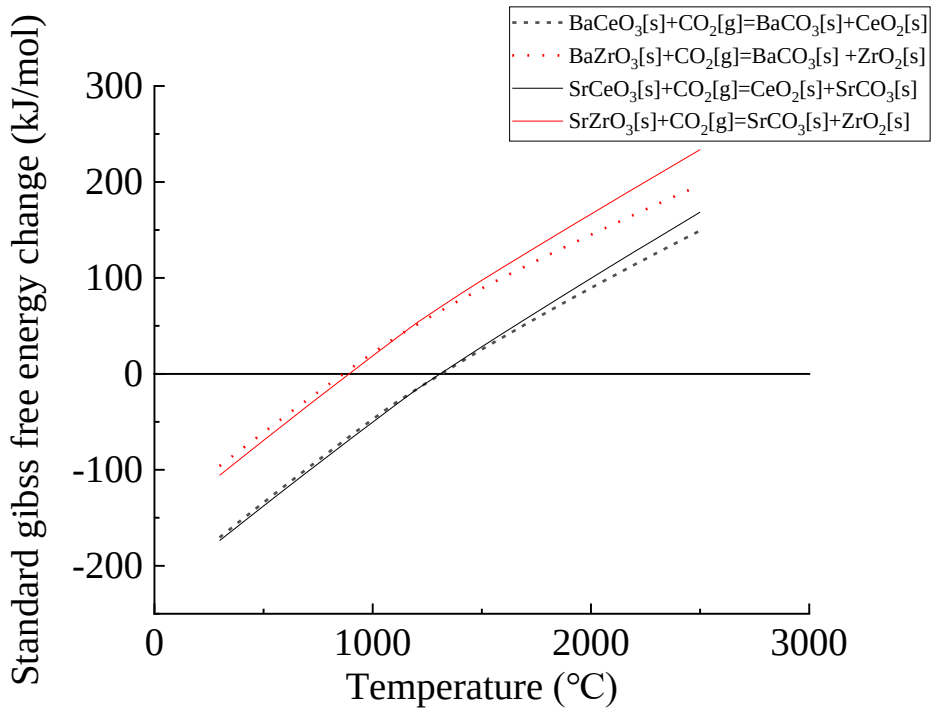

Figure 1-8 Gibbs energy change of the reaction of $BaZrO_3$ and $BaCeO_3$ to decompose into carbonate at $p(CO_2) = 3.7 \times 10^{-4}$ atm [1-52,53].

1-5 Computational approach

Previous sections have mainly explained chemical stability, ion conductivity, and proton transport number showing typical proton conducting oxides. To improve them, it is important to understand the proton conducting oxides from the viewpoints of atomic scale. However, experimental approach is still limited because of advanced experimental technique to be managed. On the other hand, it is significantly useful to apply computational approach. Because of remarkable development of computer performance in recent years, computational science has provided satisfactory results to many researchers. This also applies to proton conducting oxides, and many research results have been reported. For example, Jing *et al.* showed that proton conducting oxides becomes stable after hydration by density functional theory (DFT)[1-67]. In addition, Marco *et al.* clarified the movement mechanism of protons[1-68]. Especially, in the previous section, the proton conducting oxides are susceptible to defect equilibrium in oxygen partial pressure and reducing atmosphere. This research mainly attempts to understand these defect equilibria from atomic scale using DFT for proton conducting oxides.

Reference

(1-1) C. S. Sunandana. *Introduction to Solid State Ionics: Phenomenology and Applications*. *Sedimentary Geology* (CRC Press, 2015).

(1-2) Norby, T. Solid-state protonic conductors: Principles, properties, progress and prospects. *Solid State Ionics* **125,** 1–11 (1999).

(1-3) Armand, M. & Tarascon, J.-M. Building better batteries. *Nature* **451,** 652–657 (2008).

(1-4) Alotto, P., Guarnieri, M. & Moro, F. Redox flow batteries for the storage of renewable energy: A review. *Renew. Sustain. Energy Rev.* **29,** 325–335 (2014).

(1-5) Sharma, P. & Bhatti, T. S. A review on electrochemical double-layer capacitors. *Energy Convers. Manag.* **51,** 2901–2912 (2010).

(1-6) Yampolskii, Y. Polymeric gas separation membranes. *Macromolecules* **45,** 3298–3311 (2012).

(1-7) Tuller, H. L. & Barsoum, M. W. Glass solid electrolytes: Past, present and near future - the year 2004. *J. Non. Cryst. Solids* **73,** 331–350 (1985).

(1-8) Gordon, W. Zur Lichtfortpflanzung nach der Relativitätstheorie. *Ann. Phys.* **377,** 421–456 (1923).

(1-9) Frenkel, J. Über die Wärmebewegung in festen und flüssigen Körpern. *Zeitschrift für Phys.* **35,** 652–669 (1926).

(1-10) Grove, W. R. XXIV. On voltaic series and the combination of gases by platinum. *Philos. Mag. Ser. 3* **14,** 127–130 (1839).

(1-11) Winter, M. & Brodd, R. J. What Are Batteries, Fuel Cells, and Supercapacitors? *Chem. Rev.* **104,** 4245–4270 (2004).

(1-12) Kirubakaran, A., Jain, S. & Nema, R. K. A review on fuel cell technologies and power electronic interface. *Renew. Sustain. Energy Rev.* **13,** 2430–2440 (2009).

(1-13) Steele, B. C. H. & Heinzel, A. Materials for fuel-cell technologies. *Nature* **414,** 345–352 (2001).

(1-14) Iwata, T. Characterization of Ni-YSZ Anode Degradation for Substrate-Type Solid Oxide Fuel Cells. *J. Electrochem. Soc.* **143,** 1521 (1996).

(1-15) Simwonis, D. Nickel coarsening in annealed Ni/8YSZ anode substrates for solid oxide fuel cells. *Solid State Ionics* **132,** 241–251 (2000).

(1-16) Dótor-Almazán, A., Armienta-Hernández, M. A., Talavera-Mendoza, O. & Ruiz, J. Geochemical behavior of Cu and sulfur isotopes in the tropical mining region of Taxco, Guerrero (southern Mexico). *Chem. Geol.* **471,** 1–12 (2017).

(1-17) Mai, A. *et al.* Time-dependent performance of mixed-conducting SOFC cathodes. *Solid State Ionics* **177,** 1965–1968 (2006).

(1-18) Im, D. J., Buchman, E. & Taylor, G. W. Understanding Minimum Probability Flow for RBMs Under Various Kinds of Dynamics. 581–610 (2014). doi:10.1146/annurev.matsci.33.022802.093856

(1-19) Mitterdorfer, A. & Gauckler, L. J. La2 Zr2 O7 formation and oxygen reduction kinetics of the La Sr Mn O3 , O2 (g)YSZ system. *Solid State Ionics* **111,** 185–218 (1998).

(1-20) Kawada, T., Sakai, N., Yokokawa, H. & Dokiya, M. Electrical properties of transition-metal-doped YSZ. *Solid State Ionics* **53–56,** 418–425 (1992).

(1-21) Jiang, S. P. & Chen, X. Chromium deposition and poisoning of cathodes of solid oxide fuel cells - A review. *Int. J. Hydrogen Energy* **39,** 505–531 (2014).

(1-22) Yokokawa, H. *et al.* Thermodynamic considerations on Cr poisoning in SOFC

cathodes. *Solid State Ionics* **177,** 3193–3198 (2006).

(1-23) Hilpert, K. Chromium Vapor Species over Solid Oxide Fuel Cell Interconnect Materials and Their Potential for Degradation Processes. *J. Electrochem. Soc.* **143,** 3642 (1996).

(1-24) Hatada, N., Toyoura, K., Onishi, T., Adachi, Y. & Uda, T. Fast and anisotropic proton conduction in a crystalline polyphosphate. *J. Phys. Chem. C* **118,** 29629–29635 (2014).

(1-25) Fabbri, E. *et al.* Design and fabrication of a chemically-stable proton conductor bilayer electrolyte for intermediate temperature solid oxide fuel cells (IT-SOFCs). *Energy Environ. Sci.* **1,** 355–359 (2008).

(1-26) Liu, N. *et al.* Microstructure and ionic conductivity of Sr- and Mg-doped LaGaO3. *J. Mater. Sci.* **41,** 4205–4213 (2006).

(1-27) Zheng, Y. *et al.* Effect of Fe2O3 on Sm-doped ceria system solid electrolyte for IT-SOFCs. *J. Alloys Compd.* **509,** 546–550 (2011).

(1-28) Zajac, W. & Molenda, J. Electrical conductivity of doubly doped ceria. *Solid State Ionics* **179,** 154–158 (2008).

(1-29) Badwal, S. P. S., Ciacchi, F. T. & Milosevic, D. Scandia-zirconia electrolytes for intermediate temperature solid oxide fuel cell operation. *Solid State Ionics* **136–137,** 91–99 (2000).

(1-30) Kwon, O. H. & Choi, G. M. Electrical conductivity of thick film YSZ. *Solid State Ionics* **177,** 3057–3062 (2006).

(1-31) Dalslet, B. *et al.* Assessment of doped ceria as electrolyte. *J. Solid State Electrochem.* **10,** 547–561 (2006).

(1-32) Wang, S., Kobayashi, T., Dokiya, M. & Hashimoto, T. Electrical and Ionic

Conductivity of Gd-Doped Ceria. *J. Electrochem. Soc.* **147,** 3606 (2000).

(1-33) EGUCHI, K., SETOGUCHI, T., INOUE, T. & ARAI, H. Electrical properties of ceria-based oxides and their application to solid oxide fuel cells. *Solid State Ionics* **52,** 165–172 (1992).

(1-34) Yamaji, K., Horita, T., Ishikawa, M., Sakai, N. & Yokokawa, H. Chemical stability of the La Sr Ga Mg O electrolyte in a reducing atmosphere. *Solid State Ionics* **121,** 217–224 (1999).

(1-35) Stevenson, J. Effect of A-site cation nonstoichiometry on the properties of doped lanthanum gallate. *Solid State Ionics* **113–115,** 571–583 (1998).

(1-36) Djurado, E. & Labeau, M. Second phases in doped lanthanum gallate perovskites. *J. Eur. Ceram. Soc.* **18,** 1397–1404 (1998).

(1-37) Han, D., Hatada, N., Uda, T. & Koc, R. Chemical Expansion of Yttrium-Doped Barium Zirconate and Correlation with Proton Concentration and Conductivity. *J. Am. Ceram. Soc.* **99,** 3745–3753 (2016).

(1-38) Okuyama, Y. *et al.* Incorporation and conduction of proton in Sr-doped LaMO3(M=Al, Sc, In, Yb, Y). *Electrochim. Acta* **125,** 443–449 (2014).

(1-39) Leonard, K. *et al.* Efficient intermediate-temperature steam electrolysis with Y : $SrZrO_3$ –$SrCeO_3$ and Y : $BaZrO_3$ –$BaCeO_3$ proton conducting perovskites. *J. Mater. Chem. A* 19113–19124 (2018). doi:10.1039/C8TA04019B

(1-40) Iwahara, H., Esaka, T., Uchida, H. & Maeda, N. Proton conduction in sintered oxides and its application to steam electrolysis for hydrogen production. *Solid State Ionics* **3–4,** 359–363 (1981).

(1-41) Kreuer, K. D. Proton-Conducting Oxides. *Annu. Rev. Mater. Res.* **33,** 333–359 (2003).

(1-42. Kreuer, K. D. Proton conductivity: Materials and applications. *Chem. Mater.* **8,** 610–641 (1996).

(1-43) Yamazaki, Y. *et al.* Proton trapping in yttrium-doped barium zirconate. *Nat. Mater.* **12,** 647–651 (2013).

(1-44) WIENSTROER, S. Investigation of the influence of zirconium substitution on the properties of neodymium-doped barium cerates. *Solid State Ionics* **101–103,** 1113–1117 (1997).

(1-45) Saftlas, A. F., Olson, D. R., Franks, A. L., Atrash, H. K. & Pokras, R. Epidemiology of preeclampsia and eclampsia in the United States, 1979-1986. *Am. J. Obstet. Gynecol.* **163,** 460–465 (1990).

(1-46) Poetzsch, D., Merkle, R. & Maier, J. Investigation of oxygen exchange kinetics in proton-conducting ceramic fuel cells: Effect of electronic leakage current using symmetric cells. *J. Power Sources* **242,** 784–789 (2013).

(1-47) Dippon, M., Babiniec, S. M., Ding, H., Ricote, S. & Sullivan, N. P. Exploring electronic conduction through BaCexZr0.9-xY0.1O3-dproton-conducting ceramics. *Solid State Ionics* **286,** 117–121 (2016).

(1-48) Jung, M. G., Kim, Y. J., Jung, Y. G. & Lim, H. T. Measurement of hydrogen and oxygen chemical potential in yttria doped barium cerate (BCY) electrolyte of anode-supported protonic ceramic fuel cells. *Int. J. Hydrogen Energy* **39,** 16576–16584 (2014).

(1-49) Tomita, A. *et al.* Chemical and redox stabilities of a solid oxide fuel cell with BaCe0.8Y0.2O3-α functioning as an electrolyte and as an anode. *Solid State Ionics* **177,** 2951–2956 (2006).

(1-50) Bonanos, N. Transport properties and conduction mechanism in high-temperature

protonic conductors. *Solid State Ionics* **53–56,** 967–974 (1992).

(1-51) Han, D. *et al.* Transport properties of acceptor-doped barium zirconate by electromotive force measurements. *Int. J. Hydrogen Energy* **41,** 14897–14908 (2016).

(1-52) Shin, I. Electrical Conductivity of Grain Boundary in Accepter Doped Barium Zirconate. (Kyoto University, 2009). doi:10.14989/doctor.k14574

(1-53) Matsumoto, H. *et al.* Hydrogen separation from syngas using high-temperature proton conductors. *Ionics (Kiel).* **13,** 93–99 (2007).

(1-54) Katahira, K., Kohchi, Y., Shimura, T. & Iwahara, H. Protonic conduction in Zr-substituted BaCeO3. *Solid State Ionics* **138,** 91–98 (2000).

(1-55) Magrez, A. & Schober, T. Preparation, sintering, and water incorporation of proton conducting Ba0.99Zr0.8Y0.2O3-δ: Comparison between three different synthesis techniques. *Solid State Ionics* **175,** 585–588 (2004).

(1-56) Yamazaki, Y., Hernandez-Sanchez, R. & Haile, S. M. High total proton conductivity in large-grained yttrium-doped barium zirconate. *Chem. Mater.* **21,** 2755–2762 (2009).

(1-57) Taglieri, G., Tersigni, M., Villa, P. L. & Mondelli, C. Synthesis by the citrate route and characterisation of BaZrO3, a high tech ceramic oxide: Preliminary results. *Int. J. Inorg. Mater.* **1,** 103–110 (1999).

(1-58) Veith, M. *et al.* Sol-Gel Synthesis of Nano-Scaled BaTiO3, BaZrO3 and BaTi0.5Zr0.5O3 Oxides via Single-Source Alkoxide Precursors and Semi-Alkoxide Routes. *J. Sol-Gel Sci. Technol.* **158,** 145–158 (2000).

(1-59) Kumar, H. P. *et al.* Characterization and sintering of BaZrO3nanoparticles synthesized through a single-step combustion process. *J. Alloys Compd.* **458,**

528–531 (2008).

(1-60) Sun, Z., Fabbri, E., Bi, L. & Traversa, E. Lowering grain boundary resistance of BaZr0.8Y0.2O3-δwith LiNO3sintering-aid improves proton conductivity for fuel cell operation. *Phys. Chem. Chem. Phys.* **13,** 7692–7700 (2011).

(1-61) Boschini, F., Rulmont, A., Cloots, R. & Vertruyen, B. Rapid synthesis of submicron crystalline barium zirconate BaZrO3 by precipitation in aqueous basic solution below 100 °C. *J. Eur. Ceram. Soc.* **29,** 1457–1462 (2009).

(1-62) Imashuku, S., Uda, T., Nose, Y. & Awakura, Y. Fabrication and electrical characterization of 15% yttrium-doped barium zirconate - Nitrate freeze drying method combined with vacuum heating. *J. Alloys Compd.* **509,** 3872–3879 (2011).

(1-63) Babilo, P. & Haile, S. M. Enhanced sintering of yttrium-doped barium zirconate by addition of ZnO. *J. Am. Ceram. Soc.* **88,** 2362–2368 (2005).

(1-64) Tao, S. & Irvine, J. T. S. A stable, easily sintered proton-conducting oxide electrolyte for moderate-temperature fuel cells and electrolyzers. *Adv. Mater.* **18,** 1581–1584 (2006).

(1-65) Park, K. Y. *et al.* Enhanced proton conductivity of yttrium-doped barium zirconate with sinterability in protonic ceramic fuel cells. *J. Alloys Compd.* **639,** 435–444 (2015).

(1-66) Somekawa, T. *et al.* Physicochemical properties of Ba(Zr,Ce)O3-Δ-based proton-conducting electrolytes for solid oxide fuel cells in terms of chemical stability and electrochemical performance. *Int. J. Hydrogen Energy* **42,** 16722–16730 (2017).

(1-67) Jing, Y., Matsumoto, H. & Aluru, N. R. Mechanistic Insights into Hydration of

Solid Oxides. *Chem. Mater.* **30,** 138–144 (2018).

(1-68) Fronzi, M., Tateyama, Y., Marzari, N. & Traversa, E. First-principles molecular dynamics simulations of proton diffusion in cubic BaZrO3 perovskite under strain conditions. *Mater. Renew. Sustain. Energy* **5,** 1–10 (2013).

CHAPTER 2

Theory and Computational Methods

In this chapter, theory of computational chemistry is explained to investigate physical properties of proton conducting oxides in following chapters. The computational chemistry has rapidly emerged as a new practical and robust branch of chemistry to describe the structure and properties of a system [2-1,2-2]. Quantum chemical calculations play an important role addressing real-world research problems as they can supplement experimental results to uncover and explore new physical/chemical properties [2-3]. The evolution of the approximations in quantum theory can reduce calculation time. In addition, advances in computer hardware and user-friendly software made quantum chemical calculations legitimate and indispensable part of material science. However, the mathematical equations used in the application of quantum mechanics and describing material properties are still not enough to clarify entire materials. It is because the entire field of computational chemistry is built with approximate solutions to those equations. Although some of solution methods are very crude, yielding quantitative and valuable insights require computational expensiveness. Some calculation is expected to be more rigorous than any experiment ever conducted, which leads to requiring extremely long computation time. In short, no method of calculation is likely to be ideal for all applications. Hence, the ultimate choice rests on a suitable level of theory for the system to be studied with a reasonable computational cost [2-1,2-4]. As a prominent example, density functional theory (DFT) method has been developed and evolved as an effective tool to describe the structure and properties of materials at the atomic scale. The main idea of DFT is to solve the many-particle Schrödinger equation by replacing the complete electron wavefunction with much simpler ground-state electron density [2-5]. Using the electron density as the fundamental variable for the description of the energies of electronic systems started soon after the introduction of the Schrödinger equation as its solution was beyond reach in most cases [2-3,2-10]. Hohenberg and Kohn's work [2-11] complemented by Kohn and Sham research [2-12] demonstrated that the electron density of a fully interacting system could be approximated from simple one-electron theory. For decades, due to the contribution of different researchers, DFT slowly gathered momentum and improved to the point to be implemented and commercially available in different codes to be

applied in a large number of research areas such as material science, biochemistry, chemistry, physics, nano-systems, and devices.

In this chapter, the theoretical backgrounds of the DFT method are presented from the advent of quantum mechanics to the correction/approximations that led to the widespread application of DFT.

2-1 Quantum mechanics

The quantum mechanics can theoritically predict properties of any systems composed of a number of nuclei and electrons interacting with each other. Formally the Hamiltonian of such system can be written as the following general form:

$$\widehat{H} = -\sum_{I=1}^{P}\frac{\hbar^2}{2M_I}\nabla_I^2 - \sum_{I=1}^{N}\frac{\hbar^2}{2m}\nabla_i^2 + \frac{e^2}{2}\sum_{I=1}^{P}\sum_{J\neq 1}^{P}\frac{Z_I Z_J}{|R_I - R_J|} + \frac{e^2}{2}\sum_{i=1}^{N}\sum_{j\neq 1}^{N}\frac{1}{|r_i - r_j|} - \frac{e^2}{2}\sum_{I=1}^{P}\sum_{i=1}^{N}\frac{Z_I}{|R_I - r_i|} \quad (2\text{-}1)$$

where $R = \{R_I\}, I = 1, \dots, P$ is a set of nuclear coordinates and $r = \{r_i\}, I = 1, \dots, N$ is a set of electronic coordinates. The e, Z_I and $M_I$are the elementally charge, nuclear charges and masses, respectively.

In principle, all the properties can be derived by solving the many-body Schrödinger equation:

$$\widehat{H}\Psi(r, R) = E\Psi(r, R), \quad (2\text{-}2)$$

where Ψ is the many-body wavefunction for the N electronic eigenstates, and E is the total energy.

In practice, the exact solution of this equation is known only for hydrogen-like atoms. Because this is a multicomponent many-body system, where each component, i.e., the nuclear species and the electrons obey a particular statistics, and the total wavefunction cannot be easily factorized because of coulombic correlations. Also, the Schrödinger equation cannot be easily decoupled into a set of independent equations so that, in general, is required to deal with $3P$+$3N$ degrees of freedom. So far, various methods have been developed for approximating the solution for multiple electron systems. Following sections explain the various approximation for simplifying the Schrödinger equation.

2-2 Adiabatic approximation

As one of the approximation method, the adiabatic approximation is also known as Born-Oppenheimer approximation [2-13] and it is based on the difference in mass between nuclei and electrons. It means that the electron velocity is much larger than that of the nuclei due to the difference of mass. Hence, it was proposed that the electrons can be regarded to respond the motion of the nuclei instantaneously, i.e., as the nuclei follow their dynamics, the electrons immediately adjust their wavefunction according to the nuclear wavefunction[2-13]. Hence, the full wavefunction can be expressed as:

$$\Psi(R,r,t) = \Theta_m(R,t)\Phi_m(R,r), \tag{2-3}$$

which is the electronic Schrödinger equation and the equation is the basis for standard quantum chemistry[2-3,7,10,14]. In the electronic Schrödinger equation, the electronic wavefunction $\Phi_m(R,r)$ is the m^{th} stationary state of the electronic Hamiltonian,

$$\hat{h}_e = \hat{T}_e + \hat{U}_{ee} + \hat{V}_{ne} = \hat{H} - \hat{T}_n - \hat{U}_{nn}, \tag{2-4}$$

where $\hat{\mathrm{T}}_n$ and $\hat{U}_{nn}$ are the kinetic and potential nuclear operators, $\hat{\mathrm{T}}_e$ and $\hat{U}_{ee}$ are the kinetic and potential electron operators, and $\hat{\mathrm{V}}_{ne}$ the electron-nuclear interaction.

To obtain the correct potential energy curves from quantum chemical calculations, the interaction between nuclei has to be added:

$$E = E_e + \frac{e^2}{2}\sum_{I=1}^{P}\sum_{J\neq 1}^{P}\frac{Z_I Z_J}{|\boldsymbol{R}_I - \boldsymbol{R}_J|}, \tag{2-5}$$

Separating the electronic and nuclear wavefunctions simplifies the resolution of the total Schrödinger equation. The determination of the entire wavefunction of the system nuclei plus electrons is reduced to finding the total electronic wavefunction. However, the electronic wavefunction cannot be factorized because the presence of an electron in a region of space influences the behavior of other electrons in other regions, so they cannot be considered as individual entities. Hence, getting the exact solution involves solving an equation in $3N$ degrees of freedom. This exact solution is known only for the homogeneous electron gas, for atoms with a small number of electrons and a few small molecules, for larger systems the only option is to employ some types of approximations.

2-3 Hartree-fock approximation

The Hartree approximation postulates that the many-electron wavefunction can be written as a simple product of one-electron wavefunction. Each of these verifies a one-particle

Schrödinger equation in an effective potential that takes into consideration the interaction with the other electrons in a mean-field:

$$\Phi_m(R,r) = \prod_i \varphi_i(r_i), \tag{2-6}$$

$$\left(-\frac{\hbar}{2m}\nabla^2 + V_{eff}^i(R,r)\right)\varphi_i(r) = \varepsilon_i\varphi_i(\boldsymbol{r}), \tag{2-7}$$

where φ_i is the one electron orbital, ε_i is the one-electron eigenvalue, and the effective potential is defined as:

$$V_{eff}^i(R,r) = V(R,r) + \int \frac{\sum_{j\neq i}^N \rho_j(r')}{|r-r'|} dr', \tag{2-8}$$

where the second term in the right side of the equation is the classical electrostatic potential generated by the charge distribution $\sum_{j\neq i}^N \rho_j(\boldsymbol{r})$, and the electronic density associated with particle j is defined as:

$$\rho_j(r) = \left|\varphi_j(r)\right|^2, \tag{2-9}$$

The charge density does not include the charge associated with particle i, so that the Hartree approximation is self-interaction-free. As consequence of the effective potential the electron-electron interaction is counted twice, hence the correct expression for the energy is as follows:

$$E_H = \sum_{n=1}^N \varepsilon_n - \frac{1}{2}\sum_{i\neq j}^N \iint \frac{\rho_i(r)\rho_j(r\prime)}{|r-r'|} dr dr', \tag{2-10}$$

The set of N coupled partial differential equations in (2-7) can be solved by minimizing the energy with respect to a set of variational parameters in a trial wavefunction or, alternatively, by recalculating the electronic densities in (2-9) using the solutions of (2-7), then inserting them back into the expression for the effective potential (2-8), and solving again the Schrödinger equation. This procedure can be iterated, until self-consistency in the input and output wavefunctions or potentials is achieved. This process is called self-consistent Hartree. The Hartree approximation treats the electrons as distinguishable particles, thus it does not consider Pauli's Exclusion Principle that states that two fermions cannot occupy the same quantum state because the many-fermion wave function has to be

antisymmetric upon particle exchange. For two electrons in the same quantum state, the only antisymmetric wavefunction is the null wave function. Hence, the description of the electronic components is incomplete.

The consideration of the Pauli Exclusion Principle is included by proposing an antisymmetrized many-electron wavefunction in the form of a Slater determinant:

$$\Phi_{HF}(x_1, \dots, x_N) = \frac{1}{\sqrt{N!}} \begin{vmatrix} \varphi_1(1) & \varphi_2(1) & \cdots & \varphi_N(1) \\ \varphi_1(2) & \varphi_2(2) & \cdots & \varphi_N(2) \\ \vdots & \vdots & \ddots & \vdots \\ \varphi_1(N) & \varphi_2(N) & \cdots & \varphi_N(N) \end{vmatrix} = SD\{\varphi_1(1)\varphi_2(2) \dots \varphi_N(N)\}, \quad (2\text{-}11)$$

where $\varphi_i(j)$ refers to the i^{th} one-electron spin orbital composed of spatial and spin components, and (j) indicates the spatial and spin coordinates of electron *j* condensed in a single variable $x_1 = (r_j, \sigma_j)$. The mathematical properties of the determinant expression ensures that the wavefunction changes sign when exchanging the coordinates of two of the electrons. The method of approximation consisting of postulating a wavefunction of the form as in [2-11] is called Hartree-Fock (HF) or self-consistent field (SCF) method, and it has been used for long time to calculate the electronic structure of molecular systems, because it provides a reasonable picture of atomic systems and a reasonable good description of interatomic bonding [2-7,10] One of the limitations of HF method is that they do not include electron correlation.[2] This means that HF method takes into account the average effect of electron repulsion, but not the explicit electron-electron interaction. The HF method is usually used as starting point of more rigorous calculations such as Møller-Plesset perturbation theory (MPn, where n is the order of correction), the generalized valence bond (GVB) method, multi-configurational self-consistent field (MCSCF), configuration interaction (CI), and coupled cluster theory (CC) and then correcting for correlation.

2-4 Thomas-fermi approximation

Alongside the HF approximation, Thomas [2-15] and Fermi [2-16] proposed to use the electronic density as the fundamental variable for solving the many-electron problem, since the electron density is a physical observable, it can be measured, calculated, and easily visualized.

In their approximation, Thomas and Fermi stated that the properties of an inhomogeneous system are locally identical to those of the homogeneous electron. This was the first time that the local density approximation (LDA) was used. For the homogeneous electron gas, the density is related to the Fermi energy (ε_F) by:

$$\rho = \frac{1}{3\pi^2}\left(\frac{2m}{\hbar^2}\right)^{3/2} \varepsilon_F^{3/2}, \tag{2-12}$$

and the kinetic energy of the homogeneous gas is:

$$T = \frac{3\rho\varepsilon_F}{5}, \tag{2-13}$$

then the kinetic energy density is:

$$t[\rho] = \frac{3}{5}\frac{\hbar^2}{2m}(3\pi^2)^{2/3}\rho^{5/3}, \tag{2-14}$$

the Thomas-Fermi kinetic energy functional, which is function of the local electron density is:

$$T_{TF}[\rho] = C_k \int \rho(r)^{5/3}\, dr, \tag{2-15}$$

with $C_k = \frac{3}{10}(3\pi^2)^{2/3} = 2.871$ atomic units. Adding to the Thomas-Fermi kinetic energy functional the classical electrostatic energies of electron-nucleus attraction and electron-electron repulsion it is possible to obtain the energy functional of the Thomas-Fermi theory of atoms:

$$E_{TF}[\rho] = C_k \int \rho(r)^{5/3}\, dr + \int v(r)\rho(r)dr + \frac{1}{2}\iint \frac{\rho(r)\rho(r\prime)}{|r-r\prime|} drdr', \tag{2-16}$$

Because E_{TF} depends only on the electronic density, it is a function of the density, which can be minimized with the constraint $\int \rho(r)dr = N$ to approximate the ground state electron density of an atom. The Thomas-Fermi approximation is actually too crude because it does not include exchange and correlation effects, more importantly, no molecular bonding is predicted. However, it sets up the basis for the later development of DFT.

2-5 Density functional theory

The DFT method has become very popular in recent years as it can describe accurately the structure and properties of a system and less computationally demanding than other methods with similar accuracy [2-2,5,17,18].

The modern formalism of DFT started when Hohenberg and Kohn formulated and proved a theorem that put on solid mathematical grounds the ideas proposed by Thomas and Fermi.

2-5-1 Hohenberg-Kohn theorem

The Hohenberg and Kohn theorem is divided into two parts:

Theorem: For any system of interacting particles in an external potential, the potential is uniquely determined by the ground state particle density, except for a trivial additive constant.

Proof: Supposing the opposite, i.e., that the potential is not uniquely determined by the density, then it is possible to find two potentials v and v' such that they have the same ground state density ρ. Let Ψ and $E_0 = \langle\Psi|\hat{H}|\Psi\rangle$ be the ground state wavefunction and ground state energy of $\hat{H} = \hat{T} + \hat{U} + \hat{V}$, and Ψ' and $E_0' = \langle\Psi'|\hat{H}'|\Psi'\rangle$ the ground state wavefunction and ground state energy of $\hat{H}' = \hat{T} + \hat{U} + \hat{V}'$. Owing to the variatonal principle:

$$E_0 < \langle\Psi'|\hat{H}|\Psi'\rangle = \langle\Psi'|\hat{H}'|\Psi'\rangle + \langle\Psi'|\hat{H} - \hat{H}'|\Psi'\rangle, \tag{2-17}$$

which written in terms of the density:

$$E_0 < \langle\Psi'|\hat{H}|\Psi'\rangle = E_0' + \int \rho(\boldsymbol{r})\big(v(\boldsymbol{r}) - v'(\boldsymbol{r})\big)d\boldsymbol{r}, \tag{2-18}$$

Reversing the situation of Ψ and Ψ' it can be obtained:

$$E_0' < \langle\Psi|\hat{H}'|\Psi\rangle = \langle\Psi|\hat{H}|\Psi\rangle + \langle\Psi|\hat{H}' - \hat{H}|\Psi\rangle, \tag{2-19}$$

$$E_0' < \langle\Psi|\hat{H}'|\Psi\rangle = E_0 - \int \rho(r)\big(v(r) - v'(r)\big)dr, \tag{2-20}$$

Adding the inequalities, it turns out that $E_0 + E_0' < E_0' + E_0$, which is absurd. Therefore, there are not two external potentials determined by the same ground state electronic density.

Theorem: A universal functional for the energy $E[\rho]$ in terms of the density $\rho(\boldsymbol{r})$ can be defined valid for any external potential $v(\boldsymbol{r})$. For any particular $v(\boldsymbol{r})$, the exact ground state energy of the system is the global minimum value of this functional, and the density that minimizes the functional is the exact ground state density.

Proof: For a trial electron density $\tilde{\rho}(\boldsymbol{r})$ such that $\tilde{\rho}(\boldsymbol{r}) \geq 0$ and $\int \tilde{\rho}(\boldsymbol{r})\, dr = N$, then $E_0 < E_v[\tilde{\rho}]$, for

$$E_v[\tilde{\rho}] = F[\tilde{\rho}] + \int \tilde{\rho}(\boldsymbol{r})v(\boldsymbol{r})d\boldsymbol{r}, \tag{2-21}$$

and $F[\tilde{\rho}]$ can be defined as:

$$F[\tilde{\rho}] = \langle \Psi[\tilde{\rho}] \big| \hat{T} + \hat{U} \big| \Psi[\tilde{\rho}] \rangle, \tag{2-22}$$

where $\Psi[\tilde{\rho}]$ is the ground state of a potential that has $\tilde{\rho}$ as its ground state density.

Since the external potential is uniquely determined by the density and the potential, in turn, determines the ground state wavefunction, all the other observables of the system such as kinetic energy are uniquely determined. Then, the energy as functional can be written as:

$$\begin{aligned} \langle \Psi[\tilde{\rho}] \big| \hat{H} \big| \Psi[\tilde{\rho}] \rangle &= F[\tilde{\rho}] + \int \tilde{\rho}(r) v(r) dr, \\ &= E_v[\tilde{\rho}] \geq E_v[\rho] = E_0 = \langle \Psi \big| \hat{H} \big| \Psi \rangle, \end{aligned} \tag{2-23}$$

Employing the Rayleigh-Ritz's variational principle applied the electronic density:

$$\delta\{E_v[\rho] - \mu(\int \rho(r) dr - N)\} = 0, \tag{2-24}$$

and a generalized Thomas-Fermi equation is obtained:

$$\mu = \frac{\delta E_v[\rho]}{\delta \rho} = v(r) + \frac{\delta F[\rho]}{\delta \rho}, \tag{2-25}$$

where μ is the Lagrange multiplier associated with the constraint that the number of electrons N is conserved.

Using DFT, one can determine the electronic ground state density and energy exactly, provided that $F[\rho]$ is known [2-4,7,10]. $F[\rho]$ is a universal functional that does not depend explicitly on the external potential. It depends only on the electronic density.

2-5-2 The Kohn-Sham formulation

DFT would remain a minor curiosity today if it were not for the ansatz made by Kohn and Sham, which has provided a way to make useful approximate ground state functionals for real systems of many electrons [2-17]. The idea of Kohn and Sham was to set up a system where the kinetic energy could be determined exactly, since this was a significant problem in Thomas-Fermi theory. Kohn-Sham formulation proposed to replace the kinetic energy of the interacting electrons with that of an equivalent non-interacting system, and that the exact ground state density can be represented by the ground state density of a reference system of non-interacting particles:

$$T = \sum_{s=1}^{2} \sum_{i=1}^{\infty} n_{i,s} \langle \varphi_{i,s} \left| -\frac{\nabla^2}{2} \right| \varphi_{i,s} \rangle, \tag{2-26}$$

$$\rho_s(\boldsymbol{r}, \boldsymbol{r}') = \sum_{i=1}^{\infty} n_{i,s} \varphi_{i,s}(r) \varphi_{i,s}^*(r'), \tag{2-27}$$

where $\{\varphi_{i,s}(r)\}$ are the natural spin orbitals and $\{n_{i,s}\}$ are the occupation numbers of these orbitals. The non-interacting reference system of density $\rho(r)$ that is described by the Hamiltonian:

$$\widehat{H}_R = \sum_{i=1}^{N}(-\frac{\nabla_i^2}{2} + v_R(r_i)), \tag{2-28}$$

where the potential $v_R(r)$ is such that the ground state density of $\widehat{H}_R$ equals $\rho(r)$ and the ground state energy equals the energy of the interacting system. This Hamiltonian has no electron-electron interactions and, thus, its eigenstates can be expressed in the form of Slater determinants meaning that the density can be written as:

$$\rho(r) = \sum_{s=1}^{2}\sum_{i=1}^{N_s}\left|\varphi_{i,s}(r)\right|^2, \tag{2-29}$$

The kinetic term is:

$$T_R[\rho] = \sum_{s=1}^{2}\sum_{i=1}^{N_s}\langle\varphi_{i,s}\left|-\frac{\nabla^2}{2}\right|\varphi_{i,s}\rangle, \tag{2-30}$$

The ground-state density is obtained in practice by solving the N one-electron Schrödinger equations.

$$\left\{-\frac{\nabla^2}{2} + v_R(r)\right\}\varphi_{i,s}(r) = \varepsilon_{i,s}\varphi_{i,s}(r), \tag{2-31}$$

where ε_i are Lagrange multipliers corresponding to the orthonormality of the N single-particle states $\varphi_i(r)$. Then the universal density functional $F[\rho]$ can be partitioned into three terms:

$$F[\rho] = T_R[\rho] + \frac{1}{2}\iint\frac{\rho(r)\rho(r\prime)}{|r-r\prime|}drdr' + E_{XC}[\rho], \tag{2-32}$$

where $E_{XC}[\rho]$, is the exchange-correlation energy as functional of the density, which contains the difference between the exact and non-interacting kinetic energies and also the non-classical contribution to the electron-electron interactions, and $T_R[\rho]$, is the kinetic energy term of the non-interacting reference system. Hence this implies that the correlation piece of the true kinetic energy has been ignored and has to be taken into account elsewhere. This is done by redefining the correlation energy functional in such a way as to include kinetic correlations. Replacing this value for the universal functional in the total energy functional $E_{KS}[\rho] = F[\rho] + \int\rho(r)v(r)dr$, the latter is called the Kohn-Sham functional:

$$E_{KS}[\rho] = T_R[\rho] + \int\rho(r)v(r)dr + \frac{1}{2}\iint\frac{\rho(r)\rho(r\prime)}{|r-r\prime|}drdr' + E_{XC}[\rho], \tag{2-33}$$

In the Kohn-Sham formalism, the Euler equation is expressed as

$$\mu_R = \frac{\delta T_R[\rho]}{\delta\rho(r)} + v_R(r), \tag{2-34}$$

where μ_R is the chemical potential for the non-interacting system and the effective potential v_R or v_{eff} is given by

$$v_{eff}(r) = v(r) + \int\frac{\rho(v_R(r\prime)}{|r-r\prime|}dr' + \mu_{XC}[\rho](r), \tag{2-35}$$

The exchange-correlation potential $\mu_{XC}[\rho](r)$ is the functional derivative of the exchange-correlation energy $\delta E_{XC}[\rho]/\delta\rho$. The solution of the Kohn-Sham equations has to be obtained by an iterative procedure similar to the HF equations and double counting terms have to be subtracted:

$$E_{KS}[\rho] = \sum_{i=1}^{N_s}\sum_{s=1}^{2}\varepsilon_{i,s} - \frac{1}{2}\iint\frac{\rho(r)\rho(r')}{|r-r'|}drdr' + \{E_{XC}[\rho] - \int\rho(r)\mu_{XC}[\rho](r)dr\}, \quad (2\text{-}36)$$

All the unknowns about the many-fermion problem have been displaced to the $E_{XC}[\rho]$ term, while the remaining terms in the energy are known.

2-5-3 Exchange-correlation energy

The fact that both exchange and correlation effects tend to keep electrons apart led to the description of the exchange and correlation contribution in terms of a hole surrounding each electron and keeping other electrons from approaching it. The exchange-correlation hole averaged over the strength of the interaction, taking into consideration kinetic correlations can be defined as:

$$E_{XC}[\rho] = \frac{1}{2}\iint\frac{\rho(r)\tilde{\rho}_{XC}(r,r')}{|r-r'|}drdr', \quad (2\text{-}37)$$

where $\tilde{\rho}_{XC}(r,r') = \rho(r')\,[\tilde{g}(r,r') - 1]$, and $g(r,r')$ is the pair correlation function, that takes into account the fact that the presence of an electron at r discourages a second electron to be located at a position r' because of the Coulomb repulsion.

Needless to mention, neither the exchange-correlation hole density or the pair correlation functional can be calculated exactly. Hence the exchange and correlation functionals have been the focus of many investigations, leading to differently available functionals discussed in the literature.

2.5.3.1 The local density approximation

The simplest and most widely used density functional approximation for the exchange-correlation energy is the LDA. The main idea is to consider general inhomogeneous electronic systems as locally homogeneous, and then to use the exchange-correlation hole corresponding to the homogeneous electron gas for which there are good approximations.

$$\tilde{\rho}_{XC}^{LDA}(r,r') = \rho(r)(\tilde{g}^h[|r-r'|,\ \rho(r)] - 1), \quad (2\text{-}38)$$

where $\tilde{g}^h[|r-r'|,\ \rho(r)]$ is the pair correlation function of the homogenous gas depending only on the distances between r and r', evaluated at the density ρ^h, which locally equals $\rho(r)$.

Using this approximation, the energy per particle of the homogeneous electron gas is defined as:

$$\varepsilon_{XC}^{LDA}[\rho] = \frac{1}{2}\int \frac{\tilde{\rho}_{XC}^{LDA}(r,r')}{|r-r'|}dr' , \tag{2-39}$$

and the exchange-correlation energy becomes:

$$E_{XC}^{LDA}[\rho] = \int \rho(r)\, \varepsilon_{XC}^{LDA}[\rho]dr , \tag{2-40}$$

2-5-3-2 The local spin density approximation

In systems where open electronic shells are studied, taking into consideration, the two spin densities led to better approximations to the exchange-correlation functional. The equivalent of the LDA in spin-polarized systems is the local spin density approximation (LSDA), which consists of replacing the energy per particle of the homogeneous electron gas with a spin-polarized expression:

$$E_{XC}^{LSDA}[\rho_\uparrow(r),\rho_\downarrow(r)] = \int [\rho_\uparrow(r)+\rho_\downarrow(r)]\varepsilon_{XC}^{h}[\rho_\uparrow(r),\rho_\downarrow(r)]dr , \tag{2-41}$$

The LDA is a successful approximation for bulk metals, semiconductors, and ionic crystals. However it fails to reproduce features in atomic systems, where the density has large variation, and the self-interaction is also important. Similarly, the LDA cannot reproduce all the properties in systems with weak molecular bonds, such as hydrogen bond because the density region is very small, and in negatively charged ions because fails to cancel the electronic self-interaction. Likewise, LDA calculations underestimate the energy band gap in semiconductors.

Introducing semi-locally the non-uniformity of the density by expanding $E_{XC}[\rho]$ as a series in terms of the density and its gradients led to some improvements over the LDA and computationally more convenient than full many-body approaches.

2-5-3-3 The generalized gradient approximation

In the generalized gradient approximation (GGA), the exchange-correlation energy has a gradient expansion of the type:

$$E_{XC}[\rho] = \int A_{XC}[\rho]\rho(r)^{4/3}\, dr + \int C_{XC}[\rho]|\nabla\rho(r)|^2/\,\rho(r)^{4/3}dr + \cdots , \tag{2-42}$$

which is asymptotically valid for densities that fluctuate slowly in space. The expansion must be carried out carefully because they can violate one or more of the exact conditions required

for the exchange and correlation holes such as the normalization condition, the negativity of the exchange density and the self-interaction cancellation.[7]

Hence, the GGA expresses the exchange-correlation energy as:

$$E_{XC}[\rho] = \int \rho(r)\varepsilon_{XC}[\rho(r)]\,dr + \int F_{XC}[\rho(r), \nabla\rho(r)]\,dr, \quad (2\text{-}43)$$

where the function F_{XC} needs to satisfy a number of formal conditions for the exchange-correlation hole, such as sum rules, long-range decay. Therefore, there are different GGAs each making a different choice of the F_{XC} function. Among them, the Perdew-Burke-Ernzerhof (PBE)[18,19] exchange-correlation functional satisfies the uniform scaling condition, recovers the correct uniform electron gas limit, obeys the spin-scaling relationship, recovers the LSDA linear response limit, and satisfies the Lieb-Oxford bound. Aditionally, the PBE's GGA does not contain any fitting parameters making it satisfactory from the theoretical point of view. The enhancement factor F_{XC} over the local exchange in the PBE exchange-correlation functional, is defined as:

$$E_{XC}[\rho] = \int \rho(r)\varepsilon_X^{LDA}[\rho(r)]F_{XC}(\rho, \zeta, s)dr, \quad (2\text{-}44)$$

where ρ is the local density, ζ is the relative spin polarization and $s = \frac{|\nabla\rho(r)|}{2k_F\rho}$ is the dimensionless density gradient:

$$F_X(s) = 1 + \kappa - \frac{\kappa}{1+\mu s^2/\kappa}, \quad (2\text{-}45)$$

where $\mu = \beta\left(\frac{\pi^2}{3}\right)$ =0.21951 and β =0.066725 is related to second order gradient expansion.

The correlation energy is written in the following form:

$$E_C^{GGA} = \int \rho(r)[\varepsilon_C^{LDA}(\rho, \zeta) + H[\rho, \zeta, t]]dr, \quad (2\text{-}46)$$

with

$$H[\rho, \zeta, t] = (\frac{e^2}{a_0})\gamma\phi^3 \ln\{1 + \frac{\beta\gamma^2}{t}\left[\frac{1+At^2}{1+At^2+At^4}\right]\}, \quad (2\text{-}47)$$

where $t = \frac{|\nabla\rho(r)|}{2\phi k_s\rho}$ is a dimensionless density gradient, $k_s = (\frac{4k_F}{\pi a_0})^{1/2}$ is the Thomas-Fermi screening wave number and $\phi(\zeta) = \frac{[(1+\zeta)^{2/3}+(1-\zeta)^{2/3}]}{2}$ is a spin-scaling factor. The quantity β is the same as for the exchange term and $\gamma = \frac{1-ln2}{\pi^2} = 0.031091$, and the function $A = \frac{\beta}{\gamma}[e^{-\varepsilon_C^{LDA}[\rho]/(\frac{\gamma\phi^3e^2}{a_0})} - 1]^{-1}$.

The GGA-PBE retains the correct features of LSDA and combines them with the inhomogeneity features that are supposed to be the most important energetically. Some improvements of GGAs over the LDA can be pointed out; improved binding energies and atomic energies, enhanced bond lengths and angles, improved description of hydrogen-

bonded systems. On the other hand, semiconductors are better described by LDA than GGA, lattice constants of noble metals (Ag, Au, Pt) are overestimated by GGA functionals, band gaps and consequently dielectric constants are better estimated by LDA than GGA.

2-6 Projector augmented wave method

Solving the Kohn-Sham equations pose substantial numerical difficulties for example, near the nucleus, due to the large kinetic energy of the electrons, the rapid oscillating wavefunction can be properly represented by a small basis set. On the other hand, in the bonding region between atoms, the kinetic energy is small, and the wavefunction is smooth, and the change in the chemical environment has a strong effect on the shape of the wavefunction, hence requires a large basis set. Various strategies have been developed to deal with the problems mentioned above.

- In the pseudopotential method, the Pauli repulsion of the core electrons is therefore described by an effective potential that expels the valence electrons from the core region. This approach avoids describing explicitly the core electrons, hence avoiding the rapid oscillating wavefunction near the nucleus.
- Augmented wave methods compose their basis functions from atom-like wavefunctions in the atomic regions and a set of envelope functions appropriated for the bonding in between. Space is divided accordingly into atom-centered spheres, defining the atomic regions, and an interstitial region in between. The partial solutions of the different regions are matched at the interface between atomic and interstitial regions.

The projector augmented wave (PAW) method [2-20] combines features from the pseudopotential method and the augmented wave methods into a unified electronic structure method for calculating the total energy, forces, and stress. The PAW method introduced by Blöchl is built on projector functions that map the true wavefunction ($\Psi_n(r)$) with their complete (complicated) nodal structure onto pseudo (auxiliary) wavefunction ($\widetilde{\Psi}_n(r)$), which are easier to treat computationally. The transformation from the auxiliary to the physical wavefunctions is denoted by $\mathcal{T}$, such as:

$$\Psi_n(r) = \mathcal{T}\widetilde{\Psi}_n(r), \tag{2-48}$$

The operator $\mathcal{T}$, has to modify the smooth auxiliary wavefunction in each atomic region, so that the resulting wavefunction has the correct nodal structure.

$$\mathcal{T} = 1 + \sum_R S_R, \tag{2-49}$$

where S_R, is the atomic contribution, that adds the difference between the true and auxiliary wavefunction. The transformation $\mathcal{T}$ shall produce only wavefunctions orthogonal to the core electrons, while the core electrons are treated separately.

Then, total energy can be expressed by auxiliary wavefunctions as:

$$E = E[\Psi_n(r)] = E[\mathcal{T}\tilde{\Psi}_n(r)], \tag{2-50}$$

and the Schrödinger-like equation for auxiliary functions can be obtained, but the Hamiltonian operator has a different form, $\tilde{H} = \mathcal{T}^{\dagger}H\mathcal{T}$, an overlap operator $\tilde{O} = \mathcal{T}^{\dagger}\mathcal{T}$ occurs, and the resulting auxiliary wavefunction are smooth.

To evaluate the physical quantities is required to assess the expectation values of an operator A that can be expressed in terms of the true or the auxiliary wavefunctions

$$\langle A \rangle = \sum_n f_n \langle \Psi_n | A | \Psi_n \rangle = \sum_n f_n \langle \tilde{\Psi}_n | \mathcal{T}^{\dagger} A \mathcal{T} | \tilde{\Psi}_n \rangle, \tag{2-51}$$

where f_n is the occupation state.

The PAW method has extensively proven its high performance compared to norm-conserving pseudopotentials as the total energy expression is less complex and can, therefore, be expected to be more efficient.

2-7 Quantum calculation software

The improved accuracy of DFT led to the point where most established and commercially available codes for molecular calculations nowadays can be run also in DFT mode. Among them Vienna Ab initio Simulation Package (VASP) [2-21-25] computes an approximate solution to the many-body Schrödinger equation by solving the Kohn-Sham equations within DFT. In VASP, the Kohn-Sham equations are solved self-consistently with an iterative matrix diagonalization coupled to highly efficient Broyden and Pulay density mixing schemes [2-26,27] to speed up the self-consistency cycle. The iterative matrix diagonalization is performed by techniques and algorithms implemented in VASP, like the residual minimization method with direct inversion of the iterative subspace (RMM-DIIS) or blocked Davidson algorithms. The algorithms calculate the electronic ground state for a given geometry, calculate forces, and then based on these forces calculate a new geometry. This process is repeated until an energy (force) criterion is reached. The interactions between the electrons and ions are described using norm-conserving or ultrasoft pseudopotentials, or the PAW method.

2-7-1 Periodic boundary conditions

Crystalline solids contain an infinite number of electrons, hence the wavefunction has to be calculated for each electron and the basis set, in which the wavefunction is expressed will also be infinitely large. To overcome this issue, periodic boundary conditions are introduced to reduce the studied system to one particular unit cell that is periodically repeated in three dimensions. The periodicity for surfaces and clusters is in two dimensions. Crystal surfaces are represented as slabs, i.e., several layers of atoms that can represent the bulk and surface atoms with a vacuum region. This vacuum region must be large enough to prevent any spurious interaction between the adsorbate and the next periodic image.

According to Bloch's theorem [2-28], and the periodicity of the crystal, the massive number of one-electron wavefunctions is reduced to the number of electrons in the unit cell to be computed. Then the wavefunction of an electron, $\psi_{j,k}$, within a periodic potential, can be written as the product of a lattice periodic part $\mu_j(r)$, and a wavelike part $e^{ik\cdot r}$:

$$\psi_{j,k}(r) = \mu_j(r)e^{ik\cdot r}, \tag{2-52}$$

where *j* indicates the band index and k is a continuous wavevector that is confined to the first Brillouin zone of the reciprocal lattice. To minimize the number of *k*-points needed to integrate the Brillouin zone, a number of special set of k-points is employed that can be calculated by various methods. Among them, in the Monkhorst-Pack method [2-29], the *k*-points are distributed homogeneously throughout space in rows and columns that follow the shape of the Brillouin zone:

$$k_j = x_{1j}b_1 + x_{2j}b_2 + x_{3j}b_3, \tag{2-53}$$

where b_1, b_2, b_3 are the reciprocal vectors

and,

$$x_{ij} = \frac{l_i}{n_j}, \quad j = 1, \dots, n_j\ , \tag{2-54}$$

where l_i are the lengths of the reciprocal lattice vectors and n_j characterizes the number of special points in the set.

In order to reproduce accurately the properties of the researched material, a sufficiently large number of *k*-points must be used. However, the computational cost increases with increasing the *k*-point mesh. Therefore, it is usual to test a varied set of *k*-points until the convergence is reached within the chosen accuracy.

In this work, two different material systems were engaged. Hence, to reproduce the materials and species' properties accurately, and to obtain meaningful and reproducible

results different computational details were employed for each study. For each of the problems tackled a subsection with its specific computational procedure can be found in their respective chapter of the results and discussion.

Reference

(2-1) Jensen, F. *Molecular Modelling*, Second edit.; John Wiley & Sons Ltd.: Chichester, England, 2007.

(2-2) Young, D. C. *Computational Chemistry A Practical Guide for Applying Techniques to Real-World Problems*; John Wiley & Sons, Inc.: New York, USA, 2001.

(2-3) Hehre, W. J. *A Guide to Molecular Mechanics and Quantum Chemical Calculations*; Wavefunction, Inc.: Irvine, CA, 2003.

(2-4) Jalbout, A. F.; Nazari, F.; Turker, L. Gaussian-Based Computations in Molecular Science. *J. Mol. Struct. THEOCHEM* **2004**, *671* (1–3), 1–21.

(2-5) Lejaeghere, K.; Bihlmayer, G.; Björkman, T.; Blaha, P.; Blügel, S.; Blum, V.; Caliste, D.; Castelli, I. E.; Clark, S. J.; Dal Corso, A.; et al. Reproducibility in Density Functional Theory Calculations of Solids. *Science* **2016**, *351* (6280), 1415.

(2-6) von Barth, U. Basic Density-Functional Theory an Overview. *Phys. Scr.* **2004**, *T109* (6), 9–39.

(2-7) Kohanoff, J.; Gidopoulos, G. N. Density Functional Theory: Basics, New Trends and Applications. In *Handbook of Molecular Physics and Quantum Chemistry. Volume 2: Molecular Electronic Structure*; Wilson, S., Bernath, P. F., McWeeny, R., Eds.; John Wiley & Sons, Ltd: Chichester, England, 2003; pp. 532–568.

(2-8) Jones, R. O. Density Functional Theory: Its Origins, Rise to Prominence, and Future. *Rev. Mod. Phys.* **2015**, *87* (3), 897–923.

(2-9) Perdew, J. P.; Kurth, S. Density Functionals for Non-Relativistic Coulomb Systems in the New Century. In *A Primer in Density Functional Theory. Lecture Notes in Physics*; Fiolhais, C., Nogueira, F., Marques, M., Eds.; Springer: Berlin, Heidelberg, 2003; Vol. 620, pp. 1–55.

(2-10) Kohanoff, J. *Electronic Structure Calculations for Solids and Molecules*, First edit.; Cambridge University Press: Cambridge, England, 2006.

(2-11) Hohenberg, P.; Kohn, W. Inhomogeneous Electron Gas. *Phys. Rev.* **1964**, *136* (3B), B864–B871.

(2-12) Kohn, W.; Sham, L. J. Self-Consistent Equations Including Exchange and Correlation Effects. *Phys. Rev.* **1965**, *140* (4A), A1133–A1138.

(2-13) Born, M.; Oppenheimer, R. Zur Quantentheorie Der Molekeln. *Ann. Phys.* **1927**, *389* (20), 457–484.

(2-14) Frank, I. On the Classical Description of Nuclear Motion. *arXiv:1402.1133* **2014**, 6, 1–3.

(2-15) Thomas, L. H. The Calculation of Atomic Fields. *Math. Proc. Cambridge Philos. Soc.* **1927**, *23* (5), 542–548.

(2-16) Fermi, E. Un Metodo Statistico per La Determinazione Di Alcune Proprietá Dell' Atomo. *Rend. Accad. Naz. del Lincei, Cl. Sci. Fis., Mat. e. Nat.* **1927**, *6* (6), 602–607.

(2-17) Perdew, J. P.; Burke, K.; Ernzerhof, M. Generalized Gradient Approximation Made Simple. *Phys. Rev. Lett.* **1996**, *77* (18), 3865–3868.

(2-18) Martin, R. M. *Electronic Structure*, First edit.; Cambridge University Press: Cambridge, 2004.

(2-19) Perdew, J. P.; Burke, K.; Ernzerhof, M. Generalized Gradient Approximation Made Simple-ERRATA. *Phys. Rev. Lett.* **1996**, *77* (18), 3865–3868.

(2-20) Blöchl, P. E. Projector Augmented-Wave Method. *Phys. Rev. B* **1994**, *50* (24), 17953–17979.

(2-21) Kresse, G.; Hafner, J. Ab Initio Molecular Dynamics for Liquid Metals. *Phys. Rev. B* **1993**, *47* (1), 558–561.

(2-22) Kresse, G.; Hafner, J. Norm-Conserving and Ultrasoft Pseudopotentials for First-Row and Transition Elements. *J. Phys. Condens. Matter* **1994**, *6* (40), 8245–8257.

(2-23) Kresse, G.; Furthmüller, J. Efficiency of Ab-Initio Total Energy Calculations for Metals and Semiconductors Using a Plane-Wave Basis Set. *Comput. Mater. Sci.* **1996**, *6* (1), 15–50.

(2-24) Kresse, G.; Furthmüller, J. Efficient Iterative Schemes for Ab Initio Total-Energy Calculations Using a Plane-Wave Basis Set. *Phys. Rev. B - Condens. Matter Mater. Phys.* **1996**, *54* (16), 11169–11186.

(2-25) Kresse, G.; Joubert, D. From Ultrasoft Pseudopotentials to the Projector Augmented-Wave Method. *Phys. Rev. B* **1999**, *59* (3), 1758–1775.

(2-26) Broyden, C. G. A Class of Methods for Solving Nonlinear Simultaneous Equations. *Math. Comput.* **1965**, *19* (92), 577–577.

(2-27) Pulay, P. Convergence Acceleration of Iterative Sequences. the Case of Scf Iteration. *Chem. Phys. Lett.* **1980**, *73* (2), 393–398.

(2-28) Baldereschi, A. Mean-Value Point in the Brillouin Zone. *Phys. Rev. B* **1973**, *7* (12), 5212–5215.

(2-29) Monkhorst, H. J.; Pack, J. D. Special Points for Brillouin-Zone Integrations. *Phys. Rev. B* **1976**, *13* (12), 5188–5192.

CHAPTER 3

Understanding effect of Ce and Zr on chemical expansion in yttrium doped strontium cerate and zirconate by high temperature X-ray analysis and density functional theory

3-1. Introduction

To reduce the use of fossil fuels, one possible approach is to improve the energy conversion efficiencies of alternative energy technologies. Solid oxide fuel cells (SOFCs) are promising energy conversion devices characterized by energy conversion efficiencies higher than those of conventional thermal power systems. Another approach is to utilize renewable energy sources, i.e., solar energy, wind energy, etc., or the combination of fuel cells and water electrolysis which will allow mass energy storage via hydrogen storing techniques [3-1,3-2,3-3]. Solid oxide fuel cells and solid oxide electrolysis cells (SOECs) have higher energy conversion efficiencies than low-temperature fuel cells and water electrolyzers. Therefore, solid oxide cells are promising candidates for reducing the reliance on fossil fuel energy.

The operating temperatures of the current SOFCs and SOECs, which primarily use stabilized zirconia as the electrolyte, are higher than 700 ℃. Such high temperatures are necessary to ensure sufficient mobility of the oxide ions in the solid oxide electrolytes, as well as fast kinetics at the electrodes. However, the high operating temperatures require the use of high-cost materials and result in the degradation of cell performance over time. Thus, lowering the operating temperature is an important challenge underlying the development of solid oxide cells.

Proton-conducting oxides based on aliovalent-doped perovskites have attracted attention because proton conduction proceeds in temperature ranges lower than those required by oxide ion-conductor-based oxide cells [3-4] due to the relatively low temperature dependence of proton mobility in comparison with that of oxide ion mobility. Although following equation was shown in chapter 1, formation of the protonic charge carriers is commonly understood to proceed via the hydration of oxide ion vacancies:

$$H_2O + V_O^{\bullet\bullet} \rightleftarrows O_O^{\times} + 2H_i^{\bullet} \quad (3\text{-}1)$$

,where $V_O^{\bullet\bullet}$, $O_O^{\times}$, and $H_i^{\bullet}$ denote oxide ion vacancy, oxide ion at its regular site, and proton, respectively, in Kröger-Vink notation[3-5,3-6]. Thus, hydration is the key process allowing proton conduction to take place in the oxides. However, a side effect of this hydration is chemical expansion: the incorporation of a water molecule into an oxide vacancy results in expansion of the perovskite lattice, leading to possible damage to the solid oxide cell components induced by mismatches in the dimensions of the proton conducting oxides, electrodes, and gas seals [3-7].

In fact, Okuzaki *et al.* reported the influence of chemical expansion due to hydration on oxygen vacancies of $Ba(Zr_{0.5}Ce_{0.4})_xY_yO_{3-\delta}$ which is one type of proton conducting oxides as follows. The sample with this composition was broken by the chemical expansion during the sintering process as the amount of Y was increased. Figure 3-1 shows the samples after sintering process as function of amount of Y. As shown in this figure, when Y doped amount was over 25 mol%, cracking took place. The researchers also mentioned that the sample became easier to be broken when the chemical expansion increased. Figure 3-2a shows the results of X-ray diffraction analysis, and the lattice volume of $Ba(Zr_{0.5}Ce_{0.4})_{7/9}Y_{0.3}O_{3-\delta}$ was measured at respective temperature. As seen from figure 3-2 b to 3-2e, the sample still held the shape at 350 ℃, but it was broken at 400 ℃ at which the chemical expansion became maximum. The above phenomenon is problematic from the viewpoint of safety for electrochemical devices such as fuel cells and steam electrolyzer [3-8].

(a) $Ba(Zr_{0.5}Ce_{0.4})_{8/9}Y_{0.2}O_{3-\delta}$ (b) $Ba(Zr_{0.5}Ce_{0.4})_{7.5/9}Y_{0.25}O_{3-\delta}$ (c) $Ba(Zr_{0.5}Ce_{0.4})_{7/9}Y_{0.3}O_{3-\delta}$

Figure 3-1 Samples after sintering process. Y is introduced over 0.25 mol% in the samples and they are broken. The length of scale bar is approximately 1 cm.[3-8]

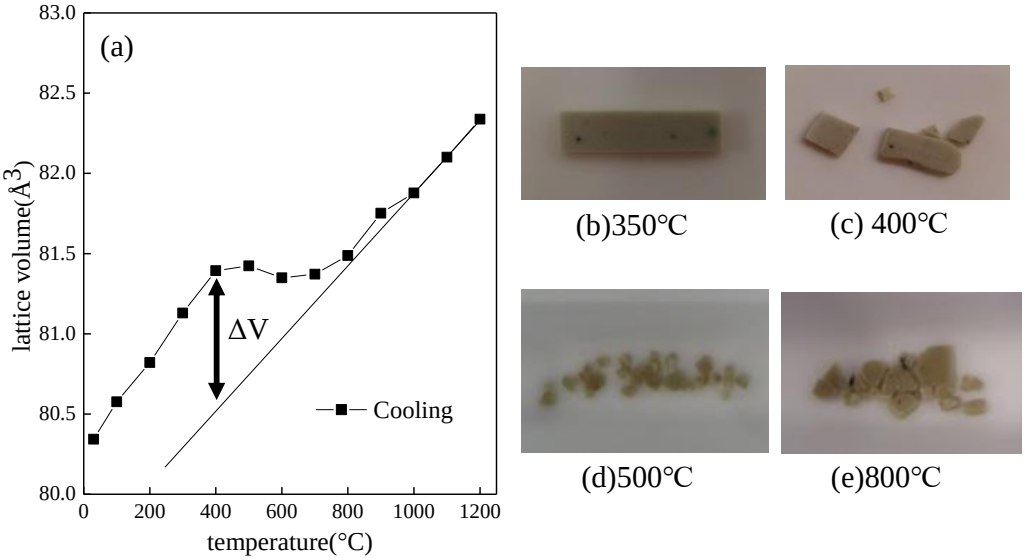

Figure 3-2 (a)The lattice volume of $Ba(Zr_{0.5}Ce_{0.4})_{7/9}Y_{0.3}O_{3-\delta}$ at respective temperature analyzed by X-ray diffraction analysis. The sample was measured in wet N_2 (pH_2O = 1.9kPa) and ΔV shows the effect of chemical expansion. (b)-(e) shows the pictures of sample at respective temperature, and it was broken above 400℃. [3-8]

To reduce such chemical expansion, its cause must first be clarified, and then a suitable chemical composition must be designed so as to minimize the expansion coefficient. This study employs strontium cerate and strontium zirconate as two model materials to assess how the incorporation of cerium or zirconium at the *B*-site of ABO_3 differently affects the hydration-induced chemical expansion. The use barium at the *A*-site is beneficial for obtaining high conductivity, although barium can be volatilized at high temperatures. For simplicity, strontium was selected as the *A*-site cation in this study. Yttrium was chosen as a typical dopant for the *B*-site, which works to provide oxide ion vacancies for hydration.

Density functional theory (DFT) for first-principle simulations was employed to theoretically evaluate the influence of Ce and Zr at the *B*-site on chemical expansion in the proton conductors. High-temperature X-ray diffraction (HT-XRD) and thermogravimetric analysis (TGA) were employed to experimentally evaluate the degree of hydration and chemical expansion in the two proton-conducting oxides.

3-2. Experimental

3-2-1. Experimental Procedure

<Material Preparation>

Ceramic powders equivalent to the chemical compositions of $SrCe_{0.922}Y_{0.078}O_{3-\delta}$ and $SrZr_{0.922}Y_{0.078}O_{3-\delta}$ were prepared by a solid state reaction method previously described [3-9, 3-10]. Powders of $SrCO_3$, CeO_2, ZrO_2, and Y_2O_3 were used as starting materials. The powders were weighed appropriately, mixed, and calcined for 10 hours in air at 1250 °C for yttrium-doped strontium cerate and at 1350 °C for yttrium-doped strontium zirconate. The products were ground with a planetary ball mill, isostatically pressed into disk shapes at 250 MPa, and sintered for 10 hours to obtain dense ceramics. Sintering temperatures were 1550 °C for yttrium-doped strontium cerate and 1650 °C for yttrium-doped strontium zirconate. Finally, $SrCe_{0.922}Y_{0.078}O_{3-\delta}$ and $SrZr_{0.922}Y_{0.078}O_{3-\delta}$ powders were obtained by grinding sintered pellets into granules. X-ray diffraction (XRD) measurements were taken at room temperature using a Rigaku Ultima IV diffractometer with Cu Kα irradiation (40 kV, 40 mA) to confirm that the diffraction patterns of the prepared materials agreed with the perovskite structure of $SrCeO_3$ (ICSD 01-083-1157) and $SrZrO_3$ (ICSD 00-044-0161), with no secondary phases.

< High Temperature X-ray Analysis >

HT-XRD analyses were carried out in the temperature range between 100 °C and 1200 °C in a humidified nitrogen gas stream ($p(H_2O)$=1.9 kPa) to investigate the chemical expansion behavior of $SrCe_{0.922}Y_{0.078}O_{3-\delta}$ and $SrZr_{0.922}Y_{0.078}O_{3-\delta}$. First, the temperature was maintained at 50 °C for 60 min and then increased to 1200 °C at a heating rate of 60 °C/min. After holding at 1200 °C for 180 min, the temperature was decreased from 1200 °C to 100 °C and XRD patterns were obtained every 100 °C. The cooling rates were 20 °C/min from 1200 to 500 °C, 10 °C/min from 500 to 400 °C, 5 °C/min from 400 to 300 °C, and 2 °C/min from 300 to 100 °C, and the measurements were taken every 10 min (1200-600 °C), 20 min (500-400 °C), or 30 min (300-100 °C).

< Thermogravimetric Analysis >

TGA (TG-DSC, NETZSCH Jupiter, STA449F3) was carried out to evaluate the amount of water incorporated in the proton conductor specimens. The granular samples with approximately 500 mg each were heated from 50 °C to 1200 °C at 5 °C/min in dry N_2 and kept at 1200 °C for 90 min. Then, the dry N_2 atmosphere was changed to wet N_2 ($p(H_2O)$ = 950 Pa

or 633 Pa) and cooled to 100 °C. During cooling, the temperature was decreased in 100 °C increments and maintained at each 100 °C step for 60 min.

3-2-2 Computational Details

All DFT calculations were performed using the Vienna Ab initio simulation package (VASP) [3-11, 3-13]. The Perdew-Burke-Ernzerhof (PBE) [3-14] exchange-correlation functional was employed based on the projector-augmented wave (PAW) method [3-11]. The cutoff energy for the plane wave basis set was 500 eV for all calculations. A DFT+U approach was applied to the f-orbitals of Ce with a value of U = 5 eV [3-15]. The PAW method pseudopotentials with valence states of Sr (4s, 4p, 5s, 4d), Zr (4s, 4p, 5s, 4d), Ce (5s, 5p, 5d, 4f, 6s), Y (4s, 4p, 5s, 4d), and O (2s, 2p) were used for all calculations. All ionic positions were optimized by a conjugate gradient method until the forces on each ion were below 0.01 eV/Å^2. Spin polarization was not considered during the calculations.

The computed lattice parameters were consistent with those determined experimentally and by DFT calculations in previous reports, as shown in Table 3-1[3-16, 3-17, 3-18]. On the basis of the optimized unit cell, $SrZrO_3$ and $SrCeO_3$ supercells with 2×2×2 orthorhombic $Sr_{32}Zr_{32}O_{96}$ and 2×2×2 orthorhombic $Sr_{32}Ce_{32}O_{96}$ cells were constructed and optimized using 3×3×4 and 3×3×4 Monkhorst-Pack *k*-points meshes, respectively. Further, one oxide ion vacancy was introduced by substituting two Y for Ce or Zr, creating $Sr_{32}Zr_{30}Y_2O_{95}$ and $Sr_{32}Ce_{32}Y_2O_{95}$, respectively. Hydrated $Sr_{32}Zr_{30}Y_2O_{95}$ and $Sr_{32}Ce_{32}Y_2O_{95}$ supercells, whose respective compositions are described as $Sr_{32}Zr_{30}Y_2O_{96}H_2$ and $Sr_{32}Ce_{30}Y_2O_{96}H_2$, were also optimized. To evaluate the chemical expansion of either composition, the lattice volumes of $Sr_{32}Zr_{30}Y_2O_{95}$, $Sr_{32}Ce_{30}Y_2O_{95}$, $Sr_{32}Zr_{30}Y_2O_{96}H_2$, and $Sr_{32}Ce_{30}Y_2O_{96}H_2$ were estimated.

Table 3-1 Calculated and experimental lattice parameters of $SrZrO_3$ and $SrCeO_3$

Solid oxide	Lattice parameter	This work, GGA-PBE	GGA-PBE	Experiment
$SrZrO_3$ (orthorhombic)	a (Å)	5.70	5.81[15]	5.79[16]
	b (Å)	5.74	5.87[15]	5.82[16]
	c (Å)	8.19	8.24[15]	8.20[16]
$SrCeO_3$ (orthorhombic)	a (Å)	6.07	5.945[17]	6.01[17]
	b (Å)	6.24	6.103[17]	6.15[17]
	c (Å)	8.70	8.506[17]	8.60[17]

3-3. Results and Discussion

3-3-1 Chemical expansion determined by HT-XRD

XRD patterns of $SrCe_{0.922}Y_{0.078}O_{3-\delta}$ and $SrZr_{0.922}Y_{0.078}O_{3-\delta}$ measured at the respective temperatures under a wet N_2 atmosphere ($p(H_2O)$ = 1.9 kPa) are shown in Fig. 3-3. The diffraction peaks shifted to lower angles with increasing temperature, as seen in the right sides of Figs. 3-2 (a) and (b); in other words, the lattices expanded as temperature was increased. Lattice volume plotted as a function of temperature is shown in Fig. 3-3. A discontinuous change in the lattice volume is observed at around 400–600 °C due to chemical expansion originating from hydration of the oxide vacancies, as shown by dashed lines in Figs 3-4 (a) and (b). Chemical expansion by volume is defined as the ratio of $\Delta V_{lattice}$, the discontinuous change in the lattice volume, to the unit cell volume of un-hydrated perovskite lattice, $V_{lattice}$, as summarized by the following equation:

$$\text{(Chemical expansion)} = \Delta V_{lattice}/V_{lattice} \quad (3\text{-}2)$$

This ratio corresponds to the difference between the cell volumes of the hydrated and un-hydrated forms. As summarized in Table 3-2, the chemical expansions were determined to be 0.0030 (0.30 %) and 0.0016 (0.16 %) for $SrCe_{0.922}Y_{0.078}O_{3-\delta}$ and $SrZr_{0.922}Y_{0.078}O_{3-\delta}$, respectively.

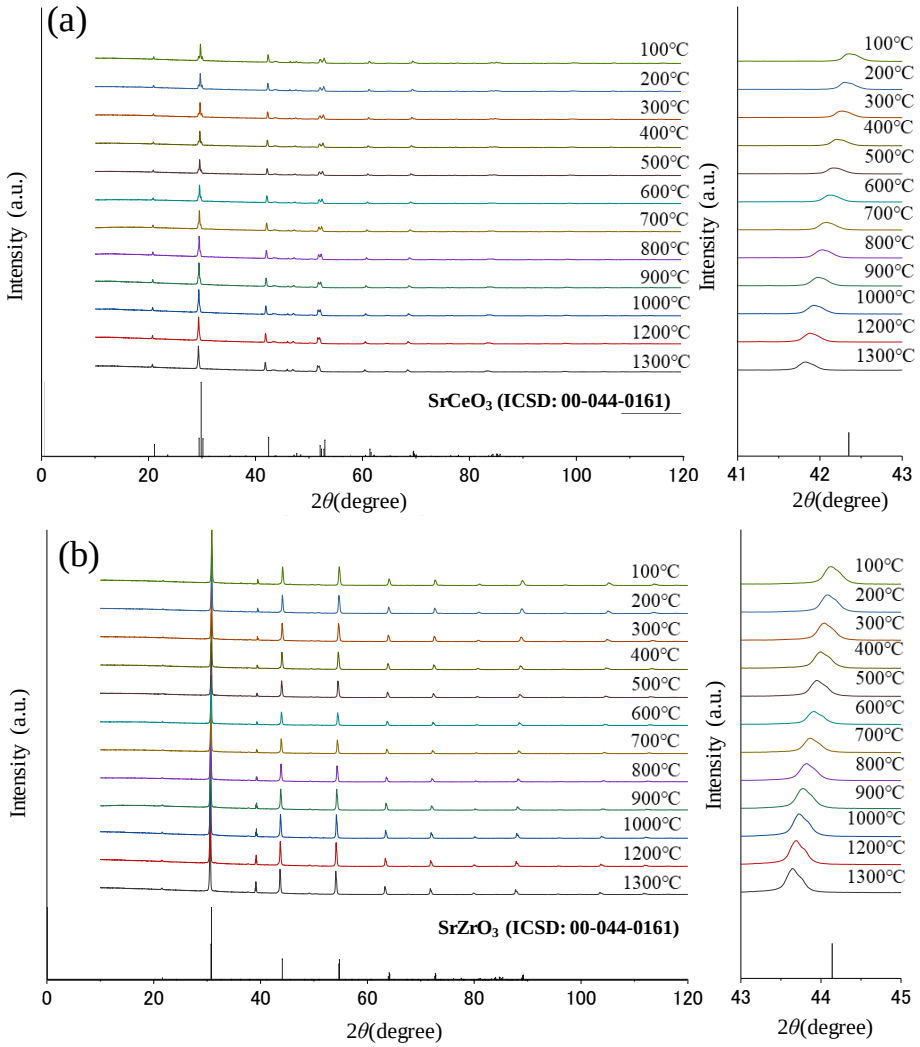

Fig. 3-3. XRD profiles as function of temperature of $SrCe_{0.922}Y_{0.078}O_{3-\delta}$ (a) and $SrZr_{0.922}Y_{0.078}O_{3-\delta}$ (b) in wet N_2. Right figures magnify the patterns in the 2θ range 41°-43° to show the peak shift with the change of temperature.

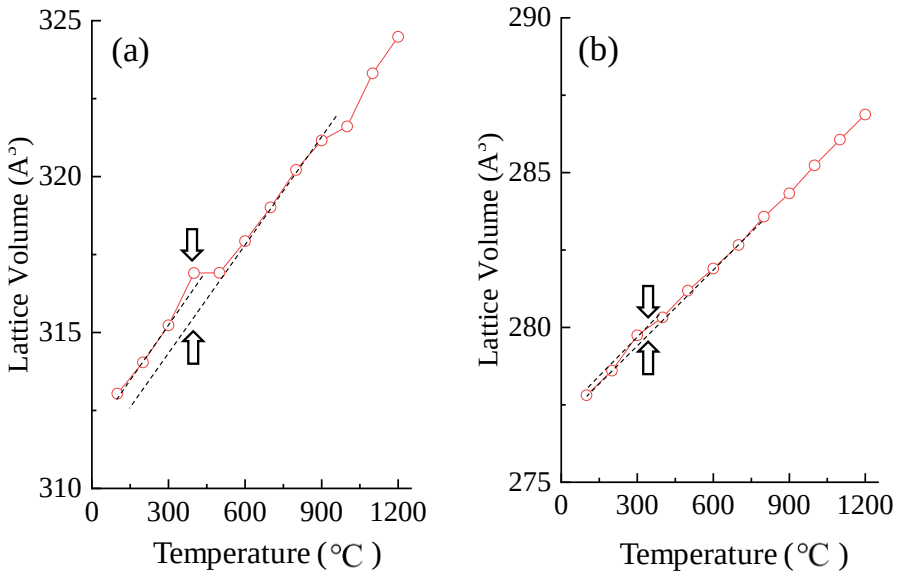

Fig. 3-4. Temperature dependence of lattice volumes of $SrCe_{0.922}Y_{0.078}O_{3-\delta}$ (a) and $SrZr_{0.922}Y_{0.078}O_{3-\delta}$ (b).

Table 3-2 Chemical Expansion, Degree of hydration, and Chemical expansion coefficient of $SrCe_{0.922}Y_{0.078}O_{3-\delta}$ and $SrZr_{0.922}Y_{0.078}O_{3-\delta}$ determined by HT-XRD and TG analysis.

	Chemical expansion*	Degree of hydration**	Protonic defect concentration	Chemical expansion coefficient: β_{chem}
	$\Delta V_{lattice}/V_{lattice}$	[OH]/[Y]	[OH] (mol/mol)	$(\Delta V_{lattice}/V_{lattice})$/[OH]
$SrCe_{0.922}Y_{0.078}O_{3-\delta}$	0.0030	0.20-0.24	0.016-0.019	0.16–0.19
$SrZr_{0.922}Y_{0.078}O_{3-\delta}$	0.0016	0.50-0.52	0.039-0.040	0.040–0.041

*determined by HT-XRD at $p(H_2O)$ = 1900 Pa,

**determined by TGA at $p(H_2O)$ = 633 Pa and 950 Pa.

3-3-2 Thermogravimetric analysis (TGA)

TGA was conducted for $SrCe_{0.922}Y_{0.078}O_{3-\delta}$ and $SrZr_{0.922}Y_{0.078}O_{3-\delta}$ to evaluate their proton concentrations. The weight changes were estimated based on increases in the sample weight relative to the weight in dry N_2 at 1200 °C, assuming that the specimens were almost completely dehydrated at this temperature, and the weight change was converted to the degree of hydration based on the reaction shown in equation 3-1. 1. As seen in Figure 3-5, the weight

change during the heating process was larger than that during the cooling process. This is presumably due to the influence of the physical adsorption of water on the sample surface before starting the measurement, and thus the amount of hydration was evaluated from the data obtained during the cooling process. The degree of hydration is defined by the following equation.

$$\text{(Degree of hydration)} = [\text{OH}]/[\text{Y}] \quad (3\text{-}3)$$

where [OH] and [Y] are the molar amounts of protons and yttrium relative to the molar amount of the mother ABO_3 perovskite. As shown in Table 3-2, the degree of hydration of $SrCe_{0.922}Y_{0.078}O_{3-\delta}$ in wet N_2 ($p(H_2O)$ = 633 Pa and 950 Pa), 0.20–0.24, was smaller than that of $SrZr_{0.922}Y_{0.078}O_{3-\delta}$, 0.50–0.53. The degree of hydration was not significantly dependent on the humidity in the gas atmosphere, and thus the result can be compared to the chemical expansion data obtained by HT-XRD (under N_2 at 1.9 kPa $p(H_2O)$) described in the former section. Using the data from the HT-XRD and TGA, the chemical expansion coefficient, β_{chem}, can be obtained according to the following equation:

$$\beta_{chem} = (\Delta V_{lattice}/V_{lattice})/[\text{OH}] \quad (3\text{-}4)$$

The data is summarized in Table 3-2. The existence of a linear relation between chemical expansion and hydration is not guaranteed. However, the chemical expansion values cannot be compared without being normalized based on the degree of hydration, and thus β_{chem} is used hereafter for this comparison. The β_{chem} of $SrCe_{0.922}Y_{0.078}O_{3-\delta}$ was approximately 4 times higher than that of $SrZr_{0.922}Y_{0.078}O_{3-\delta}$. It was thus concluded that the choice of using Ce instead of Zr results in greater chemical expansion.

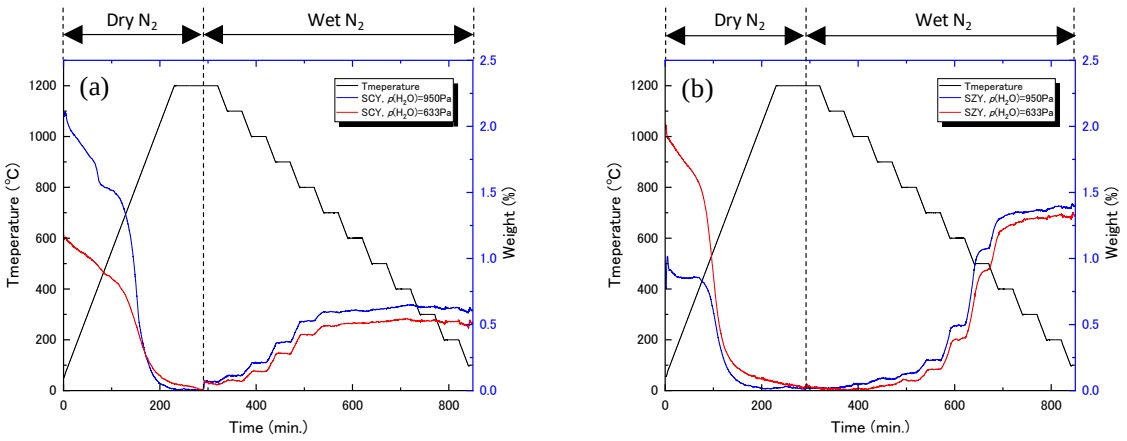

Fig. 3-5. The results of thermogravimetric analysis for $SrCe_{0.922}Y_{0.078}O_{3-\delta}$ (a) and $SrZr_{0.922}Y_{0.078}O_{3-\delta}$ (b) in respective water partial pressure.

3-3-3 Chemical Expansion evaluated by Density Functional Theory (DFT) first principle simulation

Geometry optimization was carried out for the hydrated and dehydrated yttrium-doped strontium cerate and zirconate supercells by means of DFT simulations. Two Y atoms were introduced in the 2x2x2 supercells to introduce one oxide ion vacancy or one water molecule, as shown in Fig. 3-6. The following points lie arbitrarily on the atomic arrangement in the supercells:

(i) Relative locations of the two Y atoms

(ii) Location of the oxide-ion vacancy relative to Y atoms

(iii) Location of protons relative to Y atoms

As shown later, Y-O-Y clustering results in a more energetically stable state than the case in which the two Y atoms are distant from each other. However, considering the real materials and their preparation processes, since the mobility of Y is relatively low, Y atoms may adopt relatively flexible configurations due to the high-temperature sintering process and the successive cooling period. Similar random positioning of Y dopants has been previously reported, and will be discussed in succeeding sections [3-19, 3-20]. Therefore, two cases were examined: when the two Y atoms were in closest proximity, linked via one oxygen atom (Figs. 3-6 (a1) and (b1)), and when they were furthest apart (Figs. 3-6 (a2) and (b2)). In regards to points (ii) and (iii) of the list above, oxide ion vacancies and protons have relatively high mobility, and thus the most energetically stable configurations were employed.

Table 3-3 (a) shows the enthalpies of $Sr_{32}M_{30}Y_2O_{95}$ (M = Ce or Zr) containing one oxide ion vacancy per supercell (hereafter referred to as $E(Sr_{32}M_{30}Y_2O_{95})$), of one water molecule $E_M(H_2O)$, and of $Sr_{32}M_{30}Y_2O_{96}H_2$ (M = Ce or Zr) $E(Sr_{32}M_{30}Y_2O_{96}H_2)$, in the case wherein the two Y atoms were closest to each other. Table 3-3 (b) shows the same data corresponding to the case wherein the two Y atoms were furthest apart. $E(Sr_{32}M_{30}Y_2O_{95}H_2)$ was lower than $E(Sr_{32}M_{30}Y_2O_{95})+E(H_2O)$ in both Y distribution cases, as shown in columns d in Table 3-3 (a) and (b). This implies that hydration is energetically favored in both the cerate and zirconate. In both the hydrated and dehydrated forms, as shown in Table 3-3 (a) and (b), the enthalpy of the supercell with the Y atoms in close proximity was lower than that of the case wherein the Y atoms were further apart. This means that the cell configuration containing the Y atoms in close proximity was favored over the configuration wherein the Y atoms were further apart.

Chemical expansion due to hydration was evaluated by comparing the cell volumes of $Sr_{32}M_{30}Y_2O_{95}$ with those of $Sr_{32}M_{30}Y_2O_{96}H_2$ (M = Ce or Zr). The chemical expansion

coefficient, β_{chem}, was calculated using the chemical expansion ratio ($\Delta V_{lattice}/V_{lattice}$) and protonic defect concentration ([OH]). As shown in Table 3-4 (a), in the case of the Y atoms in close proximity, $Sr_{32}Ce_{30}Y_2O_{95}$ had a chemical expansion coefficient 1.6 times smaller than that of $Sr_{32}Zr_{30}Y_2O_{95}$. The experimentally determined chemical expansion coefficient of $SrCe_{0.922}Y_{0.078}O_{3-\delta}$ was larger than that of $SrZr_{0.922}Y_{0.078}O_{3-\delta}$, showing the opposite tendency. In contrast, in case of the Y atoms further apart, $Sr_{32}Ce_{30}Y_2O_{95}$ exhibited a chemical expansion coefficient 3.1 times larger than that of $Sr_{32}Zr_{30}Y_2O_{95}$, which is in agreement with the experimental results. As shown in Table 3-3 (a), the cell was more energetically stable when the Y atoms were in close proximity than when they were further apart. If only the most stable atomic configuration is considered, the DFT calculations predict a smaller chemical expansion coefficient for the cerate than for the zirconate. However, considering the preparation process for these materials which involves sintering at high temperatures and successive cooling, along with the relatively low mobility of yttrium, it is reasonable that the material could exist in a mixture of the two different Y-atom configurations. Omata *et al.* reported that both Y-O-Y and Y-O-Zr configurations coexist in Y-doped strontium zirconate, as determined by infrared spectroscopy[3-19]. Furthermore, Yugami et al. stated that increasing the Y concentration in Y-doped strontium cerates results in disorder of the Y distribution in the lattice [3-20]. These reports support the possibility of the mixed Y configuration.

Based on these results, the experimental observation that $SrCe_{0.922}Y_{0.078}O_{3-\delta}$ had a higher chemical expansion coefficient than $SrZr_{0.922}Y_{0.078}O_{3-\delta}$ can be accounted for by the DFT calculation. The chemical expansion coefficient of $Sr_{32}Ce_{30}Y_2O_{95}$ is lower than that of $Sr_{32}Zr_{30}Y_2O_{95}$ when the Y atoms are in close proximity, but higher when the Y atoms are far apart. Considering the sample preparation process and the previously mentioned studies, the two Y configurations were presumed to coexist, resulting in the higher chemical expansion coefficient for $SrCe_{0.922}Y_{0.078}O_{3-\delta}$ than $SrZr_{0.922}Y_{0.078}O_{3-\delta}$.

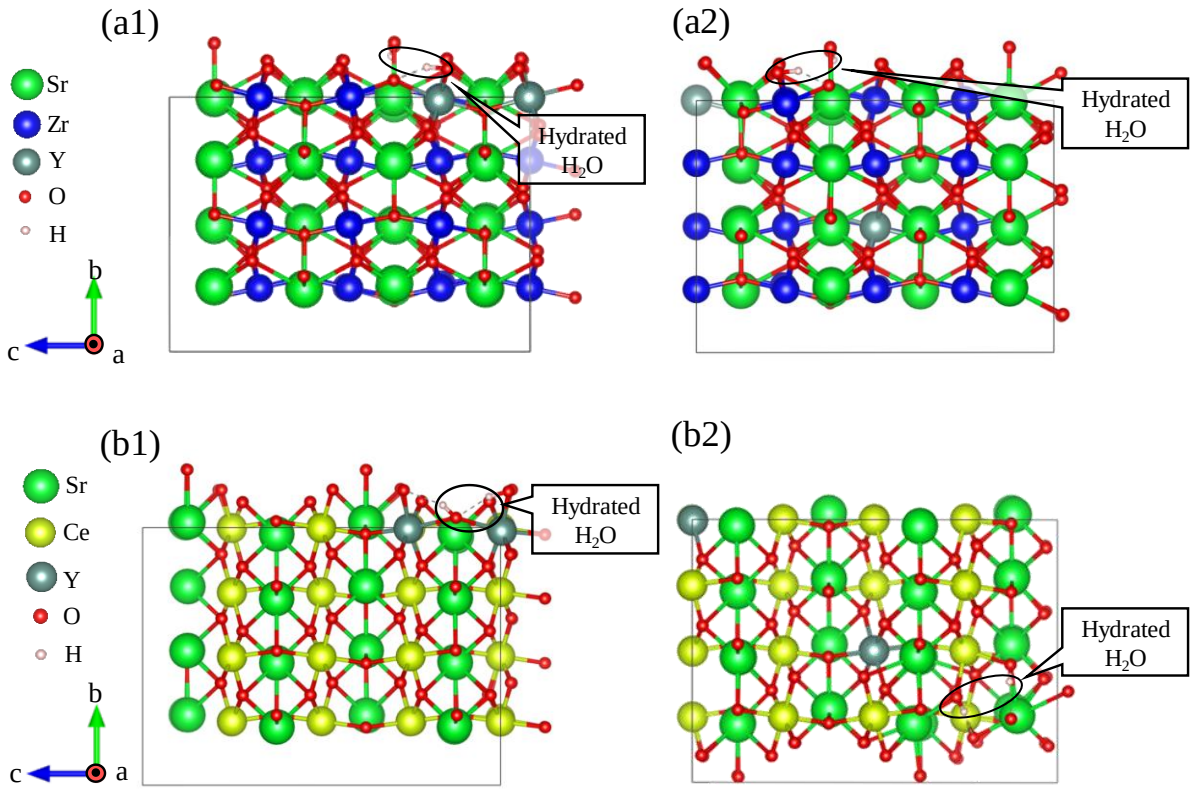

Fig. 3-6. Optimized hydrated yttrium doped strontium cerate (a) and zirconate (b) supercell depending on Y configuration: Y atoms are close each other in $Sr_{32}Zr_{30}Y_2O_{96}H_2$ (a1), Y atoms are distant each other in $Sr_{32}Zr_{30}Y_2O_{96}H_2$ (a2), Y atoms are close each other in $Sr_{32}Ce_{30}Y_2O_{96}H_2$ (b1), and Y atoms are distant each other in $Sr_{32}Ce_{30}Y_2O_{96}H_2$ (b2). Three atoms in black circles are hydrated water molecules. All schematic models are visualized with VESTA[3-23].

Table 3-3. Enthalpies of dehydrated/hydrated yttrium doped strontium cerate/zirconate depending on the Y configuration: The case that Y atoms are close each other(a) and The case that Y atoms are distant each other(b), and one water molecule. Each water molecule has same lattice volume of dehydrated yttrium doped strontium cerate/zirconate.

(a)Y atoms are close each other

M (*B*-site)	a. $E(Sr_{32}M_{30}Y_2O_{95})$	b. $E_M(H_2O)$	c. $E(Sr_{32}M_{30}Y_2O_{96}H_2)$	d. c-(a+b)
Ce	-1161.279	-14.220	-1176.278	-0.779
Zr	-1315.586	-14.220	-1331.137	-1.331

(b) Y atoms are distant each other

M (*B*-site)	$Sr_{32}M_{30}Y_2O_{95}$ (Å^3)	$Sr_{32}M_{30}Y_2O_{96}H_2$ (Å^3)	Chemical expansion $\Delta V_{lattice}/V_{lattice}$	Chemical expansion Coefficient: β_{chem} $(\Delta V_{lattice}/V_{lattice})$/[OH]
Ce	2565.66	2570.50	0.0018	0.0288
Zr	2280.73	2287.34	0.0028	0.0448

3-3-4 Oxide ion vacancy size in DFT-optimized geometry

To explain why the chemical expansion due to hydration depends on the configuration of the Y atoms, the sizes of the oxide ion vacancies in $Sr_{32}Ce_{30}Y_2O_{95}$ and $Sr_{32}Zr_{30}Y_2O_{95}$ were evaluated. During hydration, the oxide ion vacancies accommodate water molecules. Local stress originating from the incorporation of oxygen atoms into the vacancies, as well as the following relaxation, result in the chemical expansion. Thus, smaller oxide ion vacancies may possibly result in a larger degree of chemical expansion. Fig. 3-7 shows the results of evaluating the sizes of the oxide ion vacancies in $Sr_{32}Zr_{30}Y_2O_{95}$ and $Sr_{32}Ce_{30}Y_2O_{95}$, by use of the atomic coordinates determined by geometry optimization and Shannon's ionic radii [3-21]. As shown in Figs. 3-7 (a1) and (b1), which corresponds to the case wherein the Y atoms are in close proximity, the radius of the oxide ion vacancy in $Sr_{32}Ce_{30}Y_2O_{95}$ was 1.69 Å, which is larger than that in $Sr_{32}Zr_{30}Y_2O_{95}$, 1.30 Å. On the other hand, Figs. 3-7 (a2) and (b2), which correspond to the case wherein the Y atoms were further apart, the radii of the oxide ion vacancies in $Sr_{32}Zr_{30}Y_2O_{95}$ and $Sr_{32}Ce_{30}Y_2O_{95}$ were both 1.24 Å. The observation that $Sr_{32}Ce_{30}Y_2O_{95}$ exhibited a lesser degree of chemical expansion than $Sr_{32}Zr_{30}Y_2O_{95}$ in the close-proximity Y

configuration is explained by the larger oxide ion vacancy in the former. Although some other factors could influence the chemical expansion behavior, these results indicate a correlation between the chemical expansion and the size of the oxide ion vacancies to be hydrated. The result of a low chemical expansion in $Sr_{32}Ce_{30}Y_2O_{95}$ in the case of Y-Y close configuration is corresponded by the large size of oxide-ion vacancy. In other words, the chemical expansion is dependent on the Y configurations because the size of the oxide ion vacancy differs by the Y configurations.

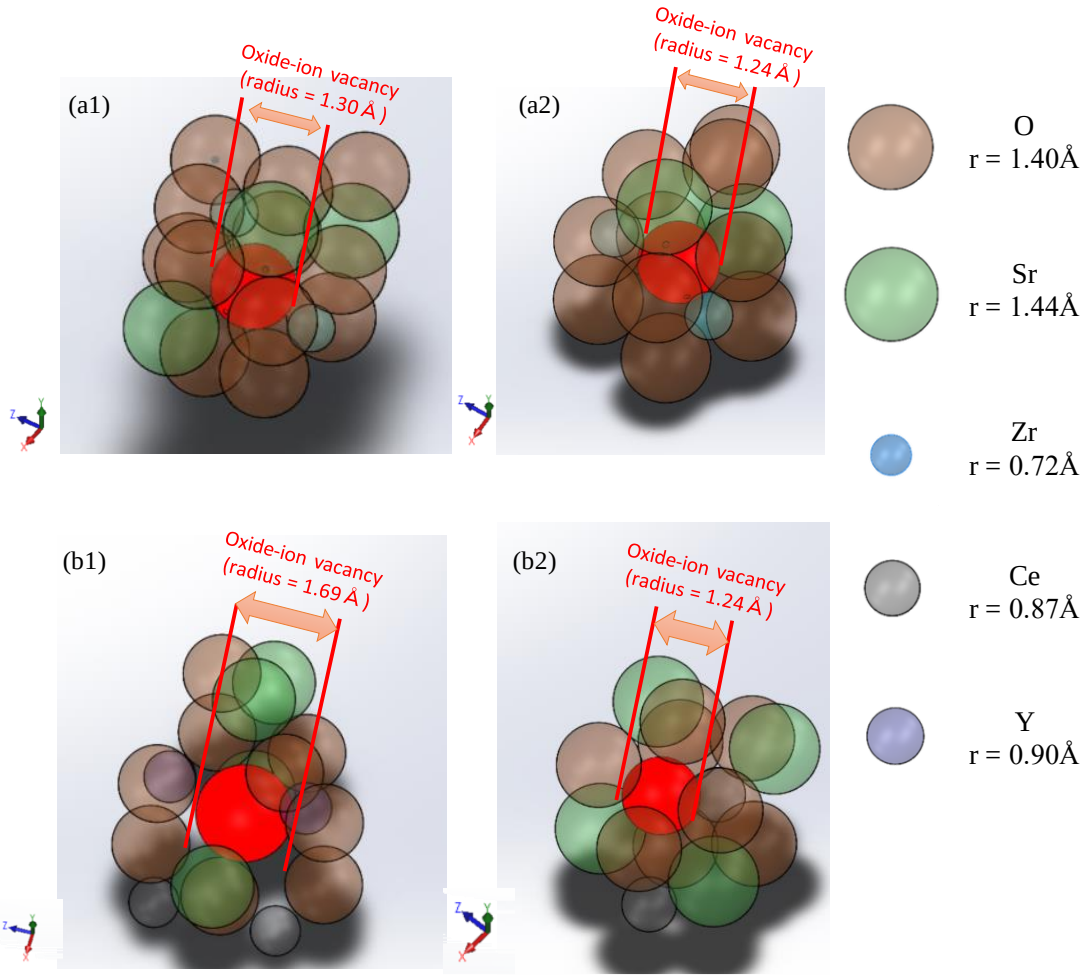

Fig. 3-7. Oxygen vacancy sizes in $Sr_{32}Ce_{30}Y_2O_{95}$ and $Sr_{32}Zr_{30}Y_2O_{95}$ depending on Y configuration: Y atoms are close each other in $Sr_{32}Zr_{30}Y_2O_{96}H_2$ (a1), Y atoms are distant each other in $Sr_{32}Zr_{30}Y_2O_{96}H_2$ (a2), Y atoms are close each other in $Sr_{32}Ce_{30}Y_2O_{96}H_2$ (b1), and Y atoms are distant each other in $Sr_{32}Ce_{30}Y_2O_{96}H_2$ (b2). Orange, green, light blue, gray, and purple spheres are oxygen, strontium, zirconium, cerium, and yttrium, respectively. The sign of r means Shannon radii of respective atoms.

3-3-5 Elastic character of $Sr_{32}Ce_{30}Y_2O_{95}$ and $Sr_{32}Zr_{30}Y_2O_{95}$

As mentioned previously, chemical expansion is considered to be the result of the relaxation of local stress due to the incorporation of oxide ions into vacancies. Thus, the elastic character of the material should also influence the chemical expansion; a lower bulk elastic modulus should give rise to a greater degree of chemical expansion. The lattice enthalpy changes in $Sr_8Ce_6Y_2O_{23}$ and $Sr_8Zr_6Y_2O_{23}$ upon isotropic deformation between -2% and +2% by volume. Fig. 3-8 shows lattice enthalpy as a function of the isotropic deformation was investigated. The fitted line for $Sr_8Ce_6Y_2O_{23}$ exhibits a lesser degree of curvature than that of $Sr_8Zr_6Y_2O_{23}$, indicating that the cerate has a smaller bulk elastic modulus than the zirconate. This means that the cerate should undergo more extensive deformation than the zirconate in response to the same level of stress. This difference between the elastic moduli of the cerate and zirconate can explain the result shown in the former section for the configuration wherein the Y atoms were spaced further apart. Despite the similar sizes of the oxide ion vacancies as shown in Figs. 3-7 (a2) and (b2), $Sr_{32}Ce_{30}Y_2O_{95}$ has a higher chemical expansion coefficient than $Sr_{32}Zr_{30}Y_2O_{95}$ (Table 3-4 (b)). This can be attributed to the lower elastic modulus of the cerate in comparison to that of the zirconate.

One possible explanation for the difference in the elastic modulus is the difference between the Ce-O and Zr-O bond lengths. Anderson and Soga reported that chemical bonds become weaker as bond length increases [3-22]. Because Ce is larger than Zr, the bulk modulus of cerate will be smaller than zirconate. Another possible explanation involves the ionicity/covalency of *B*-O bonds (*B*=Ce or Zr). Covalent bonds have relatively higher force constants than ionic bonds, and thus higher covalency may result in lower chemical expansion (and vice versa). To compare the iconicity/covalency of *B*-O bonds in the materials used in this study, the electron densities in $Sr_{32}Ce_{30}Y_2O_{95}$ and $Sr_{32}Zr_{30}Y_2O_{95}$ were mapped, as shown in Fig. 3-9, wherein the blue planes follow the center of one *B*-site and the nearest oxygen. As shown in Fig. 3-10, the electron density between Ce and O is lower than that between Zr and O. This means that the Ce-O bond has less covalent character than the Zr-O bond, which may explain the difference between the chemical expansion coefficients of $Sr_{32}Ce_{30}Y_2O_{95}$ and $Sr_{32}Zr_{30}Y_2O_{95}$. The covalency results can be also explicable from the viewpoints of difference of electronegativity between Zr/Ce and oxygen. Because the amount of electronegativity difference between Zr and oxygen is smaller than that between Ce and oxygen, iconicity between Ce and oxygen is larger than that between Zr and oxygen.

The DFT calculation results indicated that the chemical expansion in $Sr_{32}Ce_{30}Y_2O_{95}$ and $Sr_{32}Zr_{30}Y_2O_{95}$ differs based on the configuration of the Y dopant atoms, as shown in section 3.3. The results discussed in sections 3.4 and 3.5 suggest correlations between the chemical expansion and differences in the size of oxygen vacancies and elastic moduli between the cerate and zirconate. The size of oxygen vacancies and the elastic modulus are thus the factors that explain the differences in chemical expansion behavior between the cerate and zirconate.

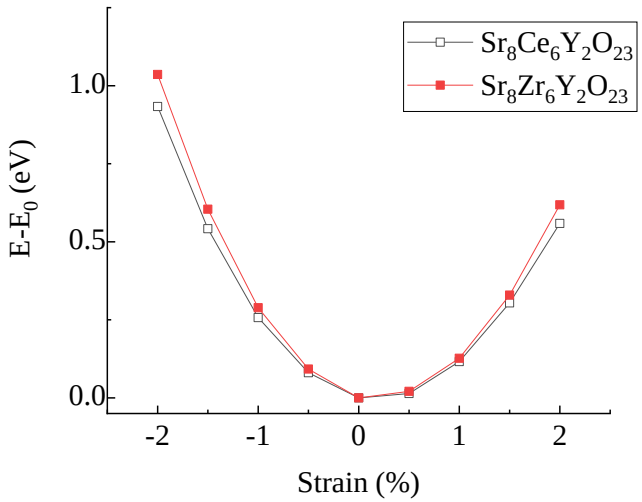

Fig. 3-8. Lattice energy comparison as a function of bulk modulus for $Sr_8M_6Y_2O_{23}$ (M = Ce or Zr). E_0 indicates the lattice energy of respective structure at 0% strain.

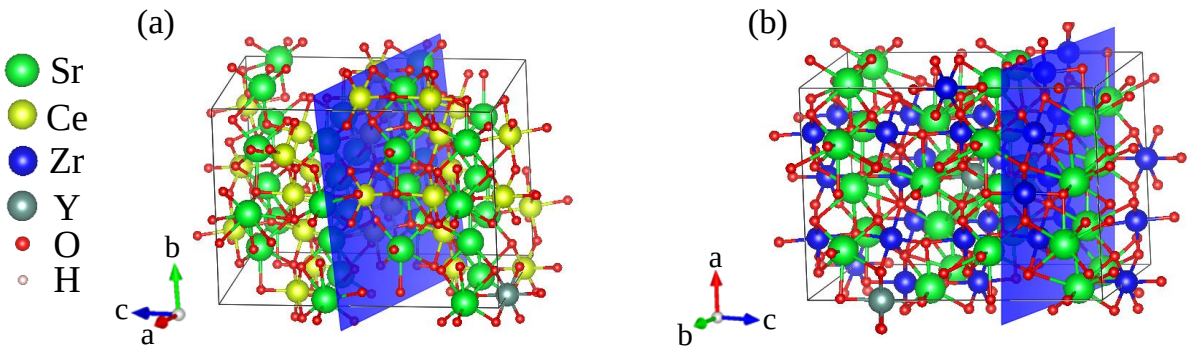

Fig. 3-9. Electron density mapping planes (Blue planes) in $Sr_{32}Ce_{30}Y_2O_{95}$ (a) and $Sr_{32}Zr_{30}Y_2O_{95}$ (b) in case that two Y atoms are distatn each other. Miller indices for each plane are (-4.60637 -1.00000 18.10390) in $Sr_{32}Ce_{30}Y_2O_{95}$ and (-5.41039 1.00000 34.8758) in $Sr_{32}Zr_{30}Y_2O_{95}$.

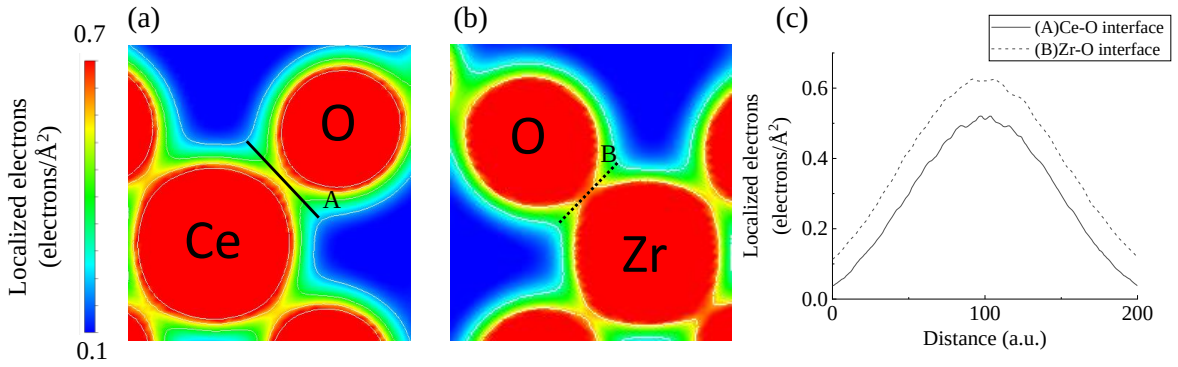

Fig. 3-10. Electron density maps at the interface between Ce/Zr and O: Ce-O interface in $Sr_{32}Ce_{30}Y_2O_{95}$ (a), Zr-O interface in $Sr_{32}Zr_{30}Y_2O_{95}$ (b) and Localized electrons comparison with Ce-O (Line A in left figure) and Zr-O (Dotted line B in left figure) interface (c).

Table 3-4. Chemical expansion of $Sr_{32}M_{30}Y_2O_{95}$ (M = Ce or Zr) by hydration process depending on Y configuration: The case that Y atoms are close each other(a) and the case that Y atoms are distant each other(b)

(a) The case that Y atoms are close each other

M (B-site)	$Sr_{32}M_{30}Y_2O_{95}$ (Å^3)	$Sr_{32}M_{30}Y_2O_{96}H_2$ (Å^3)	Chemical expansion $\Delta V_{lattice}/V_{lattice}$	Chemical expansion Coefficient: β_{chem} $(\Delta V_{lattice}/V_{lattice})/[OH]$
Ce	2565.66	2570.50	0.0018	0.0288
Zr	2280.73	2287.34	0.0028	0.0448

(b) The case that Y atoms are distant each other

M (B-site)	$Sr_{32}M_{30}Y_2O_{95}$ (Å^3)	$Sr_{32}M_{30}Y_2O_{96}H_2$ (Å^3)	Chemical expansion $\Delta V_{lattice}/V_{lattice}$	Chemical expansion Coefficient: β_{chem} $(\Delta V_{lattice}/V_{lattice})/[OH]$
Ce	2546.88	2562.6	0.0061	0.0976
Zr	2219.92	2224.41	0.0020	0.0320

3-4 Conclusion

This research investigated the effect of Ce and Zr in yttrium-doped strontium zirconate and cerate on chemical expansion by hydration. HT-XRD and TGA indicated that the cerate has a chemical expansion coefficient approximately 4 times larger than that of the zirconate.

DFT calculations suggested that the chemical expansion coefficient is dependent on the configuration of the Y atoms: the cerate exhibited lower chemical expansion than the zirconate when the Y atoms were in close proximity and higher chemical expansion when the Y atoms were further apart. Thus, the experimental observation of the larger degree of chemical expansion in the cerate than in the zirconate can be attributed to the mixed presence of both configurations of Y atoms.

DFT calculations suggested that the size of oxide ion vacancies differs based on the Y atom configuration: when the Y atoms were in close proximity, the cerate exhibited larger oxide ion vacancies than the zirconate, which resulted in the lesser degree of chemical expansion in the former. The results indicated a correlation between the chemical expansion and the size of oxide ion vacancies to be hydrated, and that the size of the oxide ion vacancies is correlated with the configuration of Y dopant atoms. The elastic character is another factor influencing the different chemical expansion behavior of the cerate and zirconate: the former has a lower bulk elastic modulus which led to a higher degree of chemical expansion.

Reference

[3-1] S.H. Mohr, J. Wang, G. Ellem, J. Ward, D. Giurco, *Fuel*, **141**, (2015) 120–135. https://doi.org/10.1016/j.fuel.2014.10.030

[3-2] P. Lianos, *Applied Catalysis B: Environmental*, **210**, (2017) 235–254. https://doi.org/10.1016/j.apcatb.2017.03.067

[3-3] M.S. Dresselhaus, I. Thomas, *Nature* **414**, (2001) 332–337. https://doi.org/10.1038/35104599

[3-4] K. Zagórski, S. Wachowski, D. Szymczewska, A. Mielewczyk-Gryń, P. Jasiński, and M. Gazda, *Journal of Power Sources*, **353**, (2017) 230–236. http://dx.doi.org/10.1016%2Fj.jpowsour.2017.04.007

[3-5] H. Matsumoto, T. Shimura, H. Iwahara, T. Higuchi, K. Yashiro, A. Kaimai, T. Kawada, J. Mizusaki, *Journal of Alloys and Compounds*, **408–412**, (2006) 456–462. https://doi.org/10.1016/j.jallcom.2004.12.093

[3-6] H. Iwahara, T. Esaka, H. Uchida, N. Maeda, *Solid State Ionics* **3–4**, (1981) 359–363. https://doi.org/10.1016/0167-2738(81)90113-2

[3-7] A. K. E. Andersson, S. M. Selbach, C. S. Knee, T.Grande, *Journal of the American Ceramic Society* **97**, (2014) 2654–2661

[3-8] I. Okuzaki, Y.S. Lee, K. Keonard, and H. Matsumoto "Heating-cooling procedure to avoid mechanical failure of proton conducting ceramics" Meeting Abstracts. P34 . 19th Solid State Protonic Conductors, 2018.

[3-9] F. Krug, T. Schober, T. Springer, *Solid State Ionics*, 81, (1995) 111–118. https://doi.org/10.1111/jace.12990

[3-10] T. Schober, *Solid State Ionics*, **145**, (2001) 319–324. http://dx.doi.org/10.1016/S0167-2738(01)00926-2

[3-11]G. Kresse, J. Furthmüller, *Physical review B*, **54**, (1996) 11169–11186. https://doi.org/10.1103/PhysRevB.54.11169

[3-12] G. Kresse and D. Joubert, *Physical review B*, **59**, (1999) 1758–1775. https://doi.org/10.1103/PhysRevB.59.1758

[3-13] G. Kresse, J. Furthmüller, *Computational Materials Science*, **6**, (1996)15–50. https://doi.org/10.1016/0927-0256(96)00008-0

[3-14] J. P. Perdew, K. Burke, M. Ernzerhof, *Physical review letters*, **77**, (1996) 3865–3868. https://doi.org/10.1103/PhysRevLett.77.3865

[3-15] Y. Chen, P. Hu, M. H. Lee, H. Wang, *Surface Science*. **602**, (2008)1736–1741. https://doi.org/10.1016/j.susc.2008.02.036

[3-16] M.A. Gomez, S. Jindal, K.M. Fletcher, L.S. Foster, N.D.A. Addo, D. Valentin, C. Ghenoiu, A. Hamilton, The Journal of chemical physics, **126**, (2007) 194701. https://doi.org/10.1063/1.2735592

[3-17] A. Ahtee, M. Ahtee, AM. Glazer, AW. Hewat. *Acta Crystallographica Section B*, **32(12)**, (1976) 3243–3246. https://doi.org/10.1107/S0567740876010029

[3-18] M. Swift, C.G. Van de Walle, *The Journal of Physical Chemistry C*, **120**, (2016) 9562–9568. https://pubs.acs.org/doi/10.1021/acs.jpcc.6b00765

[3-19] T. Omata, Y. Noguchi, S. Otsuka-Yao-Matsuo, *Journal of The Electrochemical Society*, **152**, (2005) E200-E205. doi: 10.1149/1.1899269

[3-20] H. Yugami, Y. Chiba, M. Ishigame, *Solid State Ionics*, **77**, (1995) 201–206. https://doi.org/10.1016/0167-2738(94)00263-R

[3-21] R. D. Shannon, Acta Crystallogr., 1976, **32**, 751–767.
https://doi.org/10.1107/S0567739476001551
[3-22] O. L. Anderson, N. Soga. Journal of Geophysical Research, **72**, (1967) 5754–5757.
https://doi.org/10.1029/JZ072i022p05754
[3-23] K. Momma, F. Izumi, *Journal of Applied Crystallography*. **44**, (2011) 1272–1276.
doi:10.1107/S0021889811038970

CHAPTER 4

Origin of proton conducting oxides

4-1 Introduction

There are mainly two types of ion conductors for SOFCs or SOEC, which are known as oxide-ion conductors and proton conducting oxides. They are known as oxide ion conductors and proton conducting oxides, respectively. Firstly, as a typical example of oxide ion conductor, yttrium stabilized ZrO_2 (YSZ) exhibits sufficient oxide ion conductivity with higher chemical stability over 800 ℃ following in equation 4-1. Figure 4-1 shows the reported examples of reported oxide ion conductors, and they have oxide-ion vacancies in the crystal structure[4-1].

$$Y_2O_3 + 2Zr_{Zr}^{\times} + O_O^{\times} \rightarrow 2Y_{Zr}^{/} + V_O^{\bullet\bullet} + 2ZrO_2 \qquad (4\text{-}1)$$

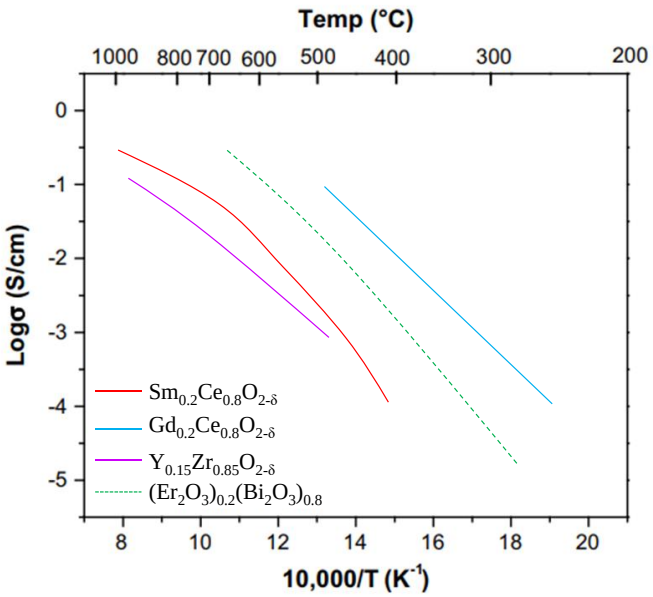

Figure 4-1 Inverse temperature dependence of total conductivities of SDC (Samarium doped ceria), GDC (Gadolinia doped ceria), 8YSZ (8 mol.% yttria stabilized zirconia), and ESB[4-1].

On the other hand, proton conducting oxides which have perovskite structure (ABO_3) have been experimentally shown to be proton conduction in wet atmosphere. Appearance of proton conduction is understood by following origin that hydration reaction occurs to oxide-ion vacancies. One experimental evidence that hydration occurs in the proton conducting oxides is equilibrium constant. From the equation of Kröger-Vink notation representing hydration reaction in equation 4-2, the equilibrium constant can be expressed thermodynamically following equation 4-3.

$$H_2O + V_O^{\bullet\bullet} + O_O^{\times} \rightleftarrows 2OH_O^{\bullet} \tag{4-2}$$

$$K = \exp\left(\frac{\Delta S^{\circ}}{R}\right)\exp\left(\frac{\Delta H^{\circ}}{RT}\right) = \frac{[OH_O^{\bullet}]}{[O_O^{\times}][V_O^{\bullet\bullet}]P_{(H_2O)}} \tag{4-3}$$

Looking at the equilibrium constant in Figure 4-2, it is clear that the equilibrium constant becomes remarkably positive around 600 °C or more, and it can be seen that the hydration reaction proceeds with the those proton conducting oxides. In addition, the dissolved amount of protons is remarkable at about 600 °C or lower. Many researchers have focused on proton conducting oxides such as proton concentrations for investigating proton conductivity or chemical expansion, which are thermodynamic properties and physical properties [4-2]. However, since proton conducting oxides were discovered by Iwahara *et al.* in 1981, a question of why metal oxides with oxygen vacancies could serve as proton conducting oxides has been missed.

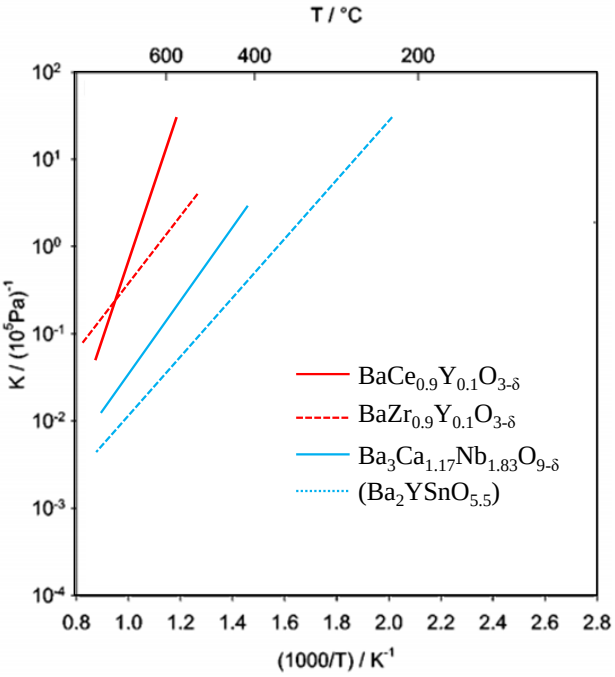

Figure 4-2 (a) Hydration isobars for cubic perovskite-type oxides [4-2]

These days, a paper focusing on that question was reported by Yuhang *et al*. They simulated how the protons hydrated in the oxygen vacancies on the surface of SZY and YSZ are conducting to the bulk by first principles calculation. They reported that the activation energy of protons that is incorporated from the surface of SZY into the bulk is smaller than that of YSZ. This phenomenon may be applied to other proton conducting oxides and oxide ion conductors. However, in addition to their interest regarding proton behavior on the surface, it is indispensable to approach the origin of proton conducting oxides for the bulk. For this reason, this study attempts to develop their research and approach the origin of the proton conducting oxides due to the difference in bulk properties between SZY and YSZ.

As shown by previous studies using DFT, when hydration takes place in the oxygen vacancies of SZY, the hydration enthalpy is negative while the YSZ becomes positive. (In this case, the hydration enthalpy is expressed as difference obtained by subtracting enthalpy of hydrated SZY from the sum of enthalpy of dehydrated SZY and that of water molecule.) To explain this difference of hydration enthalpies between SZY and YSZ, this study focuses on covalency between Zr and oxygen. When hydration takes place into positively charged oxygen vacancies, oxygen of water and Zr will make a bond. If the bond has ionic bonds, it is

considered that the energy gain is smaller than when covalent bond is created. On the other hand, when it makes covalent bonding property, the water will be more energetically stable with the covalent bonding than ionic bonding. In this study, the covalency between Zr and oxygen of SZY and YSZ after hydration was compared by DFT based on the above hypothesis.

4-2 Computational Details

DFT calculations were performed using the Vienna Ab initio simulation package (VASP) [4-3–4-5]. The Perdew-Burke-Ernzerhof (PBE) [4-6] exchange-correlation functional was employed based on the projector-augmented wave (PAW) method [4-3]. The cutoff energy for the plane wave basis set was 500 eV for all calculations. The PAW method pseudopotentials with valence states of Sr (4s, 4p, 5s, 4d), Zr (4s, 4p, 5s, 4d), Y (4s, 4p, 5s, 4d), and O (2s, 2p) were used for all calculations. All ionic positions were optimized by a conjugate gradient method until the forces on each ion were below 0.01 eV/Å^2. Spin polarization was not considered during the calculations. The computed lattice parameters were consistent with those determined experimentally and by DFT calculations in previous reports, as shown in Table 4-1. On the basis of the optimized unit cell, $SrZrO_3$ with 2×1×1 orthorhombic $Sr_8Zr_8O_{24}$ cell was constructed and optimized using 4×4×4 Monkhorst-Pack *k*-points meshes. Further, one oxide ion vacancy was introduced by substituting two Y for Zr, creating $Sr_8Zr_6Y_2O_{23}$. Hydrated $Sr_8Zr_6Y_2O_{23}$ supercells, whose respective compositions are described as $Sr_8Zr_6Y_2O_{24}H_2$, was also optimized. On the basis of the optimized unit cell, ZrO_2 supercell with 2×2×2 orthorhombic Zr_4O_8 cell was constructed and optimized using 4×4×2 Monkhorst-Pack *k*-points meshes. Further, one oxide ion vacancy was introduced by substituting one Y for Zr, creating $Zr_4Y_1O_7$. Hydrated $Zr_4Y_1O_7$ supercell, whose composition is described as $Zr_4Y_1O_8H_2$, was also optimized.

Table 4-1 Lattice constant of $SrZrO_3$ and ZrO_2

Solid oxide	Lattice parameter	This work, GGA-PBE	GGA-PBE	LDA	Experiment
$SrZrO_3$ (orthorhombic)	a (Å)	5.70	5.81[4-7]	5.73[4-8]	5.79[4-9]
	b (Å)	5.74	5.87[4-7]	5.80[4-8]	5.82[4-9]
	c (Å)	8.19	8.24[4-7]	8.31[4-8]	8.20[4-9]
ZrO_2 (face-centered-cubic)	a (Å)	5.09	5.11[4-7]	5.03[4-10]	5.09[4-9]

4-3 Results and Discussion

Firstly, stability of SZY and YSZ after hydration were investigated as shown in Table 4-2 and Table 4-3. When lattice energy of hydrated SZY is subtracted from the sum of lattice energy of dehydrated SZY and water molecule, the result is -1.752eV. Likewise, when lattice energy of hydrated YSZ is subtract from the sum of lattice energy of dehydrated YSZ and water molecule, the result is +1.742eV. These results follow the experimental result that hydrated SZY is stable and hydrated YSZ becomes unstable.

Table 4-2 Lattice energy of dehydrated SZY, water molecule, and hydrated SZY.

	dehydrated	H_2O	hydrated
Ce Sr Zr Y O H	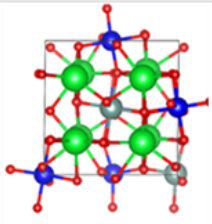		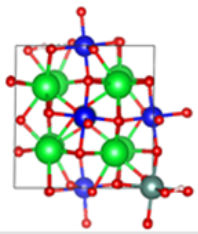
composition	$Sr_8Zr_6Y_2O_{23}$	H_2O	$Sr_8Zr_6Y_2O_{24}H_2$
lattice energy(eV)	-317.2333377	-14.22394767	-333.2099603

Table 4-3 Lattice energy of dehydrated YSZ, water molecule, and hydrated YSZ.

	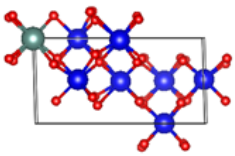		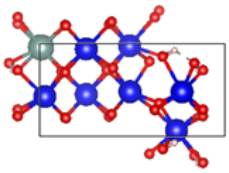
composition	$YSZ(Zr_4Y_1O_7)$	H_2O	$Zr_4Y_1O_7H_2O_1$
lattice energy(eV)	-217.5575122	-14.19737846	-230.0125431

Furthermore, the reason why SZY is stable and YSZ becomes unstable after hydration was investigated. As shown in Figure 4-3, electron density was mapped following respective planes. Those planes follow the coordination of labeled Zr and the nearest oxygen. As shown in Figure 4-4Figure 4-4, the electron density of bonds between Zr and O is analyzed following line a1-b1, a2-b2, c1-d1, and c2-d2. In fact, the covalency from the viewpoints of density of state is discussed by previous study [4-11]. As a result, covalency between Zr and O in SZY is stronger than YSZ. In addition, this results are supported by the result of density of state as shown in Figure 4-5. In addition, as shown in Table 4-3, overlapping ratio of Zr-d orbital on O-p orbital in SZY is greater than YSZ.

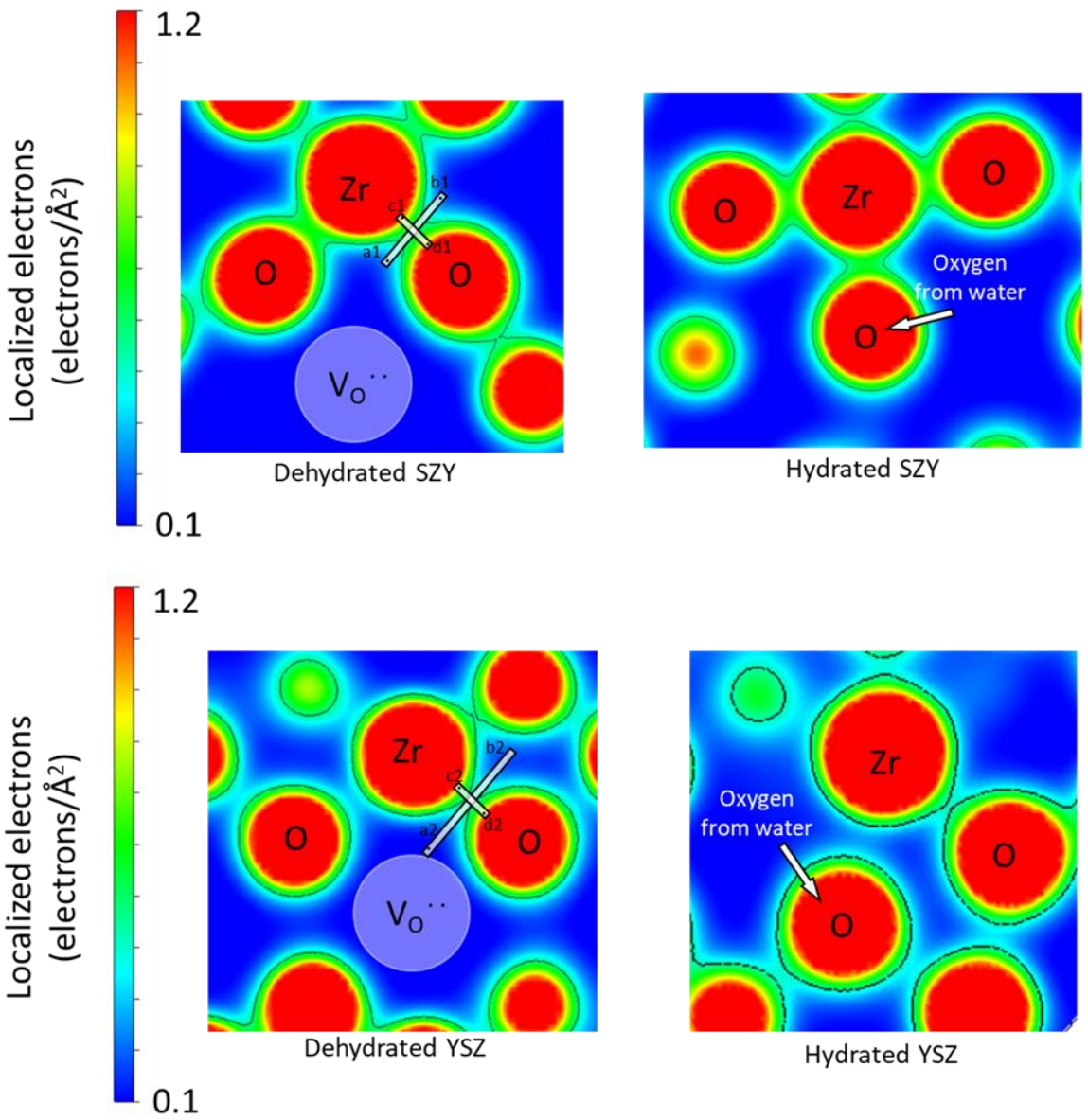

Figure 4-3 Electron density map of dehydrated and hydrated SZY/YSZ

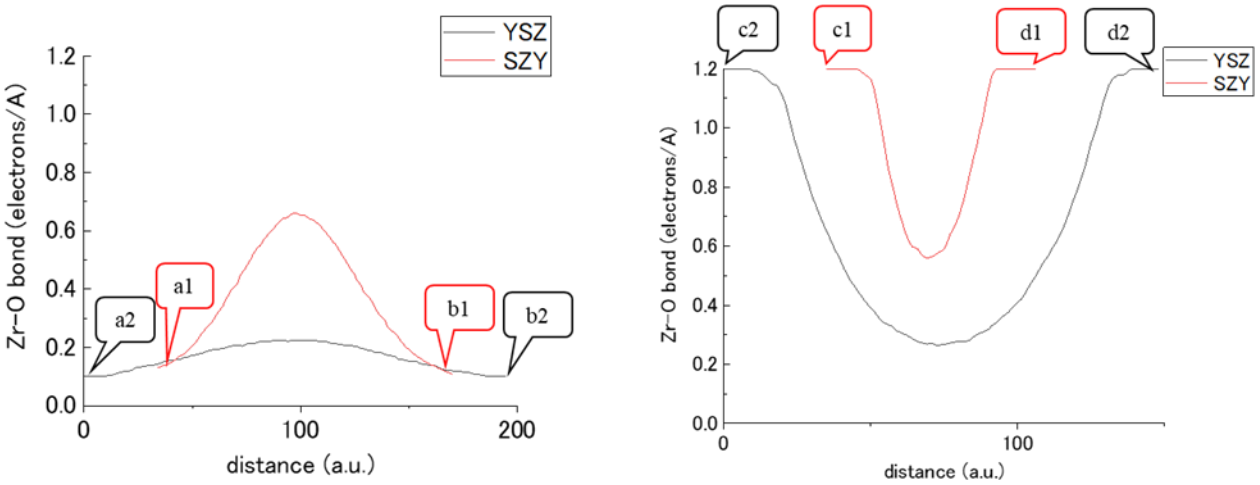

Figure 4-4 Electron density distribution on plot lines for Dehydrated SZY and YSZ

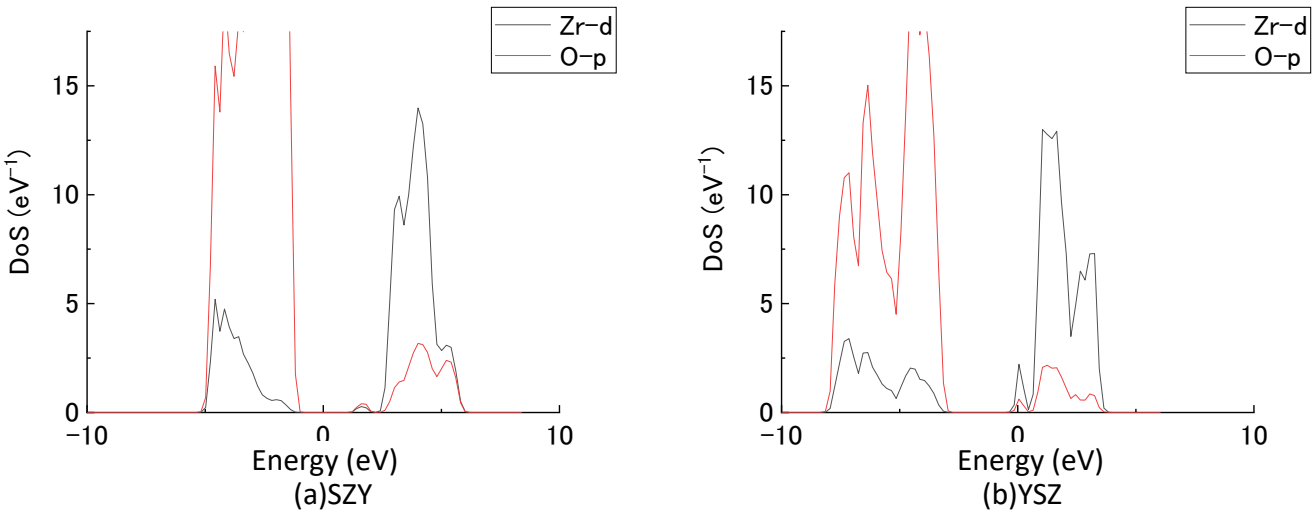

Figure 4-5 Density of state in Zr-d orbital and O-p orbital in SZY and SCY

Table 4-4 Overlapping ratio Zr-d orbital on O-p orbital in YSZ and SZY

	area overlapping between Zr-d and O-p	
	ratio(%)	pixcel
YSZ	100.0	6375
SZY	122.4	7807

Therefore, because of this different covalency between SZY and YSZ, water molecule into SZY can be trapped easier than YSZ as shown in Figure 4-6. Because maximum electron density between Zr and O in SZY is 0.699 electrons/Å^2 and in YSZ is 0.222 electrons/Å^2, as shown in Figure 4-7, 0.450 electrons/Å^2 could be the boundary between oxide ion conductor and proton conducting oxides.

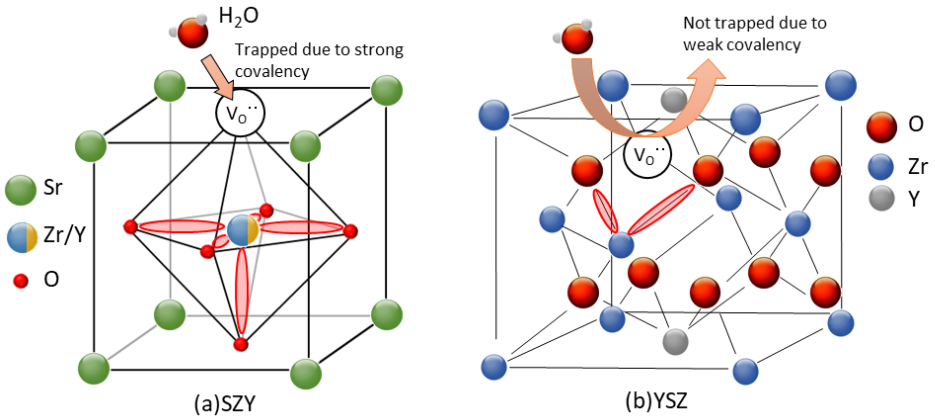

Figure 4-6 Trapped mechanism of water in SZY and YSZ

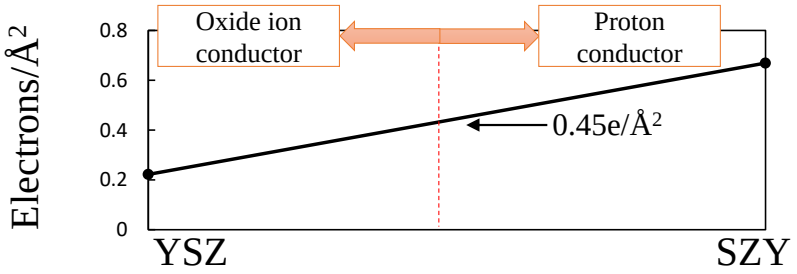

Figure 4-7 The boundary between proton conducting oxides and oxide ion conductor from the view point of Zr-O interface(*B*-O bond)

4-4 Conclusion

This chapter, focusing on bulk SZY and YSZ, investigated covalent bonding with Zr - O by density functional theory. As a result, the covalent bonding nature of SZY is larger than the covalent bonding property of YSZ. Since the hydration enthalpies are positive for YSZ and negative for SZY, this can be interpreted as the water in SZY becomes more stable than YSZ because of the covalent bonding between Zr and oxygen in SZY. It can be one of the reasons why hydration easily takes place in SZY in comparison with YSZ. Furthermore, the author proposes following hydration mechanism which can be one of the reasons why hydration and proton conduction occur in metal oxides having oxygen vacancies. SZY tends to trap oxygen of water. Conversely, since YSZ cannot trap water due to weakness of covalent bonding, it can be said that protons cannot be introduced into the crystal lattice.

Reference

(4-1) Mahato, N.; Banerjee, A.; Gupta, A.; Omar, S.; Balani, K. Progress in Material Selection for Solid Oxide Fuel Cell Technology: A Review. *Prog. Mater. Sci.* **2015**, *72*, 141–337. https://doi.org/10.1016/j.pmatsci.2015.01.001.

(4-2) Kreuer, K. D. Proton-Conducting Oxides. *Annu. Rev. Mater. Res.* **2003**, *33* (1), 333–359. https://doi.org/10.1146/annurev.matsci.33.022802.091825.

(4-3) Kresse, G.; Furthmüller, J. Efficient Iterative Schemes for Ab Initio Total-Energy Calculations Using a Plane-Wave Basis Set. *Phys. Rev. B - Condens. Matter Mater. Phys.* **1996**, *54* (16), 11169–11186. https://doi.org/10.1103/PhysRevB.54.11169.

(4-4) Joubert, D. From Ultrasoft Pseudopotentials to the Projector Augmented-Wave Method. *Phys. Rev. B - Condens. Matter Mater. Phys.* **1999**, *59* (3), 1758–1775. https://doi.org/10.1103/PhysRevB.59.1758.

(4-5) Kresse, G.; Furthmüller, J. Efficiency of Ab-Initio Total Energy Calculations for Metals and Semiconductors Using a Plane-Wave Basis Set. *Comput. Mater. Sci.* **1996**, *6* (1), 15–50. https://doi.org/10.1016/0927-0256(96)00008-0.

(4-6) Perdew, J. P.; Burke, K.; Ernzerhof, M. Generalized Gradient Approximation Made Simple. *Phys. Rev. Lett.* **1996**, *77* (18), 3865–3868. https://doi.org/10.1103/PhysRevLett.77.3865.

(4-7) Jing, Y.; Matsumoto, H.; Aluru, N. R. Mechanistic Insights into Hydration of Solid Oxides. *Chem. Mater.* **2018**, *30* (1), 138–144. https://doi.org/10.1021/acs.chemmater.7b03476.

(4-8) Gomez, M. A.; Jindal, S.; Fletcher, K. M.; Foster, L. S.; Addo, N. D. A.; Valentin, D.; Ghenoiu, C.; Hamilton, A. Comparison of Proton Conduction in KTaO3 and SrZrO3. *J. Chem. Phys.* **2007**, *126* (19), 194701. https://doi.org/10.1063/1.2735592.

(4-9) A. Ahtee, M. Ahtee, A. M. G. and A. W. H. The Structure of Orthorhombic SrZrO3 by Neutron Powder Diffraction. *Acta Crystallogr. Sect. B* **1976**, *B32*, 3243–32463.

(4-10) Ding, H.; Virkar, A. V.; Liu, F. Defect Configuration and Phase Stability of Cubic versus Tetragonal Yttria-Stabilized Zirconia. *Solid State Ionics* **2012**, *215*, 16–23. https://doi.org/10.1016/j.ssi.2012.03.014.

(4-11) Maiti, K. Role of Covalency in the Ground-State Properties of Perovskite Ruthenates: A First-Principles Study Using Local Spin Density Approximations. *Phys. Rev. B - Condens. Matter Mater. Phys.* **2006**, *73* (23), 1–8. https://doi.org/10.1103/PhysRevB.73.235110.

CHAPTER 5

Interface between Pt and proton conducting oxides

5-1 Introduction

The proton conducting oxides ($AB_{1-x}M_xO_{3-\delta}$) having perovskite structure show proton conduction at temperature range between 400 ℃ and 800 ℃ in wet steam atmosphere. It is governed by the following defect equilibriums. An excess of oxygen enters the oxygen vacancies and generates holes with the equilibrium:

$$V_O^{\bullet\bullet} + 1/2\ O_2 \rightleftarrows O_O^{\times} + 2\ h^{\bullet},\ K_1 = \frac{[O_O^{\times}][h^{\bullet}]^2}{[V_O^{\bullet\bullet}]P_{(O_2)}^{\frac{1}{2}}} \quad (5\text{-}1)$$

where $V_O^{\bullet\bullet}$, $O_O^{\times}$,and $h^{\bullet}$ represent oxygen vacancies, lattice oxygen, and holes, respectively. In addition, when oxygen escapes from the oxygen site, electrons are generated with the equilibrium:

$$O_O^{\times} \rightleftarrows V_O^{\bullet\bullet} + 2\ e' + 1/2\ O_2,\ K_2 = \frac{[V_O^{\bullet\bullet}]e'^2 P_{(O_2)}^{\frac{1}{2}}}{[O_O^{\times}]} \quad (5\text{-}2)$$

where e' represents electron. Furthermore, when water goes into oxide-ion vacancies, proton is generated with the equilibrium[5-1]:

$$H_2O + V_O^{\bullet\bullet} + O_O^{\times} \rightleftarrows 2OH_O^{\bullet},\ K = \frac{[OH_O^{\bullet}]}{[O_O^{\times}][V_O^{\bullet\bullet}]P_{(H_2O)}} \quad (5\text{-}3)$$

From above reaction equations, the relation between the electrical conductivity of the proton conducting oxides and the oxygen partial pressure has already been reported[5-2].

In addition to the above defect equilibria, the hetero interface between Pt nano particles and proton conducting oxides has attracted considerable attention. According to previous report, Pt nano particles precipitate from Y-doped strontium zirconate dissolved by Pt in

hydrogen [5-3]. As a result, electric conductivity of Y-doped strontium zirconate having Pt nano particles becomes lower than before Pt nano particles precipitate. By contrast, opposite phenomenon of electrical conductivity was experimentally reported by Takamura *et al.*, and it was shown that the Yb doped strontium cerate had higher conductivity after Pt nano particles precipitate in hydrogen as seen in Figure 5-1. To explain above conductivity behaviors, following hypothesis is established in this study. Firstly, assuming that the work function of Pt is sufficiently smaller than the proton conductor, the charge moves from the former to the latter at the interface between Pt and the proton conductor. Then, as shown in Figure 5-2 (a), cerium can easily change its valence from tetravalent to trivalent by easily entering electrons into the f-orbital. Hence, the electrons do not disturb protons conduction. On the other hand, Zr has orbits only up to d-orbital and it cannot receive electrons. Then, as shown in Figure 5-2 (b), protons in the proton conducting oxides serve as a receiver of electrons. Then, the surroundings of the Pt nanoparticles become insulating layer and disturb the proton conduction. Although previous researchers experimentally reported the phenomena between Pt and above proton conducting oxides, this research in this chapter theoretically evaluated it. By density functional theory (DFT) of first principle calculation, it is evaluated for the hypothesis that the conductivity of both was changed by the above electron flowing behavior between Pt-SZY and Pt-SCYb.

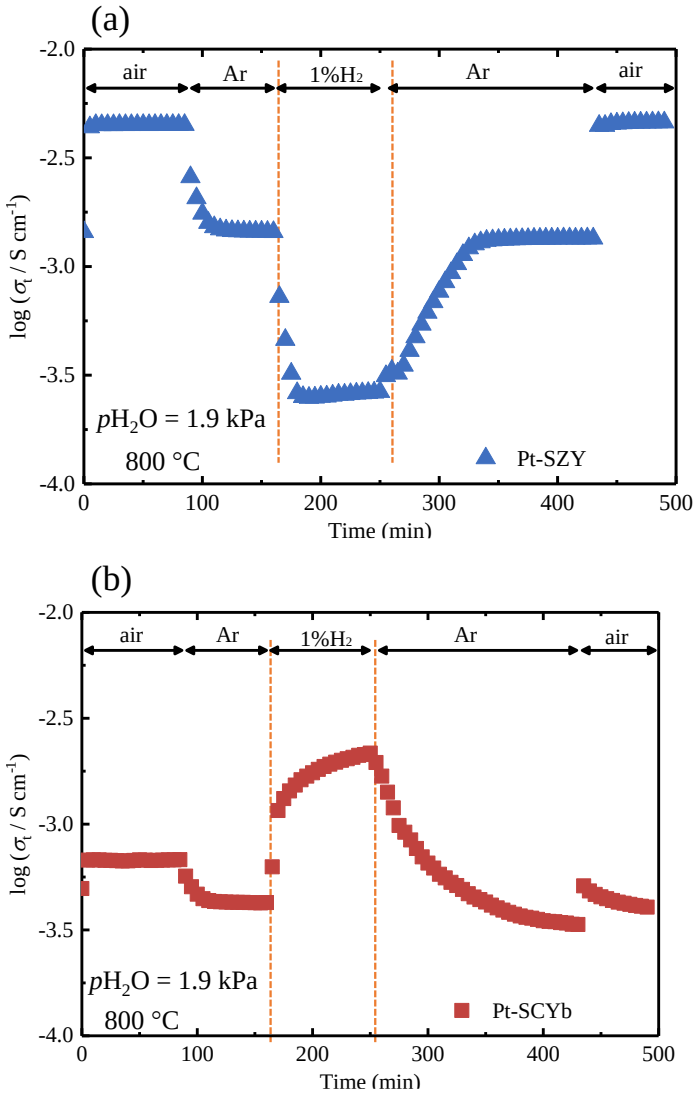

Figure 5-1 Conductivity of the Pt-SZY(a) and Pt-SCYb(b) in various atmosphere. These conductivity was experimentally obtained by Takamura *et al.* [5-4].

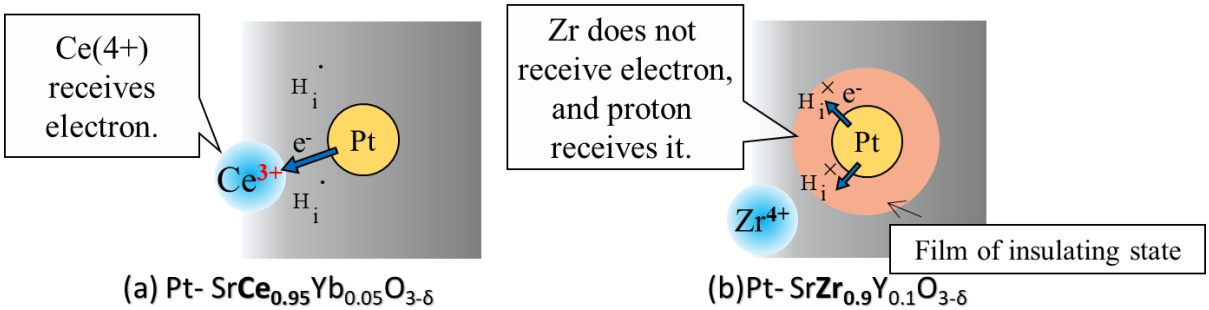

Figure 5-2. Hypothesis: electron flowing behavior between Pt-SCY and Pt-SZY

5-2. Computational details

5-2-1. Geometry optimization

All DFT calculations were performed using the Vienna Ab initio simulation package (VASP) [5-5–7]. The Perdew-Burke-Ernzerhof (PBE) [5-8] exchange-correlation functional was employed based on the projector-augmented wave (PAW) method [5-5]. The cutoff energy for the plane wave basis set was 500 eV for all calculations. A DFT+U approach was applied to the f-orbitals of Ce with a value of U = 5 eV [5-9]. The PAW method pseudopotentials with valence states of Sr (4s, 4p, 5s, 4d), Zr (4s, 4p, 5s, 4d), Ce (5s, 5p, 5d, 4f, 6s), Y (4s, 4p, 5s, 4d), Yb (4f), Pt (6s, 5d) and O (2s, 2p) were used for all calculations. All ionic positions were optimized by a conjugate gradient method until the forces on each ion were below 0.01 eV/Å^2. Spin polarization was not considered during the calculations.

The computed lattice parameters were consistent with those determined experimentally and by DFT calculations in previous reports as shown in Table 5-1[5-10, 5-11, 5-12, 5-13, 5-14]. On the basis of the optimized unit cell, $SrZrO_3$ and $SrCeO_3$ supercells with 2×1×1 orthorhombic $Sr_8Zr_8O_{24}$ and 2×1×1 orthorhombic $Sr_8Ce_8O_{24}$ cells were constructed and optimized using 2×4×3 and 2×4×3 Monkhorst-Pack *k*-points meshes, respectively. Further, one oxide ion vacancy was introduced by substituting two Y for Ce creating $Sr_8Zr_6Y_2O_{23}$. In addition, to create and $Sr_8Ce_6Yb_2O_{23}$, one oxide ion vacancy was introduced by substituting two Y for Zr. Hydrated $Sr_8Zr_6Y_2O_{23}$ and $Sr_8Ce_6Yb_2O_{23}$ supercells, whose respective compositions are described as $Sr_8Zr_6Y_2O_{24}H_2$ and $Sr_8Ce_6Yb_2O_{24}H_2$, were also optimized. Furthermore, Pt unit cell was also optimized with 5×5×5 Monkhorst-Pack *k*-points mesh. Then, Pt supercell was created with 3×1×1 cubic structure of Pt unit cell.

To make the model of interface between Pt and proton conducting oxides, optimized Pt supercell was attached with $Sr_8Zr_6Y_2O_{23}$, $Sr_8Ce_6Yb_2O_{23}$, $Sr_8Zr_6Y_2O_{24}H_2$, or $Sr_8Ce_6Yb_2O_{24}H_2$. Then, all models of interface were optimized with 4×2×1 Monkhorst-Pack *k*-points meshes.

Table 5-1 Calculated and experimental lattice parameters of $SrZrO_3$, $SrCeO_3$ and Pt

Solid oxide	Lattice parameter	This work, GGA-PBE	GGA-PBE	Experiment
$SrZrO_3$ (orthorhombic)	a (Å)	5.70	5.81[5-10]	5.79[5-11]
	b (Å)	5.74	5.87[5-10]	5.82[5-11]
	c (Å)	8.19	8.24[5-10]	8.20[5-11]
$SrCeO_3$ (orthorhombic)	a (Å)	6.07	5.94[5-12]	6.01[5-12]
	b (Å)	6.24	6.10[5-12]	6.15[5-12]
	c (Å)	8.70	8.51[5-12]	8.60[5-12]
Pt (cubic)	a(Å)	3.98	3.99[5-14]	3.92[5-13]

5-2-2 Bader analysis

To evaluate if they obtain electrons from Pt in $Sr_8Zr_6Y_2O_{23}$, $Sr_8Ce_6Yb_2O_{23}$, $Sr_8Zr_6Y_2O_{24}H_2$, or $Sr_8Ce_6Yb_2O_{24}H_2$, bader analysis is performed. This section explains the bader analysis. As shown in Figure 5-3, the bader analysis separates charge density between two atoms at minimum charge density. Bader's theory was designed for analyzing charges in molecules, but many reports show that bader analysis is effective to evaluate the charge density in metal oxides [5-15,16].

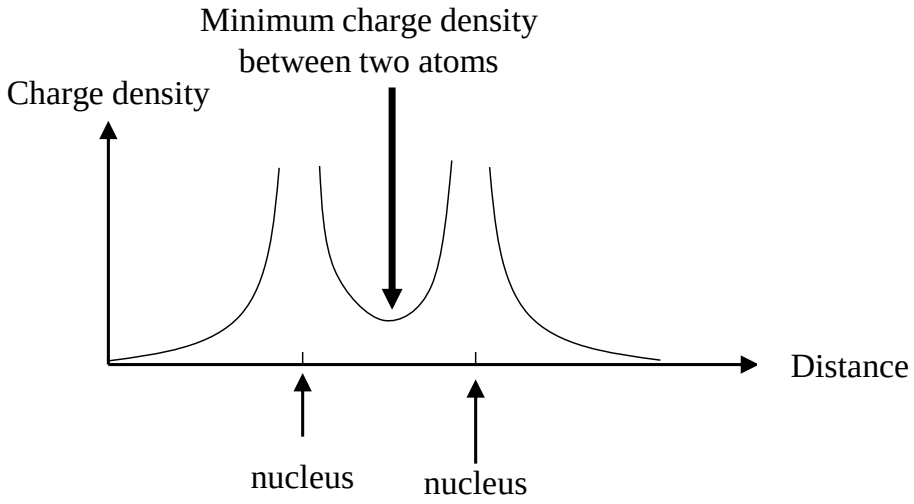

Figure 5-3 Schematic model cut position of charge density between two atoms by bader analysis.

5-2-3 Evaluation of workfunction

To support the results of bader analysis, workfunction of Pt and hydrated/dehydrated $Sr_8Ce_6Yb_2O_{23}$ was evaluated. Vacuum layer having approximately 10 Å height was formed in one direction of optimized proton conducting oxides (hydrated/dehydrated $Sr_8Ce_6Yb_2O_{23}$). The structure of the proton conducting oxides having this vacuum chamber was optimized, and the electrostatic potential at the center was calculated.

In particular, the electrostatic potential was evaluated by DFT with respect to the center of the cell. In the proton conducting oxides, the electrostatic potential is strongly influenced by the potential of constituent atoms. On the other hand, in the vacuum level, the electrostatic potential settles at a certain electrostatic potential when the influence by the polarization from the proton conducting oxides is sufficiently small. Then, the static level settled at that fixed potential in the vacuum was evaluated as vacuum level. This method has been performed in many research and it is known as technique to evaluate

vacuum level of metal oxide including perovskite structure[5-17–19]. Furthermore, when the structure of the vacuum layer and the slab structure of the proton conductive oxide are optimized, the Fermi level of the proton conductive oxide is outputted by DFT. It is possible to get work related by subtracting the obtained vacuum order and Fermi level.

5-3 Results

5-3-1 Charge transfer investigation by bader analysis

Figure 5-4 shows the structure optimized proton conducting oxides. As shown in the Table 5-1, it was shown that charge transfer direction between Pt and respective proton conducting oxide. Only hydrated $Sr_8Ce_6Yb_2O_{23}$ ($Sr_8Ce_6Yb_2O_{24}H_2$) obtains electrons from Pt, and other compositions do not obtain electrons from Pt. As shown in Figure 5-5 which is created by Table 5-3, the amount of electron transfer of cerate was almost half smaller than that of zirconate. In case of only hydrated Yb-doped $SrCeO_3$ (SCYb+H_2O), electron was transferred from Pt to hydrated SCYb+H_2O by approximately 0.1 electrons.

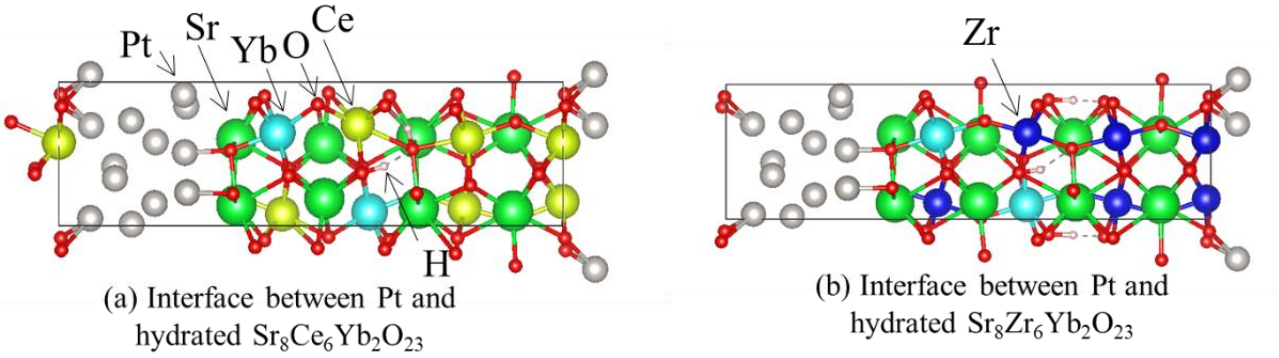

(a) Interface between Pt and hydrated $Sr_8Ce_6Yb_2O_{23}$

(b) Interface between Pt and hydrated $Sr_8Zr_6Yb_2O_{23}$

Figure 5-4 Optimized interface between Pt and proton conducting oxides

Table 5-2 Direction of charge transfer of hydrated/dehydrated Y/Yb-doped strontium cerate/zirconate

(a) Hydrated/dehydrated Yb/Y-doped strontium cerate

Pt	Direction of Charge Transfer	Composition
Pt	←	$Sr_8Ce_6Y_2O_{23}$
	←	$Sr_8Ce_6Yb_2O_{23}$
	←	$Sr_8Ce_6Y_2O_{24}H_2$
	→	$Sr_8Ce_6Yb_2O_{24}H_2$

(b) Hydrated/dehydrated Yb/Y-doped strontium zirconate

Pt	Direction of Charge Transfer	Composition
Pt	←	$Sr_8Zr_6Y_2O_{23}$
	←	$Sr_8Zr_6Yb_2O_{23}$
	←	$Sr_8Zr_6Y_2O_{24}H_2$
	←	$Sr_8Zr_6Yb_2O_{24}H_2$

Table 5-3 The amount of charge transfer (electron transfer) from proton conducting oxides to Pt. (negative value describes charge transfer from Pt to proton conducting oxides.)

Composition	The amount of charge transfer (electrons)
$Sr_8Ce_6Y_2O_{23}$	0.36787
$Sr_8Ce_6Y_2O_{24}H_2$	0.37233
$Sr_8Ce_6Yb_2O_{23}$	0.10813
$Sr_8Ce_6Yb_2O_{24}H_2$	-0.10813
$Sr_8Zr_6Y_2O_{23}$	0.62124
$Sr_8Zr_6Y_2O_{24}H_2$	0.60935
$Sr_8Zr_6Yb_2O_{23}$	0.54039
$Sr_8Zr_6Yb_2O_{24}H_2$	0.32074

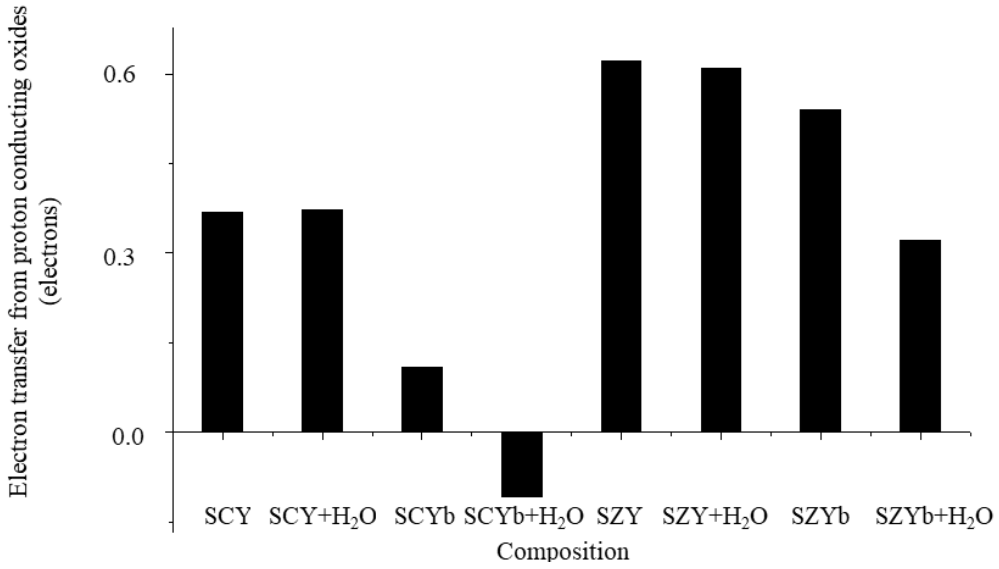

Figure 5-5 The amount of electron transfers from respective proton conducting oxides to Pt. This figure is created based on Table 5-3. (Negative value describes charge transfer from Pt to proton conducting oxides.) SCY: $Sr_8Ce_6Y_2O_{23}$, SCY+H_2O: $Sr_8Ce_6Y_2O_{24}H_2$, SCYb: $Sr_8Ce_6Yb_2O_{23}$, SCYb+H_2O: $Sr_8Ce_6Yb_2O_{24}H_2$, SZY: $Sr_8Zr_6Y_2O_{23}$, SZY+H_2O: $Sr_8Zr_6Y_2O_{24}H_2$, SZYb: $Sr_8Zr_6Yb_2O_{23}$, SZYb+H_2O: $Sr_8Zr_6Yb_2O_{24}H_2$.

.

5-3-2 Evaluation of workfunction

The Figure 5-6 shows respective proton conducting oxides having a vacuum slab (left side in the figure) and their electrostatic potential (right side in the figures). The electrostatic potential obtained in the vacuum slab, and the work function was calculated with the Fermi level obtained by geometry optimization. As a result, the work function of $Sr_8Ce_6Y_2O_{23}$ and hydrated $Sr_8Ce_6Y_2O_{23}$ ($Sr_8Ce_6Y_2O_{24}H_2$) is smaller than that of Pt, which results in supporting the analysis in section 4-4-1. Firstly, in the case of Pt, the work function was evaluated to be 5.7 eV as shown in the Figure 5-6 (a2). Because this number is consistent with the experimental number of 5.7 eV conducted by Bouwman *et al.*[5-20], it can be said that DFT evaluates the workfunction of Pt very accurately. On the other

hand, in the case of the Y-doped $SrCeO_3$, the dehydrated cerate and the hydrated cerate were evaluated as work functions of 1.44 eV and 1.88 eV, respectively. These numbers were considerably smaller than the workfunction of Pt.

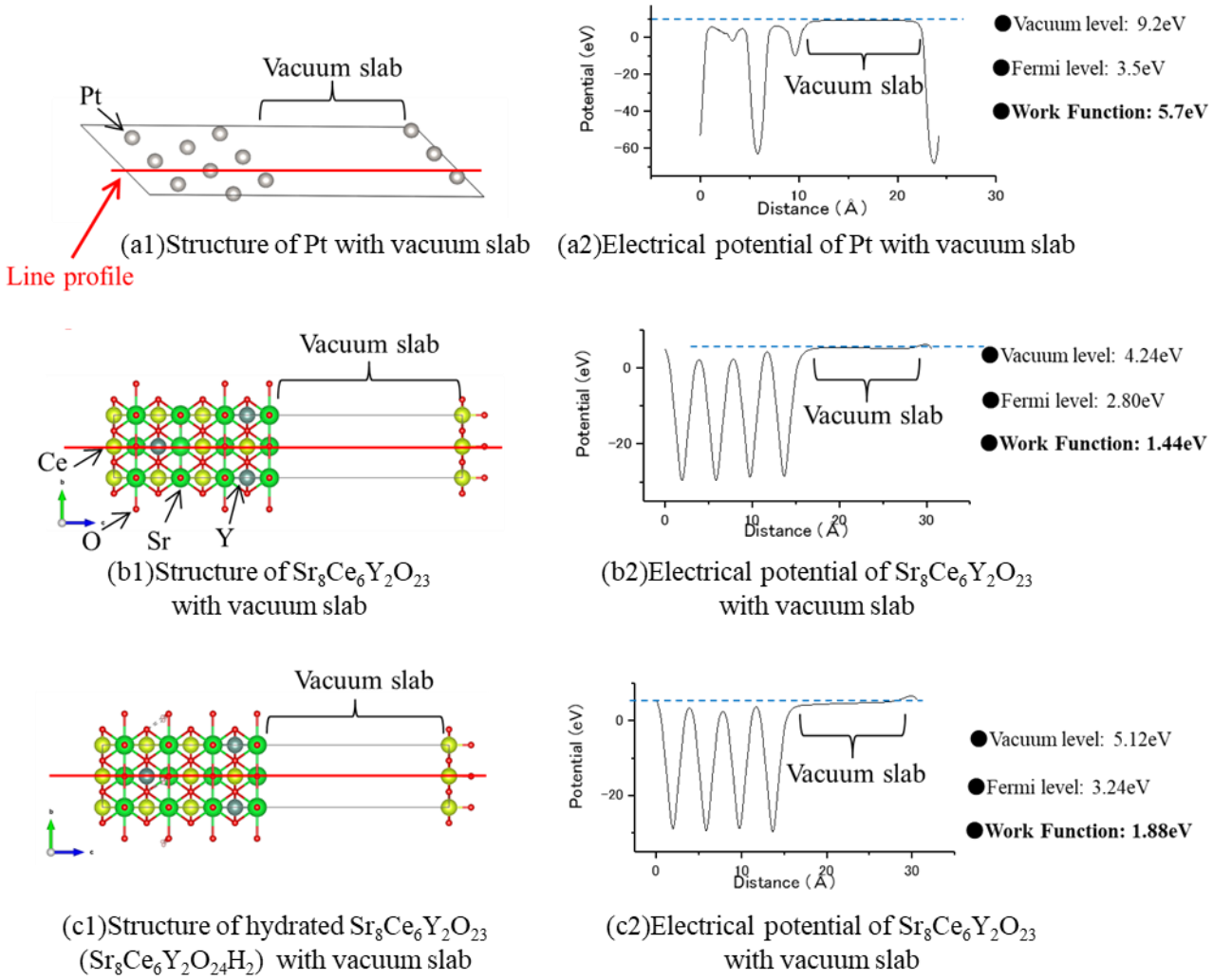

Figure 5-6 Workfunction of Pt, $Sr_8Ce_6Y_2O_{23}$ and hydrated $Sr_8Ce_6Y_2O_{23}$ ($Sr_8Ce_6Y_2O_{24}H_2$).

5-4 Discussion

The hypothesis in Figure 5-2 suggested the possibility of electron transfer occurring from Pt to proton conducting oxides at the interface. However, the transfer direction indicated by density functional theory mainly showed the opposite direction to the hypothesis except $Sr_8Ce_6Yb_2O_{24}H_2$. The result obtained by density functional theory is that of the interface between the thin film of Pt and proton conducting oxides. However, the following unresolved problem exists. It was reported that the work function of the perovskite structure changes depending on the atoms exposed on the surface. As shown in the Figure 5-7, focusing on *B*O-terminated Sr*B*O_3, it is found that the work function is doubled as compared with *A*O-terminated as seen in Figure 5-8 [5-21]. Therefore, there is possibility that the same thing can happen even in the composition as the research subject this time.

In addition, with regard to Pt, the smaller Pt nano particles could lead to make the work function become smaller. As reported by Khoa *et al.*, Au nanoparticle whose diameter is 5 nm become 0.4 eV smaller than that at 50 nm as seen in Figure 5-9 [5-22]. Therefore, when the surface of the present proton conductor is *B*O-terminated and Pt is nanoparticles of 5 nm or less, there is a possibility that electrons move from Pt to the proton conductor.

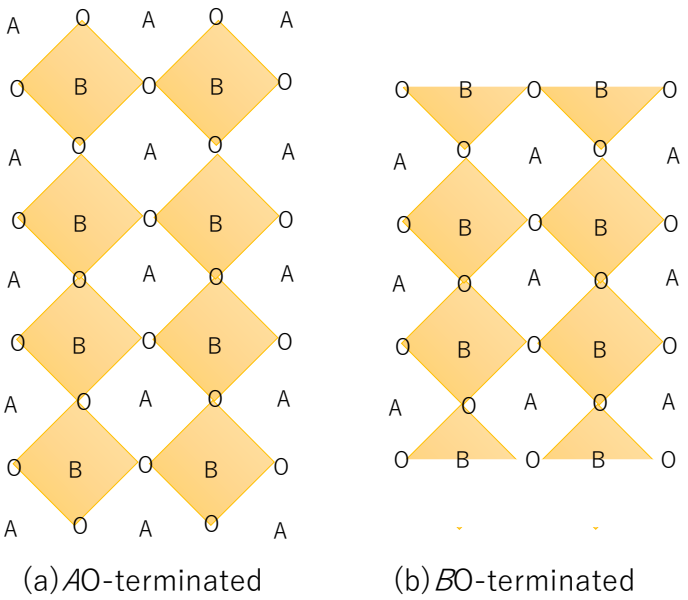

Figure 5-7 Perovskite structure (ABO_3) of respective surface based on the report of Jacobs *et al.*. (a)*A*O terminated, (b)BO_2 terminated [5-21].

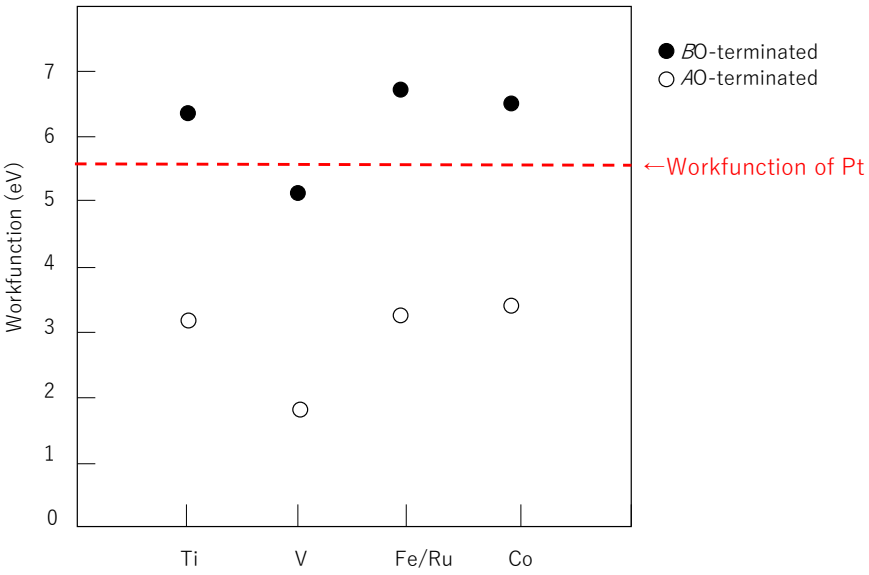

Figure 5-8 The workfunction for *A*O- and BO_2-terminated surface in respective types of Y-doped Sr*M*O_3 by Jacobs *et.al.*[5-21]. Pt workfunction is reported by Fowler *et al.*[5-23].

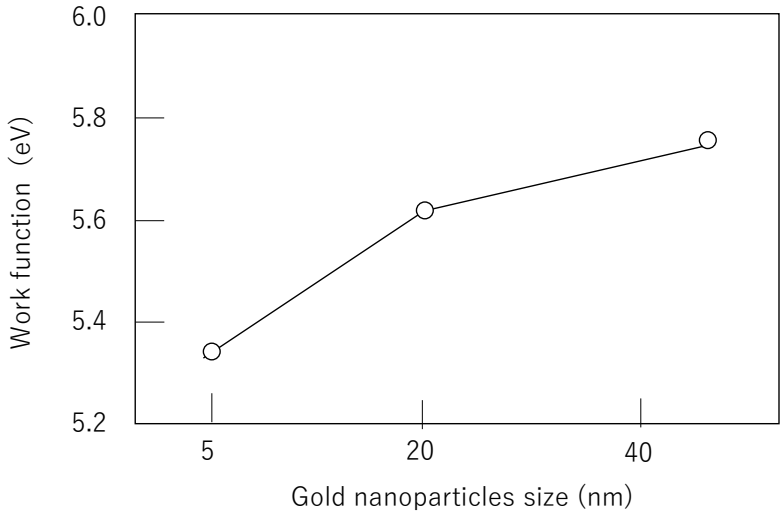

Figure 5-9 Au workfunction change as function of particle size reported by Khoa [5-22].

5-5 Conclusion

In this chapter, the flow of electrons at the interface between proton conducting oxides (Y-doped $SrCeO_3$ and Y-doped $SrZrO_3$) and Pt nanoparticles was evaluated by DFT. In the initial hypothesis, this study had considered that the workfunction of Pt is larger than that of the proton conducting oxides, and that Pt supplies electrons to them. However, the results of DFT showed the opposite tendency to the hypothesis. According to the previous study, if the *B*-site of the perovskite structure is exposed on the surface and Pt is precipitated in the proton conducting oxides as nanoparticles with several nanometers, it is speculated to obtain results supporting the above hypothesis. In addition, the crystal structure used for this calculation had to use a thin film due to calculation cost. Therefore, it could be also necessary to evaluate not the thin film but the bulk crystal structure.

Reference

(5-1) Matsumoto, H., Technol, S. & Mater, A. Nanoionics phenomenon in proton-conducting oxide : Effect of dispersion of nanosize platinum particles on electrical conduction properties Nanoionics phenomenon in proton-conducting oxide : Effect of dispersion of nanosi. (2007). doi:https://doi.org/10.1016/j.stam.2007.09.008

(5-2) Somekawa, T. *et al.* Physicochemical properties of Ba(Zr,Ce)O3-Δ-based proton-conducting electrolytes for solid oxide fuel cells in terms of chemical stability and electrochemical performance. *Int. J. Hydrogen Energy* **42,** 16722–16730 (2017).

(5-3) Matsumoto, H. *et al.* Nanoprotonics in perovsikte-type oxides: Reversible changes in color and ion conductivity due to nanoionics phenomenon in platinum-containing perovskite oxide. *Solid State Ionics* **182,** 13–18 (2011).

(5-4) Takamura, Y., Leonard, K. & Matsumoto, H. Effect of Dispersion of Platinum Nanoparticles in Strontium Zirconate and Strontium Cerate Proton Conductors. *Meet. Abstr. No. 32. Electrochem. Soc.* 1943 (2018).

(5-5) Kresse, G. & Furthmüller, J. Efficient iterative schemes for ab initio total-energy calculations using a plane-wave basis set. *Phys. Rev. B - Condens. Matter Mater. Phys.* **54,** 11169–11186 (1996).

(5-6) Joubert, D. From ultrasoft pseudopotentials to the projector augmented-wave method. *Phys. Rev. B - Condens. Matter Mater. Phys.* **59,** 1758–1775 (1999).

(5-7) Kresse, G. & Furthmüller, J. Efficiency of ab-initio total energy calculations for metals and semiconductors using a plane-wave basis set. *Comput. Mater. Sci.* **6,** 15–50 (1996).

(5-8) Perdew, J. P., Burke, K. & Ernzerhof, M. Generalized gradient approximation made simple. *Phys. Rev. Lett.* **77,** 3865–3868 (1996).

(5-9) Chen, Y., Hu, P., Lee, M. H. & Wang, H. Au on (1 1 1) and (1 1 0) surfaces of CeO2: A density-functional theory study. *Surf. Sci.* **602,** 1736–1741 (2008).

(5-10) Gomez, M. A. *et al.* Comparison of proton conduction in KTaO3 and SrZrO3. *J. Chem. Phys.* **126,** 194701 (2007).

(5-11) A. Ahtee, M. Ahtee, A. M. G. and A. W. H. The structure of orthorhombic SrZrO3 by neutron powder diffraction. *Acta Crystallogr. Sect. B* **B32,** 3243–32463 (1976).

(5-12) Swift, M. Impact of point defects on proton conduction in strontium cerate. *J. Phys. Chem. C* **120,** 9562–9568 (2016).

(5-13) Patra, A., Bates, J. E., Sun, J. & Perdew, J. P. Properties of real metallic surfaces : Effects of density functional semilocality and van der Waals nonlocality. 9188–9196 (2017). doi:https://doi.org/10.1073/pnas.1713320114

(5-14) Armiento, R. & Mattsson, A. E. Functional designed to include surface effects in self-consistent density functional theory. *Phys. Rev. B - Condens. Matter Mater. Phys.* **72,** 1–5 (2005).

(5-15) Wu, M., Tse, J. S., Wang, S. Y., Wang, C. Z. & Jiang, J. Z. Origin of pressure-induced crystallization of Ce75Al25 metallic glass. *Nat. Commun.* **6,** 1–7 (2015).

(5-16) Tang, W., Sanville, E. & Henkelman, G. A grid-based Bader analysis algorithm without lattice bias. *J. Phys. Condens. Matter* **21,** 084204 (2009).

(5-17) Foley, B. J. *et al.* Temperature dependent energy levels of methylammonium lead iodide perovskite. *Mater. Eng. Sci. Div. 2015 - Core Program. Area 2015 AIChE Annu. Meet.* **243904,** 581–586 (2015).

(5-18) Ganose, A. M., Butler, K. T., Walsh, A. & Scanlon, D. O. Relativistic electronic structure and band alignment of BiSI and BiSeI: Candidate photovoltaic materials. *J. Mater. Chem. A* **4,** 2060–2068 (2016).

(5-19) Stevanović, V., Lany, S., Ginley, D. S., Tumas, W. & Zunger, A. Assessing capability of semiconductors to split water using ionization potentials and electron affinities only. *Phys. Chem. Chem. Phys.* **16,** 3706–3714 (2014).

(5-20) Bouwman, R. & Sachtler, W. M. H. Photoelectric determination of the work function of gold-platinum alloys. *J. Catal.* **19,** 127–139 (1970).

(5-21) Jacobs, R., Booske, J. & Morgan, D. Understanding and Controlling the Work Function of Perovskite Oxides Using Density Functional Theory. *Adv. Funct. Mater.* **26,** 5471–5482 (2016).

(5-22) Khoa, N. T., Kim, S. W., Yoo, D. H., Kim, E. J. & Hahn, S. H. Size-dependent work function and catalytic performance of gold nanoparticles decorated graphene oxide sheets. *Appl. Catal. A Gen.* **469,** 159–164 (2014).

(5-23) Fowler, J. D., Virji, S., Kaner, R. B. & Weiller, B. H. Hydrogen detection by Polyaniline nanofibers on gold and platinum electrodes. *J. Phys. Chem. C* **113,** 6444–6449 (2009).

CHAPTER 6

Anomalous conductivity observed in dry hydrogen

6-1 Introduction

In the previous chapters, they have mainly evaluated properties of proton conducting oxides by using first principles calculation. This chapter explains the experimental result of investigation on specific electric conductivity expressed in a proton conducting oxide.

As shown in the previous chapters, the proton conduction is occurred as the result hydration reaction following equation 6-1 [6-1]. After the first proton conducting oxides were reported by Iwahara *et al.* in 1981 [6-2], proton conductivity in various compositions has been confirmed [6-3]. The activation energy of them is between approximately 0.4 - 0.5 eV. To obtain higher proton conductivity, some researchers have attempted to lower the resistance value by using thin films [6-4,6-5, 6-6]. As seen in Figure. 6-1, and equation 6-2 , resistance can be decreased, which will lead to improve the performance of proton conducting oxides. However, as long as the activation energy of the proton conducting oxides is in the above range, there are currently limited methods for obtaining a novel proton conducting oxides having high proton conductivity.

$$H_2O + V_O^{\bullet\bullet} \rightleftarrows O_O^{\times} + 2H_i^{\bullet} \qquad (6\text{-}1)$$

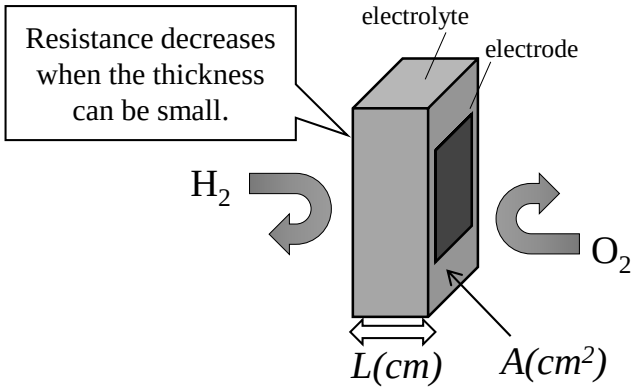

Figure. 6-1 Shimatic model of thin film electrolyte of a proton conducting oxide

$$R = \frac{L}{\sigma A} \qquad (6\text{-}2)$$

, where R, L, σ, and A are resistance, length, conductivity, and area of proton conducting oxides, respectively.

Recently, Zenitani *et al.* reported that exposed a thin film proton conducting oxide to dry hydrogen and obtained high electrical conductivity. According to them, such high conductivity with Y- doped $BaZrO_3$ is the red line in Figure 6-2 [6-7,6-8]. This conductivity is significantly larger than the conventional conductivity of bulk and film of Y-doped $BaZrO_3$. The activation energy is calculated as 0.1 eV and it is not explicable from the viewpoint of proton conduction by hydration reaction. There is possibility that some proton conducting oxides still have undiscovered conduction mechanism. In addition, Zenitani *et al.* also reported that sufficient amount of hydrogen exists over 0.5 μm from the outermost surface of the thin film, and they suggested that hydrogen itself could be the conduction causing such high conductivity. In fact, exposing to dry hydrogen at a temperature close to 600 ° C of a proton conducting oxides has been considered as taboo, because electron conductivity is induced by reducing the sample following

$$1/2\ H_2 + O_O^{\times} = OH_O^{\bullet} + e' \qquad (6\text{-}3)$$

, where e' is electrons. However, they also succeeded in measuring electromotive force,

and also showed that only electrons are hard to conceive as conduction species.

This research is inspired by the research by Zenitani *et al.*, and aimed to elucidate the mechanism of the conduction of unknown electric conductivity. Thin films are thought to be more susceptible to substrates and electrodes than bulk samples as seen in Figure 6-3. It is better to use a bulk sample to investigate the influence of the sample itself. Also, this research focused on Y- doped $SrZrO_3$, not $BaZrO_3$ that previous research showed. It is because the Ba in $BaZrO_3$ may evaporate to some extent at high temperature around 600 ℃, which may lead to changing the composition [6-9,6-10]. There is also a report that Y- doped $SrZrO_3$ is less likely to form grain boundaries compared to $BaZrO_3$ [6-11]. Therefore, the authors focused on Y- doped $SrZrO_3$ which seems to be more appropriate for evaluating the unknown conductivity observed in dry hydrogen.

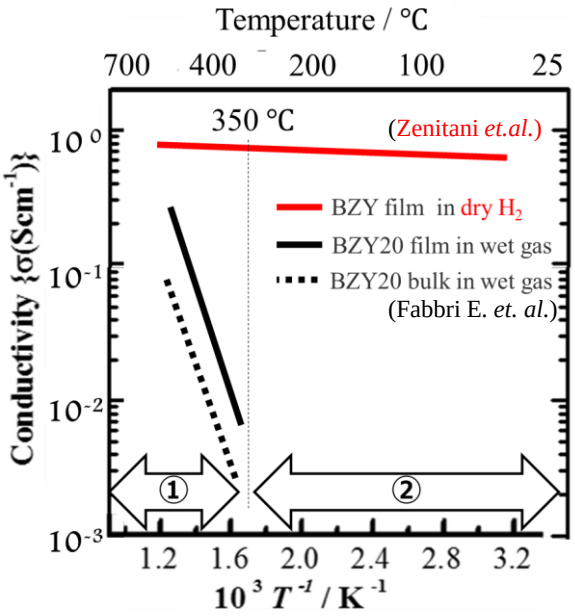

Figure 6-2 The reported conductivity of Y-doped $BaZrO_3$ in dry H_2 by Zrnitani *et al.*. The black line and dotted line show the conventional conductivity observed in wet atomoshphere [6-7,6-8].

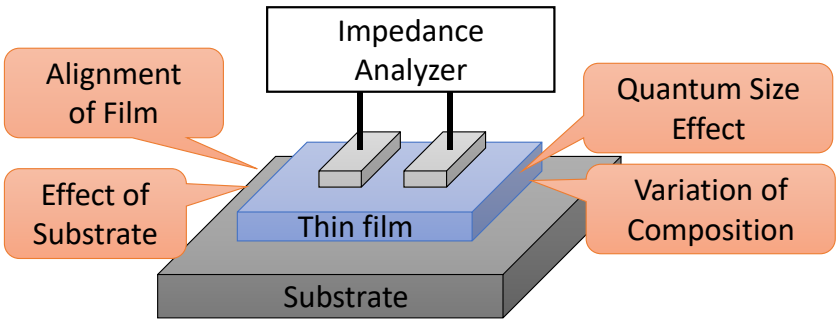

Figure 6-3 Uncertainties on thin films

6-2 Methodology

6-2-1 Sample preparation and X-Ray Diffraction Analysis

$SrZr_{0.9}Y_{0.1}O_{3-\delta}$ (SZY91) known as a composition of proton conducting oxide was prepared by a solid state reaction method [6-12]. $SrCO_3$ (RARE METALLIC Corp., Kyoto, Japan), ZrO_2 (Mitsuwa Chemicals Corp., Osaka, Japan) , Y_2O_3 (Tosoh Corp., Yamaguchi, Japan) were appropriately weighed, mixed in a zirconia mortar with ethanol and calcined at 1350°C for 10 h in air with . Calcined specimen was grinded by planetary ball-milling with 15mm-φ zirconia balls at 300 rpm for 1 h. with ethanol as a dispersant. Obtained powder was dried in vacuum oven at 120°C. The dried powder was molded and cold iso-statically pressed at 250 MPa to obtain bar shaped and disk shaped SZY91.

Finally, these samples were sintered at 1600 ℃ to obtain dense electrolyte (the relative density >95%). To analyze the crystal structure of the sintered SZY91, X-ray diffraction (XRD) was conducted at room temperature with X-ray diffractometer (Rigaku Inc., Ultima IV, Tokyo, Japan) using Cu-Kα radiation.

6-2-2 Principle of four-probe technique

To obtain precise resistance of SZY91, the four-probe technique was performed. It is useful for avoiding ohmic loss between two points on substance. In the two-probe technique as shown in Figure 6-4(a), the voltage difference between the two points is measured as a function of the current and the resistance is determined following ohm's law. The disadvantage of this technique is that resistant obtaining includes resistance from electrode reactions and lead wire. On the other hand, four-probe technique as shown in Figure 6-4 (b) can be performed to avoid the resistance of them. The outer two probes in the figure deliver a current, and the inner two probes are used to measure voltage. The ohmic resistance can be determined without effect of contact resistance between the probes and the substance [6-13].

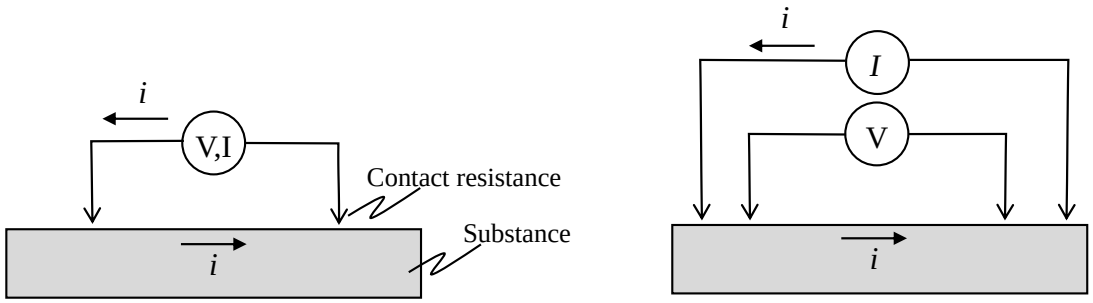

Figure 6-4 Two-(a) and four-(b) probe techniques for ohmic resistance measurement

6-2-3 Electrical conductivity measurement

The figure shows the schematic model of experimental device to measure the electrical conductivity of SZY91. This device can introduce arbitrary gas to the sample in the furnace. The furnace can increase temperature between room temperature and 1000℃.

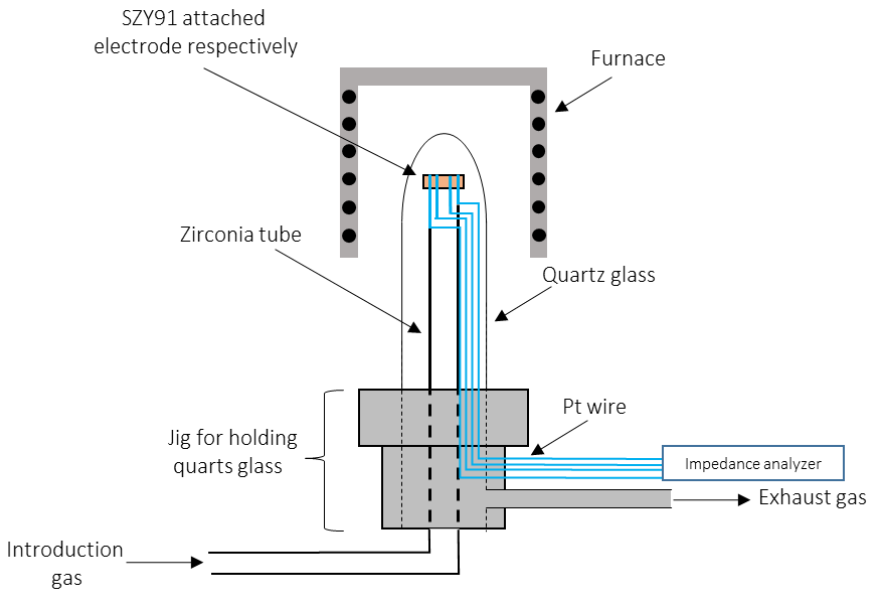

Figure 6-5. Schematic illustration of the device used for conducting measurement in dry hydrogen gas.

6-2-3-1 Silver vs. platinum electrode

The influence of the difference between the Pt electrode and the Ag electrode on the electric conductivity in dry H_2 was investigated for sintered SZY91. The dry H_2 to be handled in this experiment has the humidity below -40 ° C of dew point with dew point hygrometer (Tokyo Opto-Electronics Co., DPH-503). The Pt electrode and the Ag electrode were prepared to bake at 900 ° C and 200 ° C, respectively. While exposing the sample to 100% dry H_2, the temperature was raised from room temperature to 900 ° C every 100 ° C, and then the temperature was lowered with steps every 100 ° C. The rate of temperature change was set to 5 ° C/min.. Approximately 30 minutes after reaching the temperature of each step, the impedance was measured by the impedance measuring device (Versastat4, TOYO Corp, Japan) at each temperature.

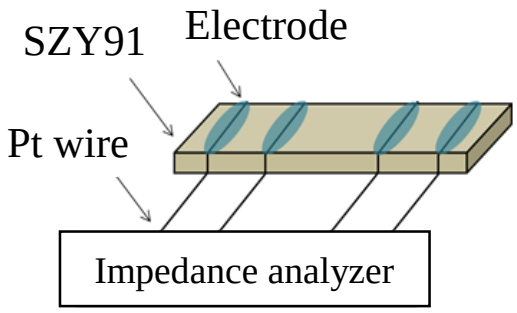

Figure 6-5 Schimatic model of four probe technique for SZY91

6-2-3-2 Hydrogen gas pressure dependence

The influence of 1% hydrogen gas (99% Ar) on electric conductivity was investigated for SZY 91 with Ag electrode. After Ag electrode was prepared on SZY 91 at 200 ° C with small electric furnace for 1 hour, electric conductivity was measured by impedance spectroscopy. The temperature was raised to 600 ° C and held for 1 hour at 600 ° C, after which the impedance was measured from 600 ° C to 100 ° C.

6-2-3-3 Bar-shaped SZY91 and position of electrode

To investigate the effect of electric conductivity due to the difference in position of the Ag electrode, the electrode was attached to the position as seen Figure 6-6. The Ag electrode was attached to both sides of bar type SZY91, and impedance measurement was attempted by the a.c. 2-probe technique. The temperature in dry H_2 was raised to 800 ° C from room temperature, and then it was maintained at 800 ° C for 1 hour. Then, the impedance was measured at every 100 °C step 10 minutes after reaching at desired temperature.

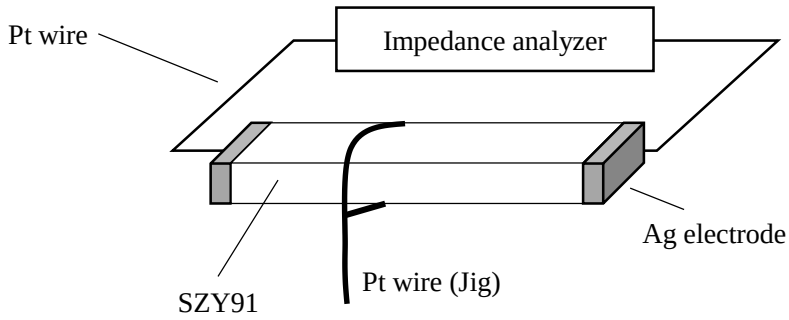

Figure 6-6 Schimatic model of Ag electrode position on the side of SZY91

6-2-3-4 Disk-shaped SZY91 and position of electrode

The electric conductivity of disk-shaped SZY91 was measured by the following two arrangements of Ag electrodes. First, as shown in Figure 6-7, two Ag electrodes were attached on top side and bottom side of SZY91. Impedance measurement was performed by the a.c. 2-probe technique, and the electric conductivity was calculated by equation (6-2). Secondly, Ag electrode of next SZY91 was placed in two places on the same surface as shown in the figure. A hole as seen in Figure 6-8 was drilled in the center of the disk-shaped SZY91 and Ag electrode was placed at the edge of the hole as first part. Then, Ag electrode as a second part was installed at another edge. The electric conductivity was obtained as following equation

$$\sigma = \frac{l}{R \cdot 2\pi r t} = \frac{l}{R \cdot 2\pi t} \int_{r_1}^{r_2} \frac{1}{r}\, dr = \frac{l}{2R\pi t} \ln \frac{r_2}{r_1} \qquad (6\text{-}4)$$

The parameters in the Figure 6-9 are in agreement with the ones in Figure 6-8.

The temperature of the two samples was raised from room temperature to 900 ° C, then held for 1 hour at 900 ° C, and then cooled down to 100 ° C. The temperature change was kept at 5 ° C/min. toward room temperature. Approximately 30 minutes after reaching every 100 ° C, the impedance was measured by the a.c. two-probe technique.

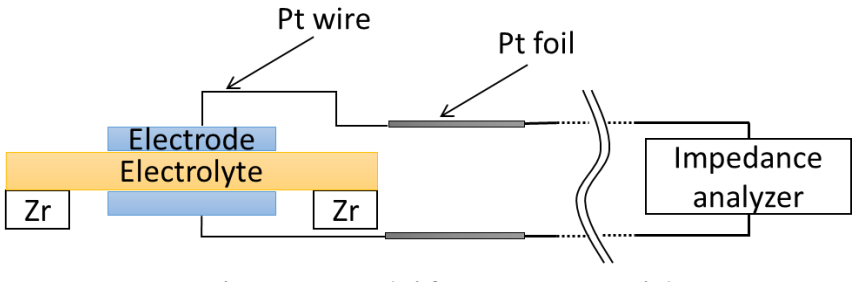

Figure 6-7 Ag electrode attached to the top and bottom of the disk-shaped SZY91. This figure shows the two-dimensional view seen from the lateral direction.

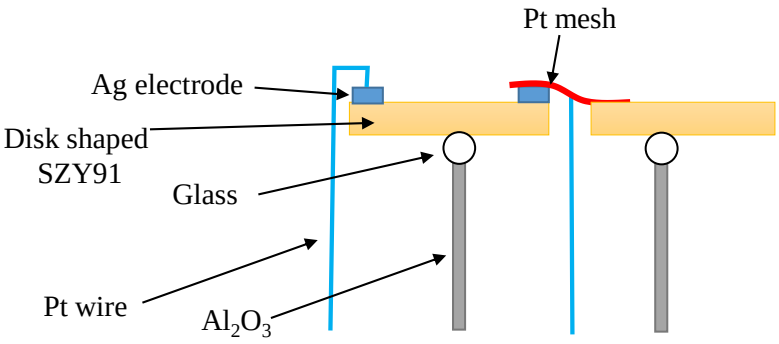

Figure 6-8 The position of Ag electrodes on the same side of disk-shaped SZY 91. This figure also shows two-dimensional view seen from the lateral direction. There is a hole in the center of the disk, and impedance measurement is possible via a platinum mesh.

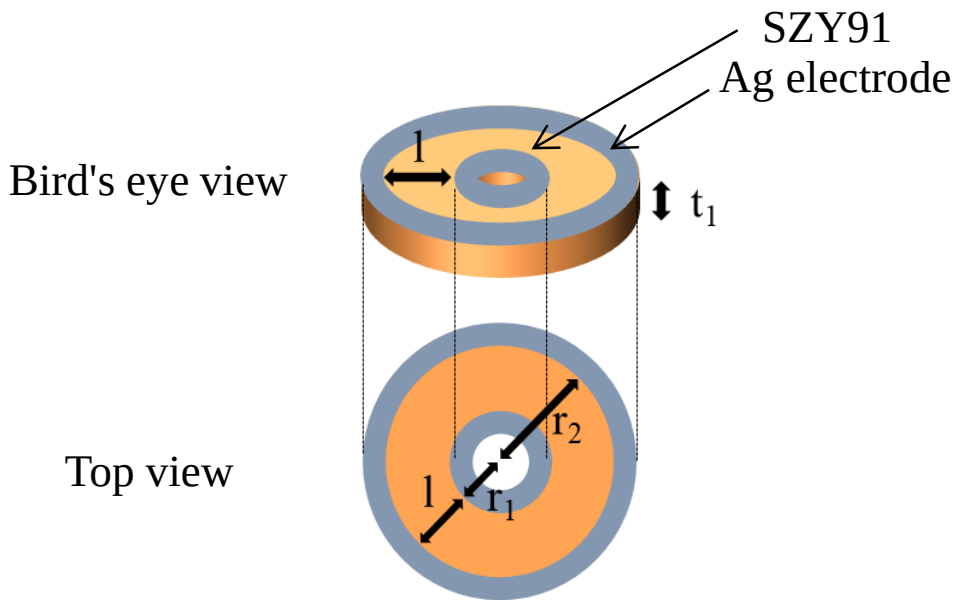

Figure 6-9 Position of parameters for equation. This schimatic model shows Ag electode and disk-shaped SZY91 for Figure.

6-2-4 Electromotive force measurement

Although four probe-techniques can evaluate electronic conduction on the surface of specimen, it cannot evaluate inside ionic conduction. By contrast, concentration cell can provide electromotive force (EMF) as proton conduction undergoes in the inside of the specimen. The reason why the concentration cell provides EMF is described as below. As the reaction is equilibrium on the both side of electrode as shown in Figure6, the difference between the chemical potentials of mono atomic hydrogen species is described as shown in equation (6-5)

$$\mu_{H_2}\ (\mathrm{I}) - \mu_{H_2}\ (\mathrm{II}) = -nFE \qquad (6\text{-}5)$$

Where $\mu_H(\mathrm{II})$, $\mu_H(\mathrm{I})$, n, F, and E indicate chemical potential of molecular hydrogen in

gas room(II), chemical potential of atomic hydrogen in gas room(I), the number of electron, the Faraday constant, and EMF, respectively. Since two electron reaction occurs in this case, we can obtain n as 2. Each chemical potential are described as shown in (6-6) and (6-7). Those potentials are substituted for equation (6-3), and we can obtain equation (6-8)

$$\mu_{H_2}\ (\mathrm{I}) = \mu^0_{H_2} + RT \ln P_{H_2}(\mathrm{I}) \tag{6-6}$$

$$\mu_{H_2}\ (\mathrm{II}) = \mu^0_{H_2} + RT \ln P_{H_2}(\mathrm{II}) \tag{6-7}$$

$$E = \frac{RT}{2F} \ln \frac{P_{H_2}(\mathrm{I})}{P_{H_2}(\mathrm{II})} \tag{6-8}$$

where P_{H2}(I) and P_{H2}(II) are hydrogen partial pressures at the gas compartments (I) and (II), respectively. Consequently, if both electrode reactions due to hydrogen are equilibrium state and both partial pressure of hydrogen are known, observed EMF becomes the proof of what proton conduction occurs inside of proton conductor. EMF with equation (6-8) is theoretical EMF as proton transport number is 100%.

As shown in Figure 6-10, the hydrogen concentration cell was established, and EMF and conductivity were measured. In this case, the conductivity was measured by 2-probe technique. The measurements were performed for a Pt|SZY91|Pt cell. Figure 6-11 indicates the temperature change of concentration cell. First, in order to seal the places which are zirconia tube and SZY91, the cell was heated while dry Ar gas was introduced into both of the electrode compartments. At that time, the cell was heated from room temperature to 900℃ at a rate of 5℃/min.. After the cell reached at 900℃, the gas was changed from dry Ar gas to dry 100%H_2 gas, and the temperature was held for 8h 40min.. After this treatment, the cell was cooled to 300℃ from 900℃, and electrical conductivity was attempted to be measured every 100℃ by 2-probe technique. At that time, the ratio of temperature change was 5℃/min. from 900℃ to 600℃. In addition, it was 2℃/min.

from 600℃ to 300℃. After the cell reached at 300℃, it was heated again to 400℃ at ratio of 2℃/min.. The reason why the cell was heated again was described as below. As mentioned before, measurement of EMF requires proton with uniform density in the electrolyte. Since it seemed that the equilibrium temperature of a reaction which produced unknown conductivity was at around 400℃, we expected that the treatment whom the cell was heated again provided equilibrium state of unknown reaction in the cell. The conductivity and EMF were attempted to be measured every 100℃ from 400℃ to room temperature by 2-probe technique and with hydrogen concentration cell, respectively. As EMF was attempted to be measured, the dry 100%H_2 on the lower side of SZY91 was changed to dry mixed gas with 99%Ar and 1%H_2(dry 1%H_2). Furthermore, at that time, the dry 100%H_2 on the upper side of SZY91 was also changed to dry 1%H_2.

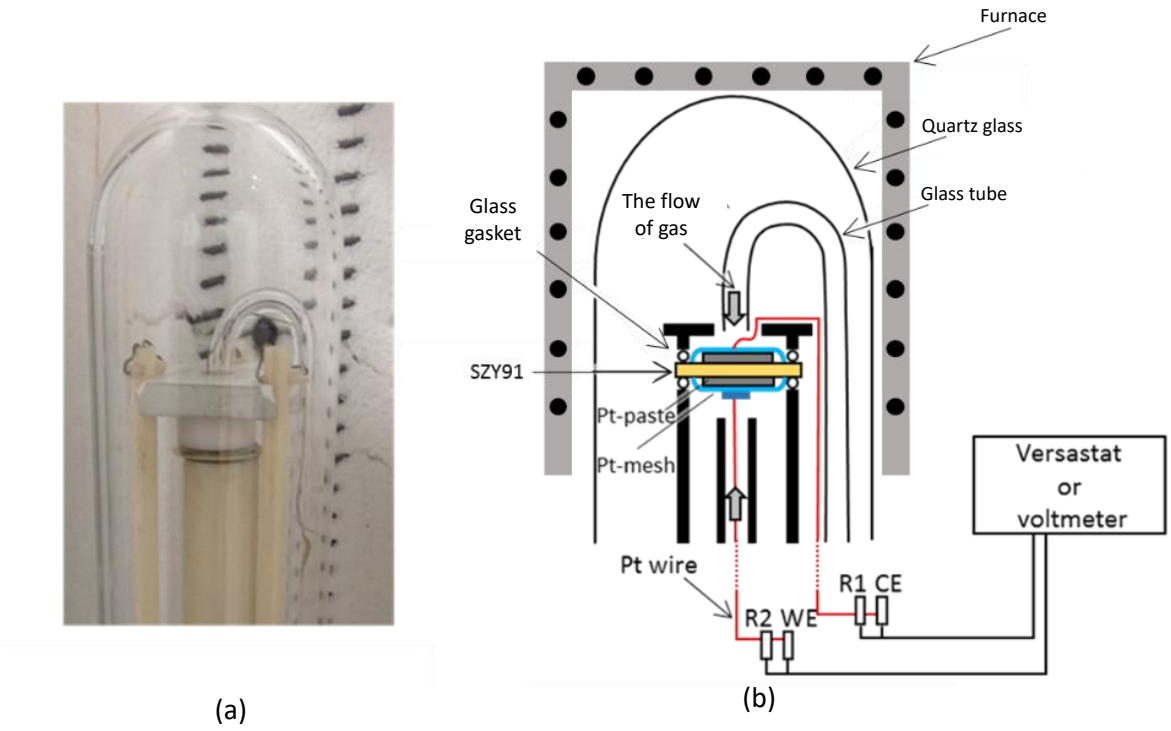

Figure 6-10 Actual picture(a) and illustration(b) of concentration cell

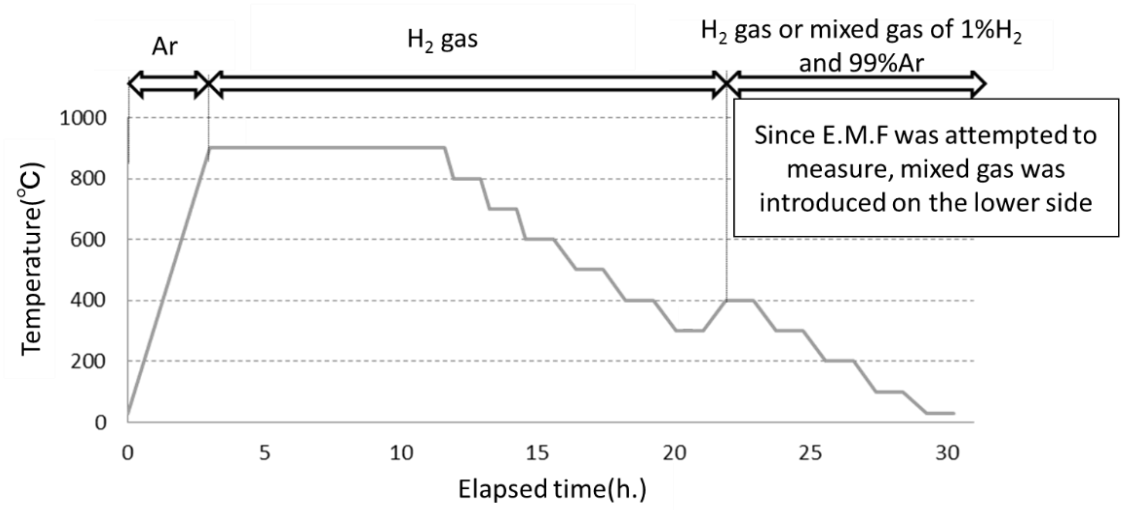

Figure 6-11 Temperature change as function of time for gas concentration cell with SZY91 in dry H_2

6-3 Results

6-3-1 Prepared samples

Figure 6-12 shows pictures of disk-shaped and bar-shaped SZY91, respectively. The relative density of both samples was over 95 % and X-ray diffraction patter as seen in Figure 6-13 shows there is no secondary phase in the samples.

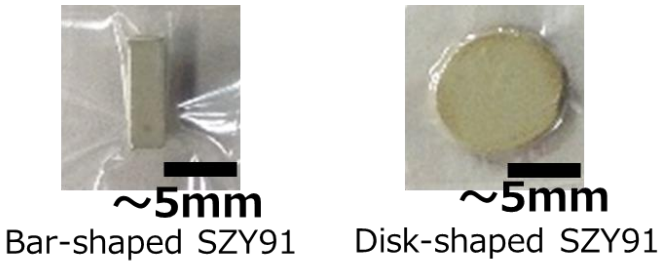

Figure 6-12 Pictures of SZY91 produced by sold state reaction method

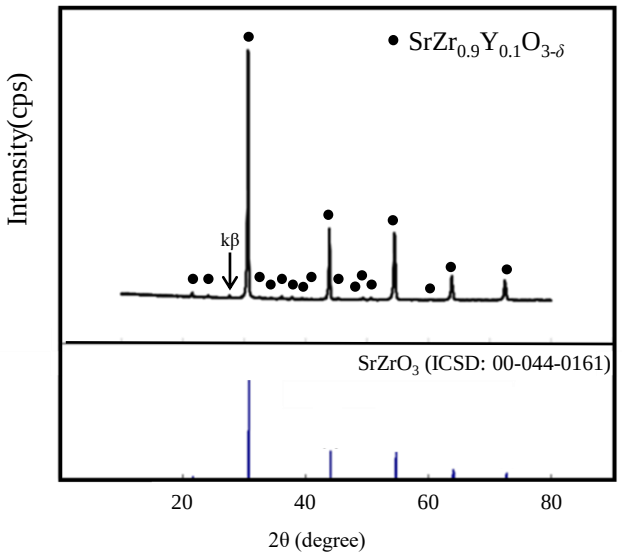

Figure 6-13 X-ray diffaction pattern of sintered SZY91

6-3-2 Electrical conductivity measurement

6-3-2-1 Silver vs. platinum electrode

Figure 6-14 shows the result of conductivity measurement for Ag electrode or Pt electrode of SZY91 in dry hydrogen. As clearly shown in both figures, as the temperature was lowered, the SZY91 using the Ag electrode had a higher electric conductivity in the cooling process. The reason why SZY91 using platinum has low electric conductivity at the time of temperature lowering than when at elevated temperature can be explained as water was dehydrated and the proton concentration became lowered. However, in the case of using the Ag electrode, this anomalous electrical conductivity possessed by SZY91 cannot be explained by conventional proton conduction due to hydration.

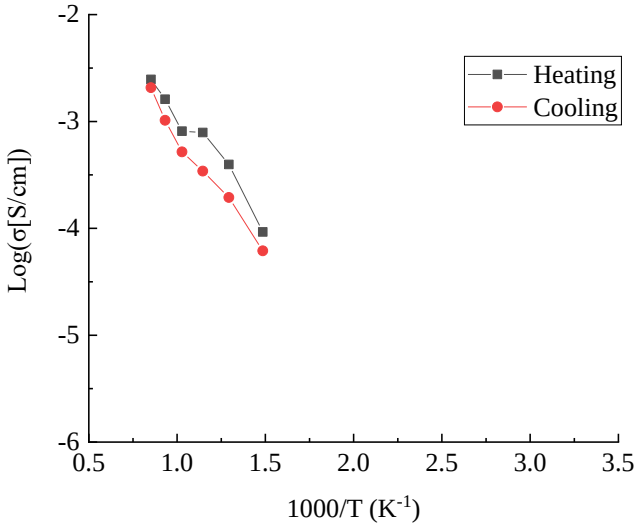

(a) Pt electrode

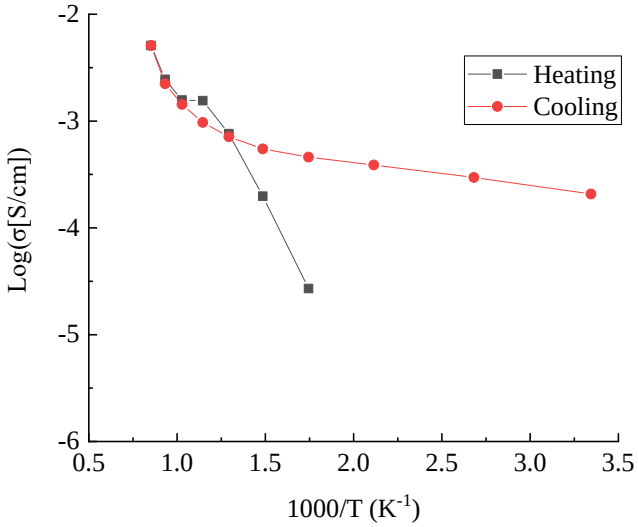

(b) Ag electrode

Figure 6-14 Electrode dependance conductivity of SZY91

6-3-2-2 Hydrogen gas pressure dependence

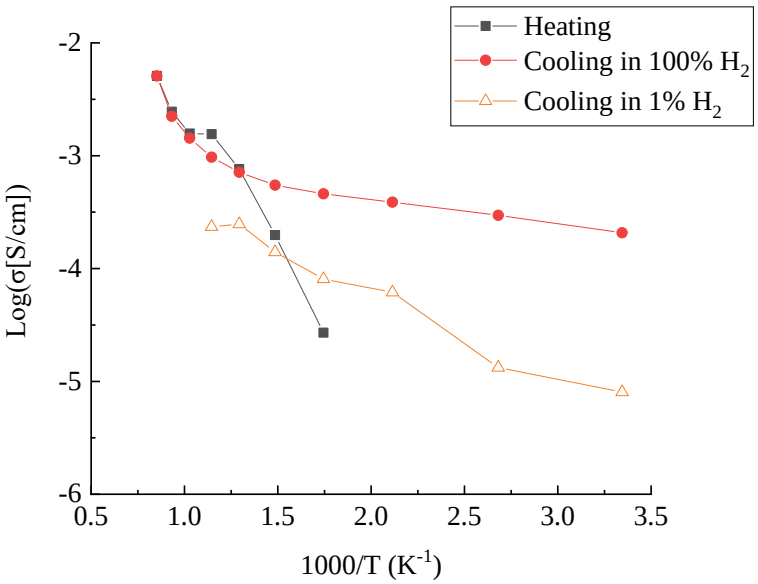

Figure 6-15 Hydrogen pressure dependance conductivity of SZY91. The conductivity obtained by a.c. 4 probe technique is same one in Figure 6-15

6-3-2-3 Bar-shaped SZY91 and position of electrode

The blue plot in the Figure 6-16 is the electric conductivity obtained by the a.c. two-probe technique for SZY91 with Ag electrode in 100% dry H_2. Even with consideration of the contact resistance between the electrode and SZY91, the electric conductivity obviously obtained by the a.c. two-probe technique tended to be smaller than the four-probe technique. In this figure, to make discussion easier, the temperature rise process and the electrical conductivity indicated by the red plot are the same data in the figure.

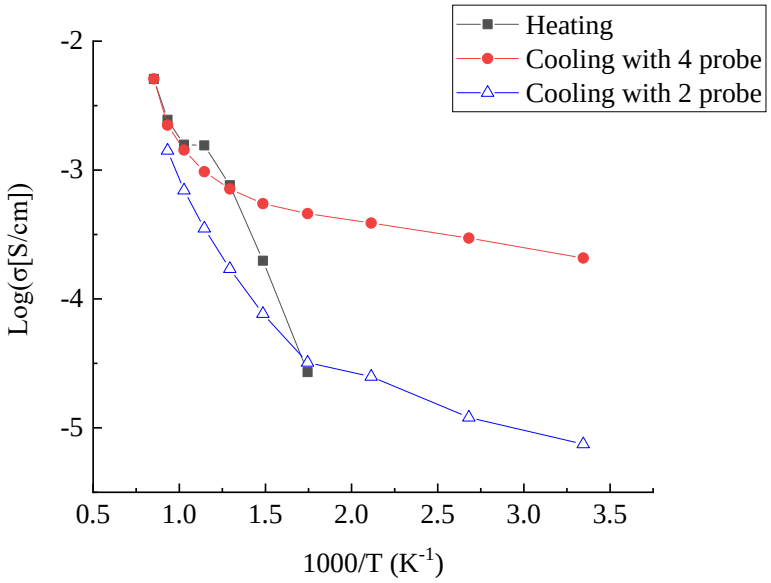

Figure 6-16 Conductivity of SZY91 with Ag electrode by a.c. 2 probe technique during cooling process. The conductivity obtained by a.c. 4 probe technique is same one in Figure 6-15.

6-3-2-4 Disk-shaped SZY91 and position of electrode

The electrical conductivity in the figure is the electrical conductivity in dry hydrogen obtained at the two types of electrode positions in the disk type SZY91. The electric conductivity obtained by attaching the electrode to the same surface on the disk indicated by the outline plot was obviously larger than the electric conductivity obtained by attaching the electrodes to both sides of the disk indicated by the other plot.

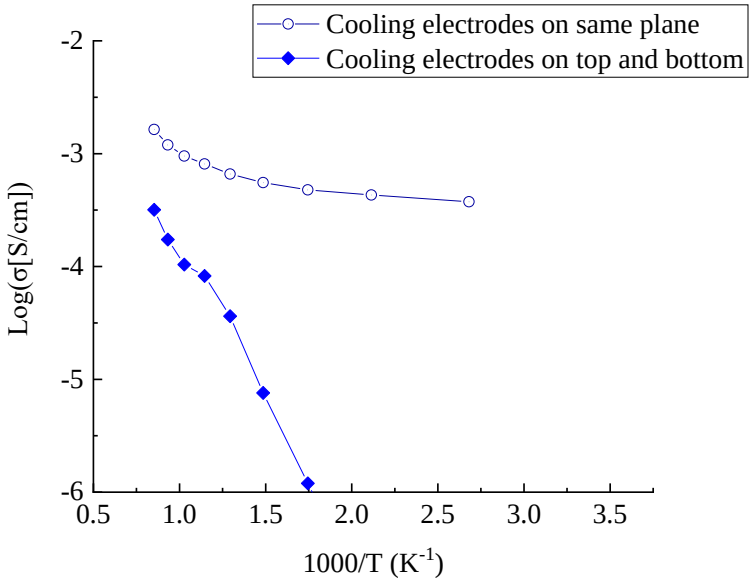

Figure 6-17 Conductivity of disk-shaped SZY91 with Ag electrode depending on the posiiton by a.c. 2 probe technique during cooling process.

6-3-4 Electromotive force measurement

Electromotive force (EMF) was measured with concentration cell using SZY91 attached Platinum electrode. As the cell served the concentration, dry 100%H_2 gas was introduced on the upper side of SZY91, and dry 1%H_2 on the lower side of it. The results are shown in Figure16. All EMF were observed on the same direction from the base line. These indicate that ion conduction occurred in SZY91 below 400℃. Since the atmospheric gas was dry hydrogen and argon gas, a conductive species could be proton as shown in Figure 6-18. Furthermore, as shown in Table 6-1, the transport number tended to decrease with decreasing in temperature.

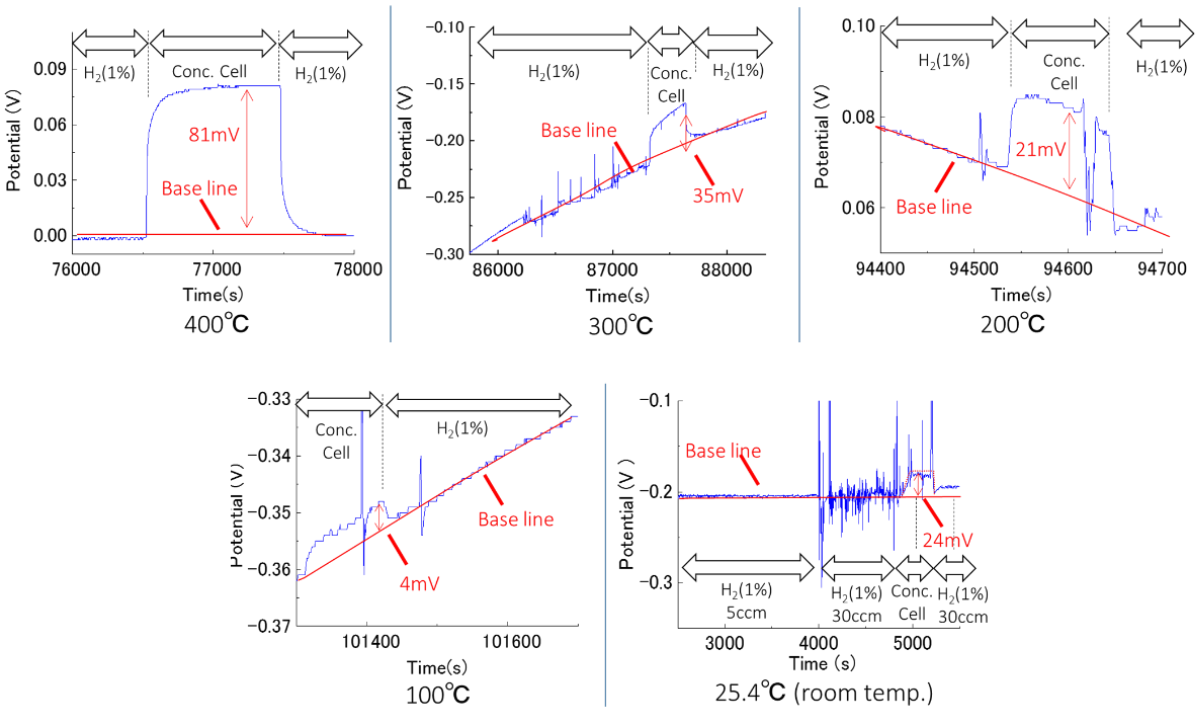

Figure 6-18 EMF measurement for SZY91 with Pt electrode in dry 100%H_2 gas

Table 6-1 Transport number of respective temperature

Temperature (℃)	Experiment (mV)	Theoritical (mV)	Transport number
400	81	133	0.61
300	35	114	0.31
200	21	94	0.22
100	4	74	0.05

6-4 Discussion

6-4-1 Possibility of surface conduction

The electric conductivity of SZY91 in dry H_2 appeared in this study is speculated that it is not bulk conduction but surface conduction. As shown in the figure, Ag electrode put on both sides of the disk-shaped SZY91 showed clearly lower conductivity than on the same side of the disk. This suggests that a conduction layer causing this anomalous electric conductivity formed the novel surface layer. As a future plan, this study also considers measuring seebeck coefficient to identify this unknown conduction species. If the species have positive charge, the seebeck coefficient becomes positive, and if they have negative charge, it becomes negative. The measurement technique to investigate seebeck coefficient for this research should be useful to narrow down the number of conduction species.

6-4-2 Reduction reaction and possible conduction species

The most important thing in this study is clarifying the reason why electric conduction changed after the heating process. Basically, it seems that reduction reaction undergoes after proton conductor of metal oxides is exposed to dry hydrogen gas and high temperature as shown in equation (6-9).

$$\frac{1}{2}\,H_2 + O_O^{\times} = OH_O^{\bullet} + e' \qquad (6\text{-}9)$$

As this reaction undergoes, the color of proton conductor should be darker. Since electron occupies the bottom of conduction band and does not fulfill entire there, electron in there will be easy to be excited by energy of visible light. Consequently, it seems that the proton conductor will occur absorption. However, the color of SZY91 was changed to be brighter as shown in Figure 6-19. This result is inconsistent with above theory.

EMF was observed from concentration cell after similar process of the conductivity measurement although the conductivity was not observed from SZY91 in concentration cell. In fact, the resistance used with electrical circuit tester of SZY91 after measurement with 4 probe technique in section 3.2.2 increased rapidly. This phenomenon could indicate ion conduction. Since there was nothing but H_2 gas during the experiment, it seemed that proton conduction occurred on the surface of SZY91.

Based on the above observations, we may conclude that proton conduction occurred on the only surface of SZY91 after exposed to dry H_2. Therefore, this conduction might be useful for thin film. The defect equilibrium equation could be suggested as equation (6-10) and equation (6-11).

$$V_{\mathrm{O}}^{\bullet\bullet} + \mathrm{H}_2 \leftrightarrows \mathrm{H}_{\mathrm{O}}^{/} + \mathrm{H}_i^{\bullet} \tag{6-10}$$

$$V_{\mathrm{O}}^{\bullet\bullet} + \frac{1}{2}\,\mathrm{O}_2 \leftrightarrows \mathrm{H}_{\mathrm{O}}^{/} + \mathrm{h}^{\bullet} \tag{6-11}$$

Where $V_{\mathrm{O}}^{\bullet\bullet}$ $\mathrm{H}_{\mathrm{O}}^{/}$, $\mathrm{H}_i^{\bullet}$, $\mathrm{h}^{\bullet}$ are oxygen vacancy, hydride ion trapped to oxygen vacancy, proton, hole, respectively. Therefore, it might occur mixed conduction as shown in Eq,.8 and Eq.9 on the surface of SZY91.

In order to clarify above hypothesis, following experiments may be effective. It is to evaluate the state of conduction band of SZY91 whose conductivity changed by ultraviolet photoelectron spectroscopy (UPS). This experiment could provide if reduction reaction occurred to SZY91 with dry H_2. In addition, in order to evaluate the location of proton in SZY91, elastic neutron scattering may be effective. With this methodology, the density of proton could be compared with before and after experiment in section 3.2.2.

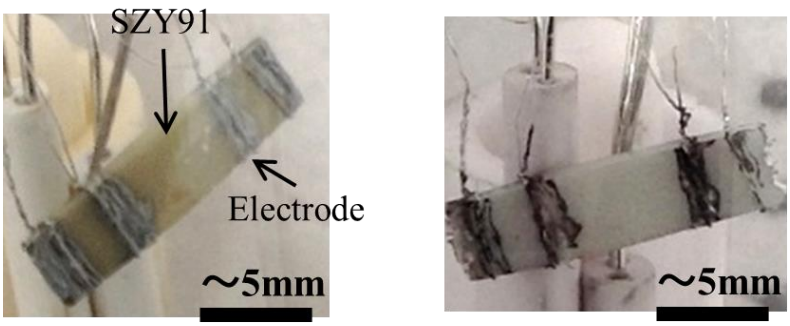

Figure 6-19 Comparison with the surface of SZY91

before and after exposed to dry H_2 gas

6-4-3 Analysis of electrode by X-ray diffraction pattern

X-ray structure analysis of SZY91 with high electric conductivity in dry H_2 was carried out together with the electrode. As seen in Figure 6-20, slight peak was observed at around 10 °C to 30 °C. Although it is not clear what this peak is derived from, it is impossible to expect such a peak in SZY91 having a perovskite structure, so we investigated the possibility of deriving from electrodes containing hydrocarbons. As shown in Figure 6-21, when a plurality of electrode samples were heated and cooled at room temperature to 800 ° C at 1% in dry hydrogen, no particular change was observed in the peak. Therefore, the influence of the electrode itself is hard to think. In this regard further investigation is necessary. In addition, in this paper, we present one possibility for the specific electric conductivity mentioned in dry hydrogen. It is a mechanism that hydrogen is supplied to silver from silver used for silver paste, becomes silver hydride, and its hydrogen is introduced into oxygen vacancies. First, decanol as shown by the structural formula in

the figure is used for the silver paste being used this time. First, decanol supplies hydrogen to silver as shown in the formula. Then, as shown in the formula, oxygen vacancies take in hydrogen from silver as hydride. It is already known that hydride can exist in the oxygen vacancy of perovskite, and a paper discussing whether the acid point can take in hydrogen from silver as described above has already been reported. This paper discusses that hydrogen can be sufficiently stored if silver nanoparticles are below 1 nm, and it also discusses that ZrO_2 can incorporate hydrogen. Although the conduction mechanism shown in this section is not shown by anyone, it is listed as one possibility to explain this phenomenon.

XRD pattern of Ag electrode was measured before and after heating process. Figure 6-21 shows the Ag-electrode before and after heating process, and Figure 6-22 shows the XRD pattern of these samples, and it was difficult to discuss change of crystal structure. Then, Ag electrode itself is not affected by dry H_2 from the viewpoint of XRD analysis.

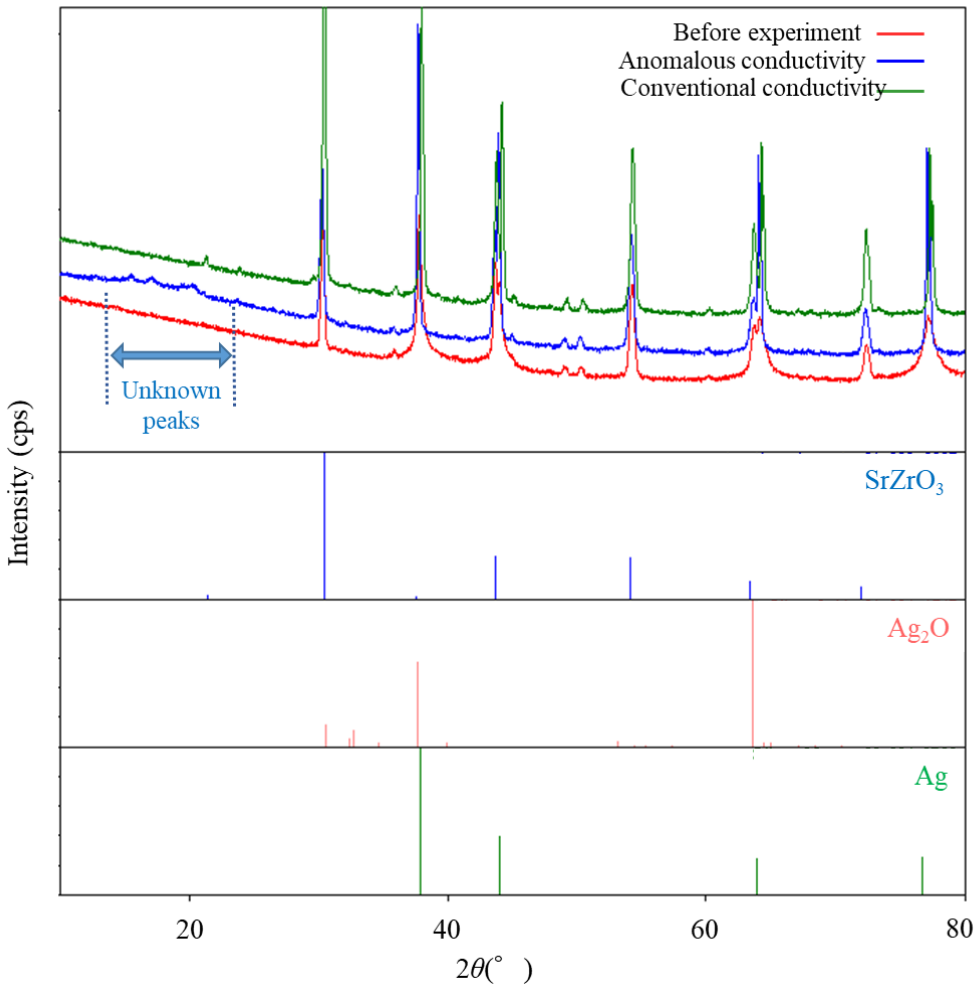

Figure 6-20 The XRD result of Ag paste with several conditions.

ICSD of $SrZrO_3$: 01-089-9005, Ag_2O : 01-084-1547, Ag : 00-004-0783

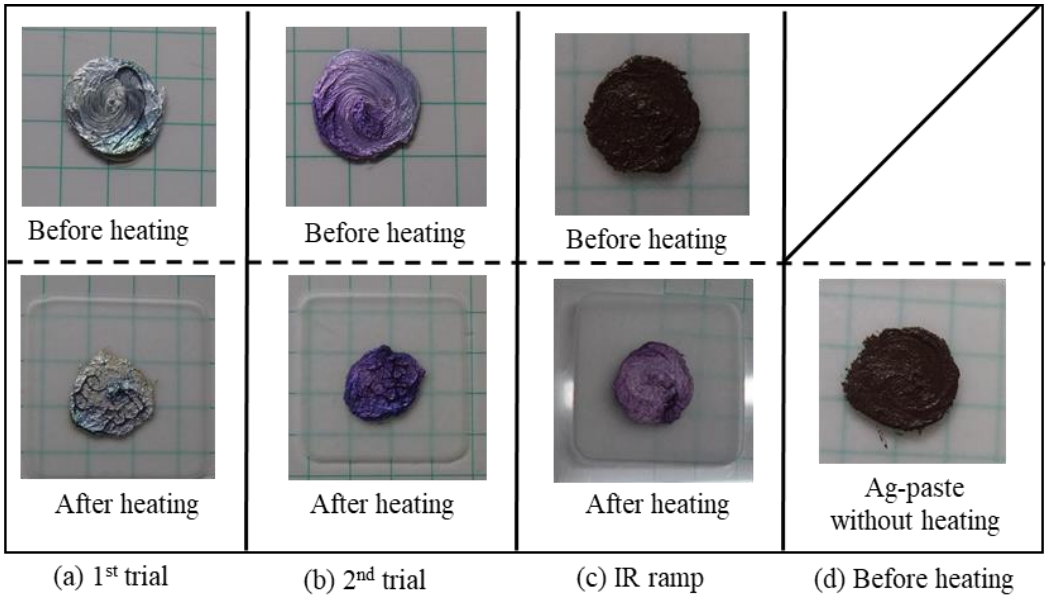

Figure 6-21 Look of Ag electrode before and after heat process

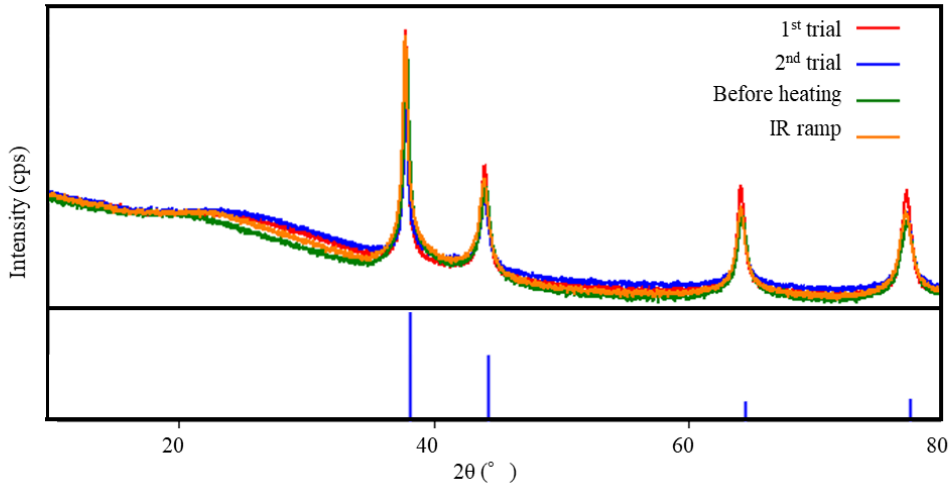

Figure 6-22 XRD pattern of Ag electrode before and after heat process

6-5. Conclusion

It has been experimentally observed that $SrZr_{0.9}Y_{0.1}O_{3-\delta}$ (SZY91) treated in dry hydrogen at 900℃ exhibits low temperature dependence of electrical conductivity that corresponds to an activation energy lower than 0.1 eV. This is unusually low in

comparison with ordinary activation energies of common proton conduction in metal oxides, 0.3-0.7 eV. As a result of such a low temperature dependence, SZY91 thus treated in dry hydrogen shows relatively high electrical conductivity at low temperatures, e.g. $10^{-3.7}$ S cm^{-1} at 26℃. Such a low activation energy and the resulting high conductivity at low temperature is normally attributable to electronic conductivity, however, development of EMFs observed for hydrogen concentration cells suggests that the conductivity is originated from ionic conduction. The above two phenomena, little-temperature-dependent conductivity and the development of EMF in response to a different gas concentrations, are not well reproducible, i.e., the key factor governing the occurrence of the phenomena is not elucidated yet. But, it is conclusive the above experimental result suggest that the heat treatment in dry hydrogen possible generate a high ionic conductivity in SZY91.

Reference

(6-1) Kreuer, K. D. Proton-Conducting Oxides. *Annu. Rev. Mater. Res.* **33,** 333–359 (2003).

(6-2) Iwahara, H., Esaka, T., Uchida, H. & Maeda, N. Proton conduction in sintered oxides and its application to steam electrolysis for hydrogen production. *Solid State Ionics* **3–4,** 359–363 (1981).

(6-3) Tao, Z. *et al.* A review of advanced proton-conducting materials for hydrogen separation. *Prog. Mater. Sci.* **74,** 1–50 (2015).

(6-4) Bi, L., Fabbri, E. & Traversa, E. Solid oxide fuel cells with proton-conducting La0.99Ca0.01NbO4 electrolyte. *Electrochim. Acta* **260,** 748–754 (2018).

(6-5) Lei, L., Keels, J. M., Tao, Z., Zhang, J. & Chen, F. Thermodynamic and

experimental assessment of proton conducting solid oxide fuel cells with internal methane steam reforming. *Appl. Energy* **224,** 280–288 (2018).

(6-6) Bi, L., Da'as, E. H. & Shafi, S. P. Proton-conducting solid oxide fuel cell (SOFC) with Y-doped BaZrO3electrolyte. *Electrochem. commun.* **80,** 20–23 (2017).

(6-7) Perovskite, H. H. *et al.* Panasonic Technical Journal Vol. 63 No. 1 May 2017 -. **63,** (2017).

(6-8) Fabbri, E., Bi, L., Pergolesi, D. & Traversa, E. Towards the next generation of solid oxide fuel cells operating below 600 ℃ with chemically stable proton-conducting electrolytes. *Adv. Mater.* **24,** 195–208 (2012).

(6-9) Matsumoto, H., Nomura, I., Okada, S. & Ishihara, T. Intermediate-temperature solid oxide fuel cells using perovskite-type oxide based on barium cerate. *Solid State Ionics* **179,** 1486–1489 (2008).

(6-10) Sun, W., Yan, L., Shi, Z., Zhu, Z. & Liu, W. Fabrication and performance of a proton-conducting solid oxide fuel cell based on a thin BaZr0.8Y0.2O3-δ electrolyte membrane. *J. Power Sources* **195,** 4727–4730 (2010).

(6-11) Song, S. & Placido, F. The influence of phase probability distributions on impedance spectroscopy. *J. Stat. Mech. Theory Exp.* **2004,** P10018 (2004).

(6-12) Hibino, T., Mizutani, K., Yajima, T. & Iwahara, H. Evaluation of proton conductivity in SrCeO3 , BaCeO3 , CaZrO3 and SrZrO3 by temperature programmed desorption method. **57,** 303–306 (1992).

(6-13) Dygas, J. R., Fafilek, G. & Breiter, M. W. Study of grain boundary polarization by two-probe and four-probe impedance spectroscopy. *Solid State Ionics* **119,** 115–125 (1999).

Summary

Firstly, this thesis introduces that solid state ionics is multidisciplinary scientific fields regarding proton conducting oxides through Chapter 1. To understand the properties, it is necessary to investigate them from the viewpoints of atomic scale. Recent advance of computational science provides us outstanding results for material science. Because of the attractive way, in Chapter 2, the computational background for this thesis used from Chapter 3 to Chapter 5 is summarized.

In Chapter 3, it is considered that chemical expansion of proton conducting oxides cause mechanical failure of electrolyte in solid oxide fuel cells or solid oxide electrolysis cell. Because Ce and Zr are famous elements for B-site of proton conducting oxides, is it necessary to understand the effect of them against chemical expansion. Then, this chapter investigated that the effect of Ce and Zr in yttrium-doped strontium zirconate and cerate on chemical expansion by hydration. HT-XRD and TGA indicated that the cerate has a chemical expansion coefficient approximately 4 times larger than that of the zirconate. DFT calculations suggested that the chemical expansion coefficient is dependent on the configuration of the Y atoms: The cerate exhibited lower chemical expansion than the zirconate when the Y atoms were in close proximity and higher chemical expansion when the Y atoms were further apart. Thus, the experimental observation of the larger degree of chemical expansion in the cerate than in the zirconate can be attributed to the mixed presence of both configurations of Y atoms. DFT calculations suggested that the size of oxide ion vacancies differs based on the Y atom configuration: when the Y atoms were in close proximity, the cerate exhibited larger oxide ion vacancies than the zirconate, which

resulted in the lesser degree of chemical expansion in the former. The results indicated a correlation between the chemical expansion and the size of oxide ion vacancies to be hydrated, and that the size of the oxide ion vacancies is correlated with the configuration of Y dopant atoms. The elastic character is another factor influencing the different chemical expansion behavior of the cerate and zirconate; the former has a lower bulk elastic modulus which led to a higher degree of chemical expansion.

Chapter 4, focusing on bulk SZY and YSZ, investigated covalent bonding with Zr - O by DFT. As a result, the covalent bonding property of SZY is larger than the covalent bonding property of YSZ, which indicates that SZY tends to trap oxygen in water. Conversely, since YSZ can not trap water due to weakness of covalent bonding, it can be said that protons can not be introduced into the crystal lattice. In this research, we developed the previous research and explains the characteristics of bulk YSZ and SZY for hydration mechanism.

In Chapter 5, the tendency of charge transfer from the proton conducting oxides to Pt was obtained at the thin film interface between them. As a results, DFT shows proton conducting oxides mostly provide electrons to Pt. This was the opposite tendency against this study's hypothesis. However, combination of *B*O-terminated surface of proton conducting oxides with Pt nano particles could show the result that Pt provides electrons to them.

In Chapter 6, it has been experimentally observed that $SrZr_{0.9}Y_{0.1}O_{3-\delta}$ (SZY91) treated in dry hydrogen in high temperature exhibits low temperature dependence of electrical conductivity that corresponds to an activation energy lower than 0.1 eV. The different conductivity behavior depending on position of Ag electrode with bar-shaped or disk-shaped SZY91 suggests that the anomalous conductivity mainly occurs on the surface.

List of publication

Papers

[1]**Takaya Fujisaki**, Aleksandar Tsekov Staykov, Kwati Leonard, Yuhang Jing, Narayana R Aluru,Hiroshige Matsumoto, “Understanding effect of Ce and Zr on chemical expansion in yttrium doped strontium cerate and zirconate by high temperature X-ray analysis and density functional theory” accepted by Solid State Ionics

[2]**Takaya Fujisaki**, “Evaluation of Green Paradox: Case Study of Japan” accepted by Evergreen (Vol. 05, Issue 04, pp.26-31, December 2018)

Awards

[1] Subutsu-kai award, Ritsumeikan University March 22, 2015

[2] Poster Award, Interim Report for Master Students of Interdisciplinary Graduate School of Engineering Sciences in Kyushu University, April 6, 2015

[3] Poster Award, Presentation of Graduation Theses for Master Students of Interdisciplinary Graduate School of Engineering Sciences in Kyushu University, February 18, 2016

[4] Poster Award, The 5th CSJ Chemical Festa 2015, November 12, 2015

[5] Bronze Award, Kyushu University Energy Week 2017 January 31, 2017

[6] Presidential Award, Kyushu University Energy Week 2017 January 31, 2017

Presentations

(Oral)

[1]Chihiro Kaito, Yoshio Saito, Tetsuya Miyashita, ○**Takaya Fujisaki**

「Production of few nanometers metal and ultra -fine metal particles」

『Physical Society of Japan Autumn Meeting 2011』, 21aRC-3, Toyama pref., September 2011

[2] Chihiro Kaito, Yoshio Saito, Chiyoe Koike, Tetsuya Miyashita, ○**Takaya Fujisaki**

「Production of Enstatite and Crystallization Temperature」

『Physical Society of Japan Spring Meeting 2012』, 25aCK-6, Hyogo pref., March 2012

[3] ○**Takaya Fujisaki**, Alexander Staykov, Yuhang Jing, Narayan Aluru, Hiroshige Matsumoto

「Evaluation of proton conducting oxides by first principle calculation」『The 85th Electrical chemical society of Japan』Tokyo, March 2018

[4] ○**Takaya Fujisaki**, Alexander Staykov, Yuhang Jing, Narayan Aluru, Hiroshige Matsumoto

「Understanding the Effect of Ce and Zr on Chemical Expansion in Y-doped Strontium Cerate and Zirconate by Density Functional Theory and High Temperature X-Ray Analysis」『130th Institute Interest Seminar Series』, Fukuoka, July 2018

(Poster)

[1] ○Chihiro Kaito, Yoshio Saito, Chiyoe Koike, Tetsuya Miyashita, **Takaya Fujisaki**

「Laboratory analogy of amorphous enstatite fine grain and crystallization」

『The 5th meeting on Cosmic Dust』Center for Planetary Science, Hyogo pref., August 2012

[2] ○Chihiro Kaito, Yoshio Saito, Chiyoe Koike, **Takaya Fujisaki**

「Mg-Fe Alloy Produced by Gas Evaporation Technique」

『Physical Society of Japan Autumn Meeting 2012』20pPSA-59, Kanagawa pref., September 2012

[3] ○Chihiro Kaito, **Takaya Fujisaki**,Yoshio Saito, Chiyoe Koike

「Crystallization of amorphous $MgSiO_3$」

『The 73rd Japan Society of Applied Physics Autumn Meeting 2012』13p-PB10, Ehime pre., September 2012

[4] ○Chihiro Kaito, Yoshio Saito, Chiyoe Koike, **Takaya Fujisaki**

「Crystal Growth of Ultra-Fine Particles Fe_2SiO_4 and $(Mg_xFe_{1-x})_2SiO_4$」

『 The 30th Grain Formation Workshop」P1, Hyogo pre, November 2012

[5] ○Chihiro Kaito, Yoshio Saito, Chiyoe Koike, **Takaya Fujisaki**

「Production of Vanadium Ultra-fine Particlesby Gas Evaporation Technique and the Oxidation at Room Temperature」

『The 68th Physical Society of Japan annual Meeting』26pPSA-52, Hiroshima, March 2013

[6] ○**Takaya Fujisaki,** Kwati Leonard, Youngsung Lee, Yuji Zenitani, Hiroshige Matsumoto

「Novel Electrical Conduction Observed in Yttrium-Doped Strontium Zirconate in Dry Hydrogen」

『Prospects on Protonic Ceramic Cells』, France-Bordeaux, July 2015

[7] ○ **Takaya Fujisaki**, Kwati Leonard, Youngsung Lee, Yuji Zenitani, Hiroshige Matsumoto

「 Electrical Conduction Behavior of Yttrium-Doped Strontium Zirconate in Dry Hydrogen Gas」

『Rare Earths 2016』, Japan-Sapporo, June 2016

[8] ○ **Takaya Fujisaki**, Kwati Leonard, Youngsung Lee, Yuji Zenitani, Hiroshige Matsumoto

「 Electrical Conduction Behavior of Yttrium-Doped Strontium Zirconate in Dry

Hydrogen Gas」

『Solid State Ionics 18』, Norway-Oslo, September 2016

[9] ○**Takaya Fujisaki**, Yassuhiro Takamura, Alexander Staykov, Hiroshige Matsumoto

「Theoretical Study for the Effect of Pt Nanoparticles on Strontium Cerate and Zirconate」

『The 13th Solid State Ionics Seminar』 Miyazaki, September 2017

[10] ○ **Takaya Fujisaki**, Yassuhiro Takamura, Alexander Staykov, Hiroshige Matsumoto

「Theoretical Study for the Effect of Pt Nanoparticles on Strontium Cerate and Zirconate」

『Talk Shower in Kyushu 2017』 Oita pre. March 2017

[11] ○ **Takaya Fujisaki**, Yassuhiro Takamura, Alexander Staykov, Hiroshige Matsumoto

「Theoretical Study for the Effect of Pt Nanoparticles on Strontium Cerate and Zirconate」

『13th Solid state ionics seminar』 Miyazaki Japan. September 2017

[12] ○**Takaya Fujisaki**, Aleksandar Tsekov Staykov, Nicola Helen Perry, Yuhang Jing, Narayana R Aluru,Hiroshige Matsumoto「Understanding the Effect of Ce and Zr on Chemical Expansion in Yttrium doped Strontium Cerate and Zirconate by Density Functional Theory and High Temperature X-Ray Analysis」

『5th Solid-state Chemistry & Ionics Workshop』 Fukuoka Japan. September 2018

[13] ○**Takaya Fujisaki**, Aleksandar Tsekov Staykov, Nicola Helen Perry, Yuhang Jing, Narayana R Aluru,Hiroshige Matsumoto「Understanding the Effect of Ce and Zr on Chemical Expansion in Yttrium doped Strontium Cerate and Zirconate by Density Functional Theory and High Temperature X-Ray Analysis」

『4th International Exchange and Innovation Conference on Engineering & Sciences』 Fukuoka Japan. October 2018

Acknowledgement

The research in the present thesis has been carried out under the guidance of Professor Hiroshige Matsumoto for the period of 2014-2019 in the Hydrogen Production Process Laboratory, Electrochemical Energy Conversion Division, International Institute for Carbon-Neutral Energy Research, Kyushu University. In addition to him, I am grateful for cooperation of following faculty staffs in Kyushu University. Firstly, Professor Akira Harata in Department of Molecular and Material Sciences helped me a lot as a dean of the Interdisciplinary Graduate School of Engineering Sciences. I thank Professor Tatsumi Ishihara to support me as a head of JSPS-NSF Partnerships for International Research and Education (PIRE). Also, I appreciate Professor Akbay Taner for helping me obtain the technique of density functional theory. In addition, I express my sincere gratitude to Associate Professor Aleksandar Tsekov Staykov who gave me the chance to study on density functional theory, for his kind guidance, valuable suggestions and hearty encouragement through this work. In addition, I appreciate Associate Professor Masamichi Nishihara for giving me the way to use thermogravimetric analysis and kind advice to proceed my study. Furthermore,

Also, I thank following people in University of Illinois at Urbana-Champaign. Firstly Professor Narayana R. Aluru, Mechanical Science and Engineering kindly gave me the chance to stay his group for 3 months in my doctoral course. Assistant Professor Nicola Helen Perry kindly provided me to stay her laboratory for 3 months for study on chemical expansion and further advice after finishing 3 months' internship. Dr. Yuhang Jin also helped me a lot obtain the technique to proceed study on density function theory despite that I was beginner when I just took part in Professor Aluru's group.

I would like to express my gratitude to Professor Michihisa Koyama in National Institute for Materials Science for giving me the chance to have internship in his group for 3 months. Also, Associate Professor Takayoshi Ishimoto in Hiroshima University helped me proceed my study in the internship. Furthermore, I appreciate Dr. Rivera Rocabado David Samuel to help me understand the theory of density functional theory.

Furthermore, I would like to appreciate Dr. Yuji Zenitani in Panasonic corporation to give me the chance to have internship for 1 month. My thanks are also extended to all the members of Hydrogen Production Process Laboratory who have helped and made my research life so enjoyable; Dr. Kwati Leonard, Dr. Young Sung Lee, Dr. Vediyappan Veeramani, Mr. Mineo Matudaira, Ms. Mizuho To, Mr. Yasuhiro Takamura, Issei Okuzaki, Shoichi Furukawa, Munemitsu Nomura, Taito Okuma, Touma Kidera, Kouki Ikeda, kouhei Yoshimori, and all alumni of the laboratory. All students and professors who met at conferences discussed my research sincerely. All members of Ambitious Leader's Program and technical staffs supported my research. This research is also financially supported by "Advanced Graduate Program in Global Strategy for Green Asia" of the Ministry of Education, Culture, Sports, Science and Technology, Japan. Finally, I am particularly grateful to my family for their perpetual understandings and supports.

March 2019

Takaya Fujisaki

Appendix A

Review of Research and Development for Hydrogen Society

This appendix explains social background of "hydrogen society" combining hydrogen and renewable energy toward a sustainable society.

A-1. Introduction

Electricity is essential to our society, and we have consumed fossil fuels such as coal, natural gas, and petroleum to generate electricity. As shown in Figure A-1, in 2015, the amount of consumption of natural gas, coal/petroleum, and oil which was typical fossil fuels was approximately 82% in the total amount of world energy consumption [A-1]. The energy consumption has grown, and it is estimated to dramatically increase in the future as seen in Figure A-2. Especially, developing countries are estimated to increase rapidly [A-2]. In fact, it is already predicted how long we can continue mining fossil fuels. When continuing mining fossil fuels at the current pace, we cannot increase the amount of production at some point. Reserves-to-production (R/P) ratio is the result of examining how much more mining is possible at each year. Figure A-3 shows the graph of R/P ratio at respective years until 2015 [A-3].The R/P ratio of natural gas has generally continued to be flat, and that of coal has decreasing trend. In addition, that of oil decreased after 2012. In short, it is unlikely the R/P ratio will not drmatically increase in the future. Indeed, the natural gas could support the demand of our society near future, but the minible years will be limitied.

Sooner or later though fossil fuels will be exhausted, it will take at least in one hundred

years. However, what we have to consider seriously is not the depletion year, but production peak. The production peak refers to the year when fossil fuels procuded most. When the produciton peak comes, the amout of fossil fuels production after the peak will not increase. As long as our society currently relays on them, there is concern that some countries will scramble for the energy source each other after the peak, which leads to the destablizing factor in those society. In fact, Mohr *et al*. suggested that the production peak for primaly fossil fuels will come by 2025 [A-4]. Although innnovation of mining technology and policies of government could postpone the peak, we can not avoid the production peak in the future. After that, the amount of energy production will decrease gradually despite that large number of countries wishes to increase the energy consumption. Eventually, to satisfy the world energy demand which will continue to increase, we have to find alternative energy source. Otherwise, our society will experience disruption due to lack of energy supply.

To prevent the situation from being disruptive due to lack of energy supply, we have to find the alternative energy source. The energy source should have a low impact on the environment. Especially, the idea of global warming is widely accepted today and it is a threat we can not ignore[A-5]. Energy supply for our society should be provided with renewable energy such as wind power and solar power. Indeed, hydropower as a renewable energy could be increased to supply electricity in the future[A-6]. However, the amount of hydropower will not be able to cover the future energy demand in the world. Because most promising location for hydropower has already been used especially in developed countries, those countries will not be able to increase the energy supply with hydropower.

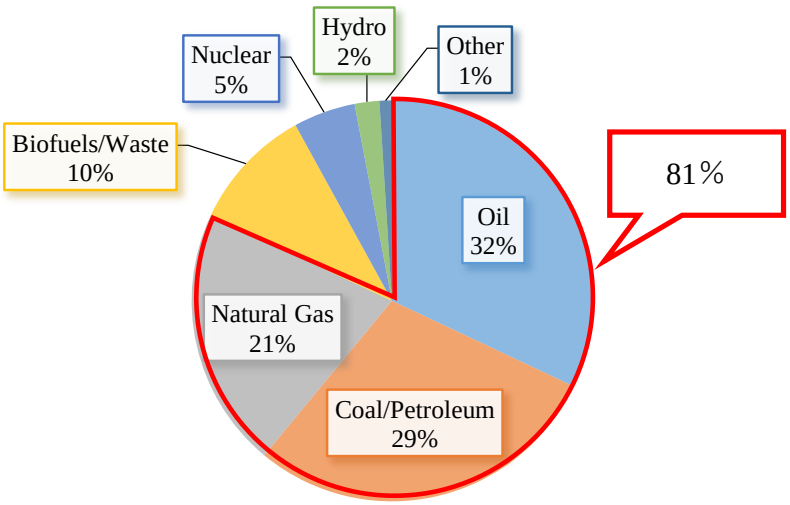

Figure A-1. World's fuel shares of total primary energy supply[A-1].

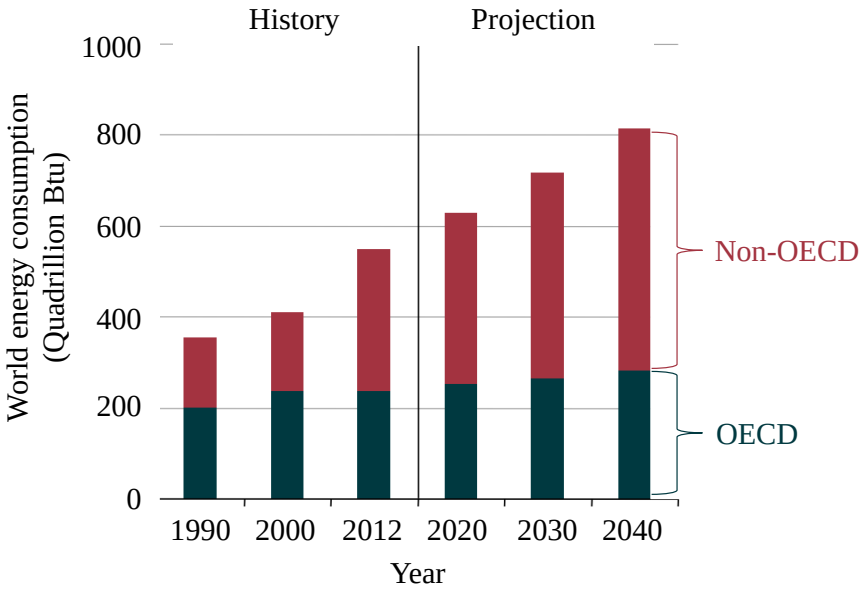

Figure A-2. World energy consumption from 1990 to 2040(Estimated),

(Btu: British thermal unit, OECD: Organization for Economic Co-operation and Development)[A-2]. Source: U.S. Energy Information Administration (May Oct 2016).

Permission to reproduce is obtained by U.S. Energy Information Administration.

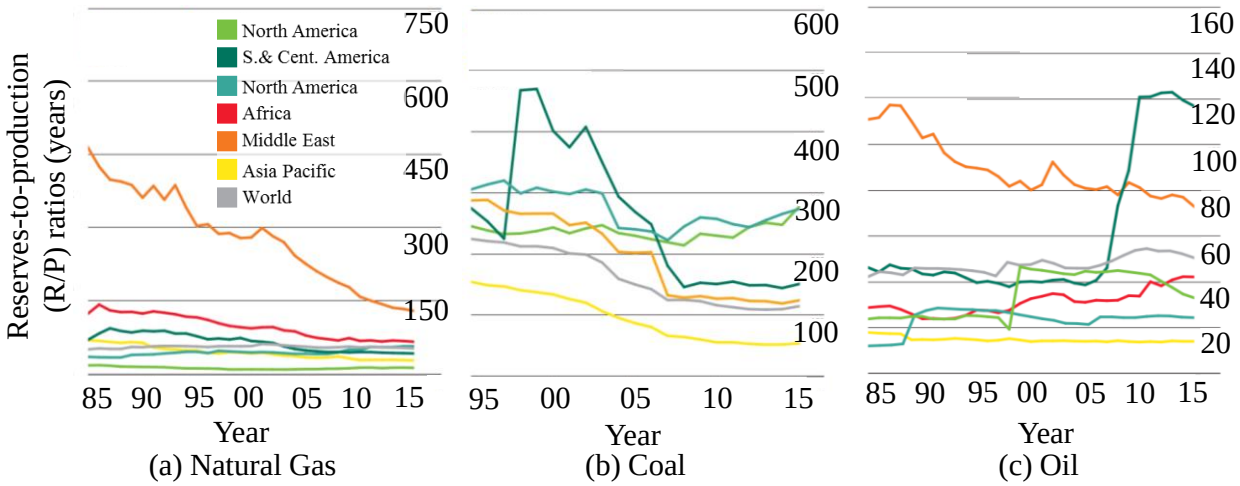

Figure A-3. R/P ratio of natural gas, coal, and oil[A-3].

Permission to reproduce is obtained by BP p.l.c

A-2 Renewable energy and hydrogen

Combination of solar, wind power and hydrogen is the promising way to provide energy because they can be combined as closed energy cycle with water and hydrogen (+ oxygen in air)[A-7]. As seen in Figure A-4, fuel cells are coupled with the electrolyzer and renewable energy conversion technologies (wind power and solar power) to provide electricity without pollution such as carbon dioxide emission. The most advanced point in this system is that fossil fuels are completely eliminated. The capability of producing electricity with renewable energy is not stable due to the climate condition. To provide

electricity stably, once hydrogen is stored with surplus energy from renewable energy, electricity will be provided stably. To realize above ideal system, in fact, there are many suggestions we have to overcome. For example, hydrogen itself has to be isolated or produced from various chemical composition (such as H_2O). It is because most hydrogen does not exist by itself. Then, it is important to make hydrogen from various chemical composition efficiently [A-8].

As mentioned previously, when the rest of fossil fuels starts to phase out after the production peak, the system of Figure A-4 can be expected to substitute for conventional energy supply with fossil fuels. Although energy conversion efficiency is not enough, the system begins to be used as demonstration to produce hydrogen by electrolyzing water[A-9,A-10]. To boost the system, the market of renewable energy, technologies, investment and policy frameworks have recently significantly developed. In fact, the amount of renewable energy source for global energy consumption in 2010 was 16.7% in total, which is strongly increasing year by year[A-11]. Still, we should reduce the installation cost of renewable energy, and expand the amount of hydrogen storage. The success of the system depends on the result of research and development. This review focuses on the current status for the system shown in Figure A-4 of the research and development. The system is largely separated into three parts. They are hydrogen production, hydrogen storage, and electrical generation with fuel cell, respectively.

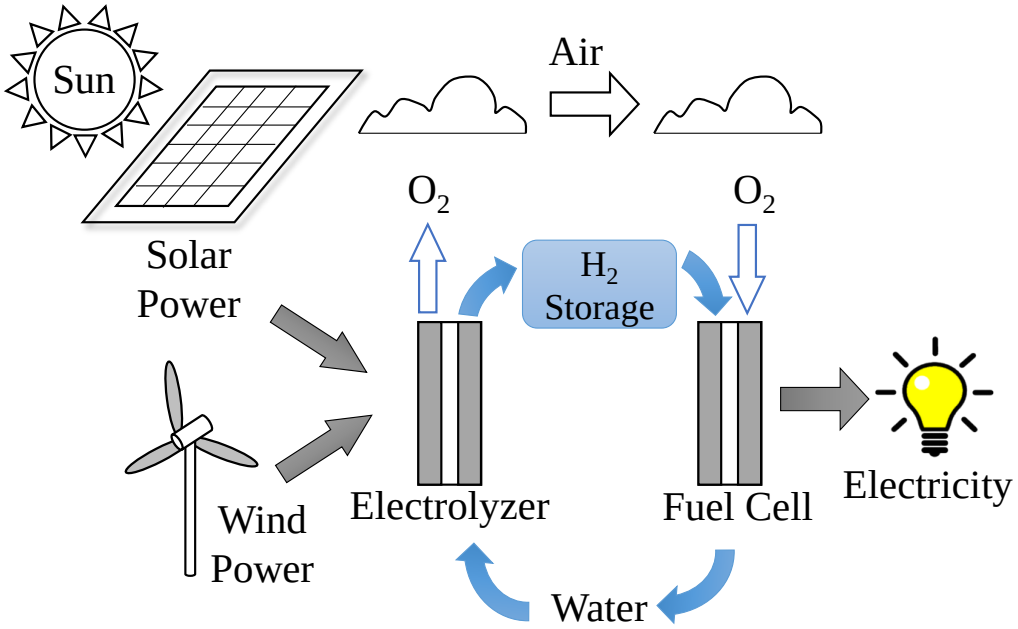

Figure A-4. Concept of hydrogen renewable energy system for power generation (This system is independent on consumption of fossil fuels)[A-12].

A-3 Hydrogen production

Firstly, this section explains the hydrogen production in Figure A-6. As previous section mentioned, to spread utilization of hydrogen, there are three steps which are hydrogen production, hydrogen storage, and hydrogen utilization. This section introduces the current status of research and development in terms of hydrogen production as below. Hydrogen production constitutes one of the biggest challenge to establish sustainable society with hydrogen [A- 13]. This society is called “hydrogen society” and it is ideal for the society to produce hydrogen with electrolysis [A-14,A-15]. However, the electrolysis does not have enough competitiveness in comparison with other hydrogen production methods due to the expensive cost. The cost by water electrolysis is not cheap, and then the cost by fossil fuel reforming is main stream because of cheap hydrogen

production cost. This section explains the current situation of research and development on fossil fuel reforming and electrolysis.

A-3-1 Fossil fuel reforming

To produce hydrogen with fossil fuels, there are typically three types of technologies for fossil fuel reforming. They are steam reforming, autothermal reforming, and partial oxidation, respectively. These advantages and disadvantages are listed in Table 2-1[A-16]. In addition to producing H_2, this production method emits CO and CO_2 during the production process. The steam reforming requires an external heat, but it does not demand oxygen to run this process. It has a lower operating temperature and higher H_2/CO ratio than partial oxidation and autothermal reforming [A-17]. The partial oxidation is a process in which sub-stoichiometric amount of oxygen is added, resulting in carbon monoxide and hydrogen products instead. The autothermal reforming combines partial oxidation and steam reforming in a single process [A-18]. In the partial oxidation, hydrocarbons of fossil fuels are partially oxidized with oxygen. The source of heat is derived from the partial oxidation with combustion. The catalyst is not needed for this process, and it is more sulfur tolerant. The pressure requirement of autothermal reforming is lower than partial oxidation. Autothermal reforming and partial oxidation do not need an external heat source. However, both of these processes require pure oxygen which increases complexity and cost with the addition of oxygen separation units. Compared to other fossil fuel reforming technologies, steam reforming (particularly steam methane reforming) is the least expensive and most common method to produce hydrogen in any other fossil fuel reforming [A-16].

Table 2-1. Summary of fossil fuel reforming technologies[A-16].

Technology	Advantages	Disadvantages
Steam reforming	Most developed industrial process No oxygen requirement Lowest operating temperature Best H_2/CO ratio	Highest air emissions
Autothermal reforming	Lower process temperature than partial oxidation Low methane slip	Limited commercial experience Air/oxygen requirement
Partial oxidation	Reduced desulfurization requirement No catalyst requirement Low methane slip	Low H2/CO ratio High operating temperatures Complex handling process

A-3-2 Electrolysis

The water electrolysis is the most basic method to produce hydrogen. It is based on the movement of electrons which are supported by an external circuit. Water electrolysis for hydrogen production with renewable energy attracts lots of attention because it produces huge amount of hydrogen with neither emission of CO_2 nor consumption of fossil fuels or nuclear resources [A-19]. Renewable energy refers to mainly hydropower, wind power and solar power which are easily coupled with water electrolysis [A-20].

The principle of water electrolysis is very simple, and the electrolysis is based on the application of a direct electric current to water to dissociate the water molecules [A-21]. The hydrogen obtained with this water electrolysis has high purity that can exceed

99.999 % with optional impurity removing apparatus [A-22]. In fact, hydrogen by water electrolysis is suitable for use of reverse fuel cell operation with alkaline, polymer electrolyte, or solid oxide fuel cells [A-23]. Table A-2 shows the summary of those reverse operation with several types of fuel cells [A-24].

Table A-2. Basic Chemical reactions and Operating temperature range for different types of Water electrolysis. Alkaline electrolysis, membrane electrolysis, and high temperature electrolysis are used for reversible reaction of alkaline fuel cells, polymer electrolyte fuel cells, and solid oxide fuel cells, respectively [A-24].

Electrolysis	Alkaline Electrolysis	Membrane Electrolysis	High Temperature Electrolysis
Anode Reaction Oxygen Evolution Reaction (OER)	$2OH^- \rightarrow \frac{1}{2}O_2 + H_2O + 2e^-$	$H_2O \rightarrow \frac{1}{2}O_2 + 2H^+ + 2e^-$	$O^{2-} \rightarrow \frac{1}{2}O_2 + 2e^-$
Cathode Reaction Hydrogen Evolution Reaction (HER)	$H_2O + 2e^- \rightarrow H_2 + 2OH^-$	$2H^+ + 2e^- \rightarrow H_2$	$H_2O + 2e^- \rightarrow H_2 + O^{2-}$
Charge Carrier	OH^-	H^+	O^{2-}
Operation Temperature Range	40℃ - 90℃	20℃ - 100℃	700℃ - 1000℃

In fact, water electrolysis has significant overpotential when it is operated. To reduce the overpotential, electrolysis with high temperature electrolysis (steam electrolysis) in Table A-2 is receiving attention [A-25]. The steam electrolysis can be more favorable than water electrolysis for hydrogen production due to the following reason. From the thermodynamic viewpoint, the total energy demand (ΔH) of Equation A-1 can be

expressed as Equation A-2 where ΔG is the electrical energy demand and $T\Delta$S is the heat energy demand.

$$H_2O \leftrightarrows H_2 + 1/2O_2 \quad \text{(A-1)}$$

$$\Delta H = \Delta G + T\Delta S \quad \text{(A-2)}$$

According to previous research, the total energy demand (ΔH) of the reaction of water and steam electrolysis at 1 atm drops considerably over 100 °C, when water shifts from the liquid to gas phase, then it remains almost constant[A-26]. Therefore, steam electrolysis leads to reduced cost for hydrogen production with less consumption of electricity.

A-4 Hydrogen storage

This section explains the hydrogen storage connected with power grid of renewable energy sources. Conventional power grid mainly supplies electricity from fossil fuels. Energy storage with hydrogen can be the key technology to be independent of conventional power grid. Although this chapter focuses on hydrogen, batteries can be also a candidate to store electricity if they store large amount of electricity. As shown in Table A-3, the efficiency from energy input to output with battery is higher than hydrogen [A-27]. It is because batteries do not need the process which converts from electricity to hydrogen [A-28]. Batteries seem to be better than hydrogen to store energy, but there are some disadvantages to them. In fact, they discharge relatively easily and they are unsuitable for large scale storage. As shown in Figure A-5, it is practical to utilize hydrogen for storage capacity over several hundred kilowatt [A-29]. Although flow batteries can be another hopeful energy storage, this storage type has drawbacks regarding

high operating temperature and safety [A-30]. Since hydrogen has the advantage over large-scale storage to diffuse the use of hydrogen in our society, several methods to store hydrogen were suggested. This section introduces them as below.

Table A-3. Technoeconimic comparison between fuel cells and their competitors in the transportation propulsion sector [A-27].

Transportation propulsion technology	**Power level (kW)**	**Efficiency (%)**	**Specific power (kW/kg)**	**Power density (kW/L)**	**Vehicle range (km)**	**Capital cost ($/kW)**
Proton exchange membrane fuel cell (on-board fuel processing)	10–300	40–45	400–1000	600–2000	350–500	100
Proton exchange membrane fuel cell (off-board hydrogen)	10–300	50–55	400–1000	600–2000	200–300	100
Gasoline engine	10–300	15–25	>1000	>1000	600	20–50
Diesel engine	10–200	30–35	>1000	>1000	800	20–50
Diesel engine/battery hybrid	50–100	45	>1000	>1000	>800	50–80
Gasoline engine/battery hybrid	10–100	40–50	>1000	>1000	>800	50–80
Lead-acid or nickel-metal hydride battery	10–100	65	100–400	250–750	100–300	>100

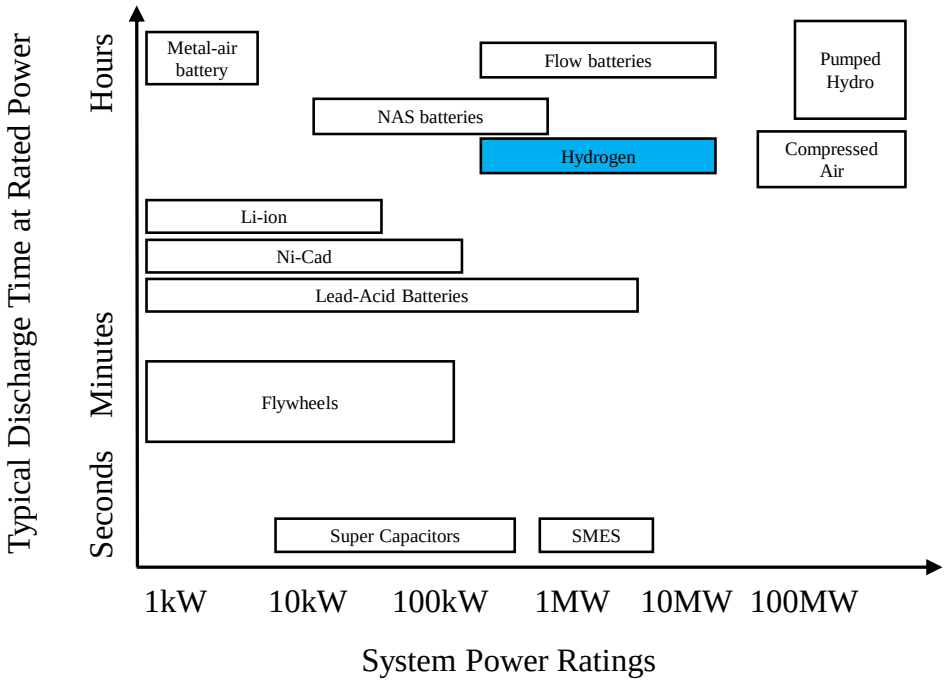

Figure A-5. Typical discharge time and power ratings for energy storage technologies [A-29].

A-4-1 Compressed hydrogen

Compressing hydrogen is the simplest technique to store energy. Gaseous hydrogen has a low density which is 0.0899 g/L at standard temperature and pressure. To store hydrogen more efficiently, the most commonly used way is currently to store hydrogen as compressed gas in gas cylinder. This is widely available although the transportation cost is relatively high when the cylinder has to be transported from one point where they are filled to anywhere. Actually, the volumetric energy density of this storage technique is not high among ways of hydrogen storage. The pressure of compressed hydrogen in a typical laboratory gas cylinder is intentionally less than 15 MPa for safety. Then, to reduce the cost of hydrogen transportation, higher pressure resistant gas cylinder with low cost

is desirable. Although Zheng *et.al.* have already suggested the hydrogen gas cylinder at 77MPa with a tank as shown in Figure A-6, there are still several issues such as cost and safety [A-31]. To solve them, several novel gas cylinder which contains composite with fiber and resin are suggested. Table A-4 shows the advantage and disadvantage of their cylinder [A-32].

There are two approaches to increase the gravimetric and volumetric storage capacities of gas cylinder. First, it is called “cryo-compressed hydrogen” [A-33], and this utilizes cooled gas cylinder to increase volumetric capacity. Thus, by cooling gas cylinder from room temperature to the temperature of liquid nitrogen (77 K), its volumetric capacity increases. Actually, there is also limitation of this storage method because a lot of energy is needed to compress hydrogen gas. Eventually, approximate 20% of the energy of hydrogen is lost due to this method [A-34].

In fact, gas hydrogen storage is not only considered but also liquid hydrogen storage is also done. The density of this liquid hydrogen is much higher than gas hydrogen. However, liquid hydrogen consumes 25-45% of the stored energy of gas hydrogen to liquefy it. In addition, because the boiling point of hydrogen is at approximately -253 °C, it is necessary to maintain this low temperature and bulky insulation, and/or a cooling system is needed [A-35].

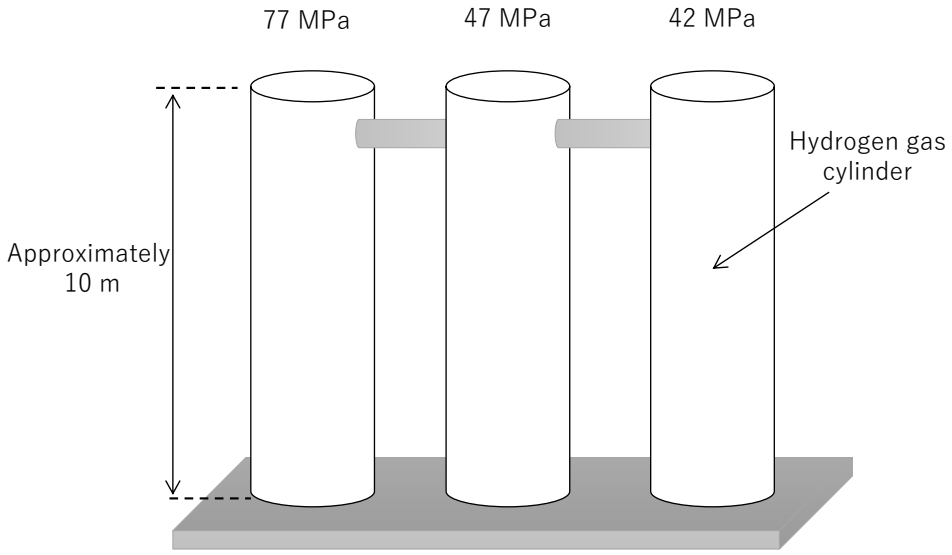

Figure A-6. Schematic model of multifunctional layered stationary hydrogen storage gas cylinders [A-31].

Table A-4. Advantage and disadvantage of several types of gas cylinder in Figure A-10 [A-32].

Technology maturity	Technology maturity	Cost performance	Weight performance
Type 1	Pressure limited to 50 MPa, ++	++	–
Type 2	Pressure not limited, +	+	0
Type 3	For P ≤ 45 MPa (difficulty to pass pressure cycling requirements for 70 MPa)	–	+
Type 4	For P ≤ 100 MPa– First commercial series – liner behaviour in gas to be further studied	–	++

A-4-2 Physisorption

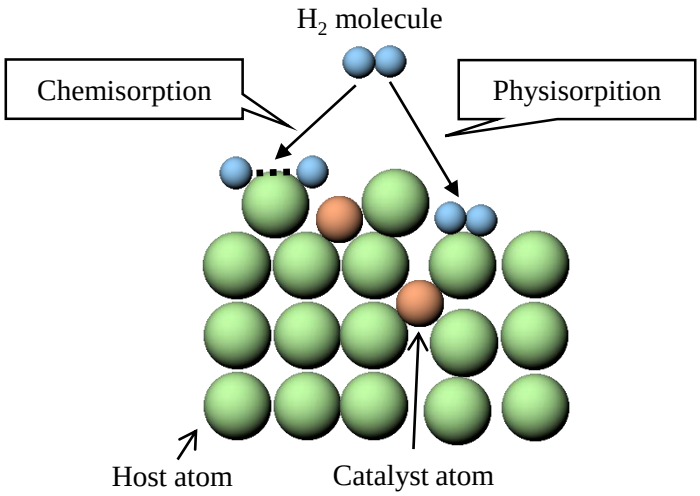

Figure 7. Schematic representation of physisorption and chemisorption with catalyst materials [A-36].

Hydrogen can be stored in its molecular form by physical adsorption (physisorption) on the surface of a porous solid material. Figure 7 is the schematic representation of physisorbed hydrogen. Dalebrook *et al.* summarize the typical gravimetric capacities for a range of materials [A-37]. Physisorption is a reversible process whereby hydrogen can be readily adsorbed onto a surface and released indefinitely without decomposition of the solid or loss of the gas. Due to gas-solid interactions, gas concentration on the surface is higher than that in the bulk. The physisorption storage materials may express gravimetric loadings as either total capacity (the entire quantity of deliverable hydrogen) or excess the capacity (the gain in uptake promoted by an adsorbent).

Among the vast range of materials, carbon-based systems have received particular research interest due to their light weight, high surface area and chemical stabilities. Early experimental data for hydrogen storage in carbon nanomaterials are promising, indicating high hydrogen storage capacities of 7.4 wt% which exceeded 6.5 wt% as target of

Department of Energy (DOE) in united states of America [A-38,A-39,A-40]. Therefore, carbon-based materials for physisorption such as activated carbon, graphite, carbon nanotubes and carbon foams are included in the group of hydrogen storage materials [A-41].

A-4-3 Chemisorption

Chemisorption is the bonding of atoms or molecules to a solid surface (See Figure 7) [A-42]. Storing hydrogen as a chemical metal hydride or complex hydride can provide high volumetric densities and low absorption pressures during hydrogen uptake.

A-4-3-1 Metal hydride

The light weight metals such as Li, Na and Mg form hydrides with high gravimetric hydrogen capacities. There are two possible reactions for hydride metals. They are direct dissociative chemisorption and electrochemical splitting of water. These reactions can be described as:

$$M + \frac{1}{2} H_2 \rightleftarrows MH_x. \quad \text{(A-3)}$$

$$M + \frac{1}{2} H_2O + \frac{1}{2}e^- \rightleftarrows \frac{1}{2} OH^- + MH_x. \quad \text{(A-4)}$$

where *M* represents the metal [A-43].

Because of the high enthalpy of formation, however, high temperature (For example, LiH requires over 650°C.) is needed to release the hydrogen. Magnesium hydride offers large potential with 7.6 wt%, but the amount of desorption is kinetically limited. This has been extensively studied with the goal of improving hydrogen sorption through mechanical modification of the material and through the addition of catalytic materials [A-44].

A-4-3-2 Complex hydrides

Complex hydrides are metal salts, typically containing more than one metal or metalloid, where the anion contains the hydride. Many complex metal hydrides possess hydrogen gravimetric storage capacities and the volumetric density can even surpass that of liquid hydrogen. Table A-5 shows the properties of material hydrides [A-45]. For example, the hydrogen content of $LiBH_4$ is 18 wt%.

Low weight complex hydrides include the alanates $[AlH_4]^-$, amides $[NH_2]^-$, imides $[NH_4]^-$ and borohydrides $[BH_4]^-$. In such systems, the hydrogen is often located at the corners of their tetrahedron. The alanates and borohydrides especially receive lots of attention because of their light weight and the capacity for a large number of hydrogen atoms per metal atom. However, both have relatively poor reversibility and high stability decomposing only at elevated temperatures [A-46].

Table A-5. Material properties of complex hydrides [A-45].

material	CAS no.	density (g/mol)	density (g/cm^3)	hydrogen (wt %)	hydrogen (kg/m^3)	T_m[a] (°C)	$\Delta H_f°$ (kJ/mol)
$LiAlH_4$	16853-85-3	37.95	0.917	10.54	-	190	−119
$NaAlH_4$	13770-96-2	54	1.28	7.41	-	178	−113
$KAlH_4$	-	70.11	-	5.71	53.2	-	-
$Mg(AlH_4)_2$	17300-62-8	86.33	-	9.27	72.3	-	-
$Ca(AlH_4)_2$	16941-10-9	102.1	-	7.84	70.4	>230	-
$LiNH_2$	7782-89-0	22.96	1.18	8.78	103.6	372−400	−179.6
$NaNH_2$	7782-92-5	39.01	1.39	5.15	71.9	210	−123.8
KNH_2	17242-52-3	55.12	1.62	3.66	59.3	338	−128.9
$Mg(NH_2)_2$	7803-54-5	56.37	1.39	7.15	99.4	360	-
$Ca(NH_2)_2$	23321-74-6	72.13	1.74	5.59	97.3	-	−383.4
$LiBH_4$	16949-15-8	21.78	0.66	18.36	122.5	268	−194
$NaBH_4$	16940-66-2	37.83	1.07	10.57	113.1	505	−191
KBH_4	13762-51-1	53.94	1.17	7.42	87.1	585	−229
$Mg(BH_4)_2$	16903-37-0	53.99	0.989	14.82	146.5	320	-
$Ca(BH_4)_2$	17068-95-0	69.76	-	11.47	-	260	-
$Al(BH_4)_3$	16962-07-5	71.51	0.7866	16.78	132	−64.5, 4 4.5	-

A-5. Hydrogen utilization

A-5-1 Fuel cells

To break dependence on fossil fuels, electricity generation with hydrogen is promising way to establish sustainable society (so-called “hydrogen society”). As mentioned before, the society with hydrogen provides electricity following three steps, which are hydrogen production, hydrogen storage, and hydrogen utilization. The hydrogen utilization for electricity generation is mostly associated with fuel cells. Von Spakovsky and Olsommer suggested that a comparison between the energy efficiencies for electricity generation with the principal energy conversion systems such as photovoltaic panels, thermal solar power plants [A-47]. In their research, the fuel cells have the highest energy efficiency after hydropower as shown in Figure A-8. Despite that hydro-power has the highest efficiency among any other energy conversion devices, it plays only a limited role for expansion of electricity generating capacity. According to their previous research, it is due to lack of new exploitable water resources and the environmental implications of building such systems especially in developed countries. Thus, as a next candidate from hydropower, fuel cells receive lots of attention because of having the promising potential for next generation energy conversion device. In this session, several types of fuel cells and properties are described as below.

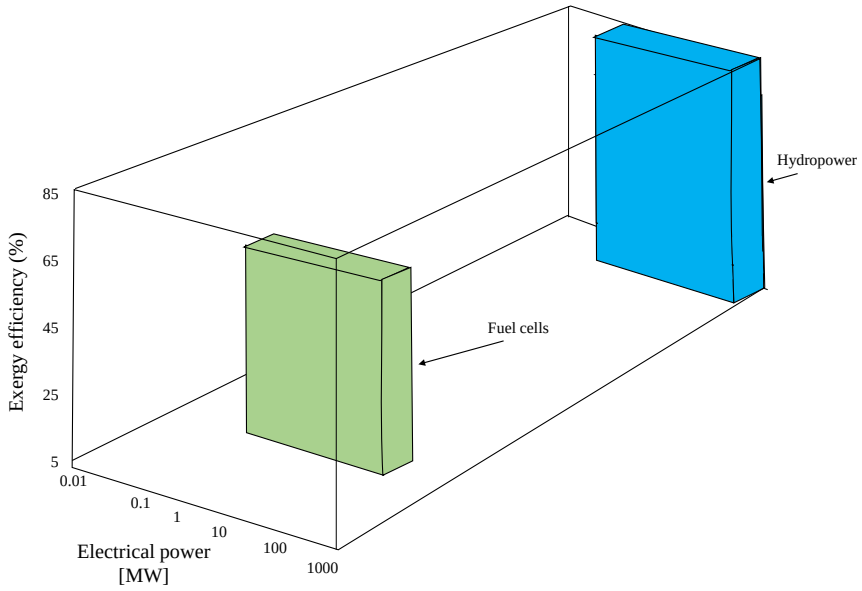

Figure A-8. Exergy efficiencies between fuel cells and hydropower [A-47].

The fuel cells have long history and a primitive fuel cell was first demonstrated in 1839 [A-48]. The fuel cells can convert the chemical energy from H_2 and O_2 into electricity directly following equation A-5. Whereas, they are significantly efficient electrochemical device [A-49].

$$H_2 + \frac{1}{2} O_2 \rightleftarrows H_2O \qquad \text{(A-5)}$$

The types of fuel cells under active development are summarized as shown in Figure A-9 [A-50]. The alkaline fuel cell (AFC), polymer electrolyte fuel cell (PEFC), and phosphoric acid fuel cell (PAFC) stacks essentially require relatively pure hydrogen as a fuel to the anode. Accordingly, an external fuel processor for the hydrogen production before those fuel cells is necessary for the use of hydrocarbon or alcohol. This apparatus is one of the matters not only increasing the complexity and/or cost of the system but also decreasing the overall efficiency as shown in Figure A-10 [A-50]. By contrast, molten-carbonate fuel cell (MCFC) and solid oxide fuel cell (SOFC) have advantage that both CO and H_2 can be electrochemically oxidized at the anode due to high temperature

operation. Yamamoto presented that the efficiency of SOFC is higher than that of MCFC since the operating temperature of SOFC is higher than that of MCFC [A-51]. Therefore, the SOFC has attracted a lot of attention and have been studied extensively [A-52, A-53].

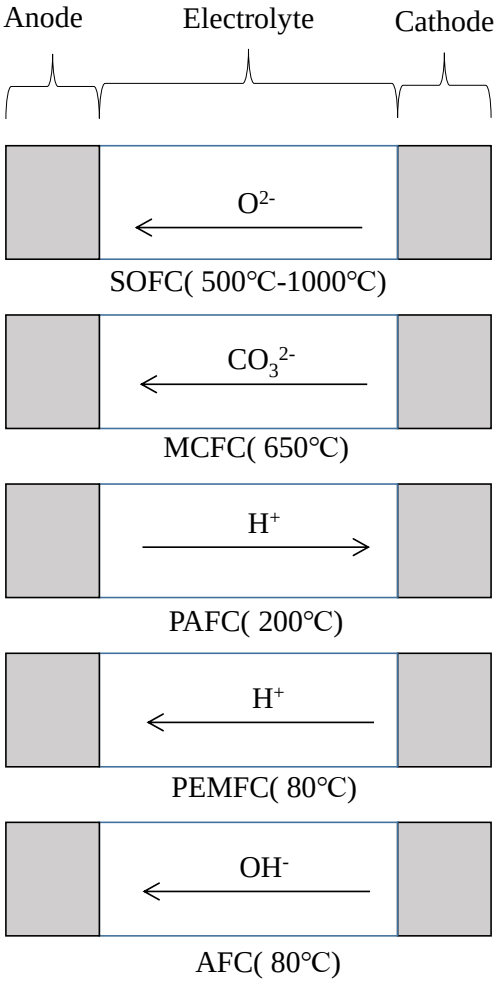

Figure A-9. Summary of types of fuel cells [A-50].

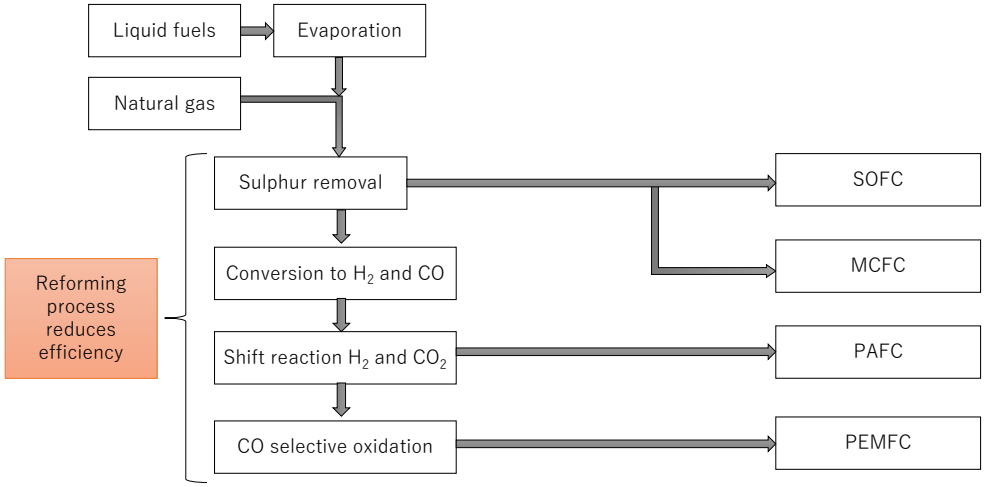

Figure A-10. Fuel cell types and fuel processing [A-50].

A-5-2 SOFCs

In the simplest case, the SOFCs (it is also known as “SOFC”) are based on the overall chemical reaction between hydrogen (at the anode) and oxygen (at the cathode) to produce water. The two electrode compartments are separated by the electrolyte, which serves as a barrier to gas diffusion but allows ion transport, such as oxide ions or protons. In addition, interconnects and seals are also important for SOFCs. Those components have respective issues to improve SOFCs, and Figure A-11 shows them [A-54].

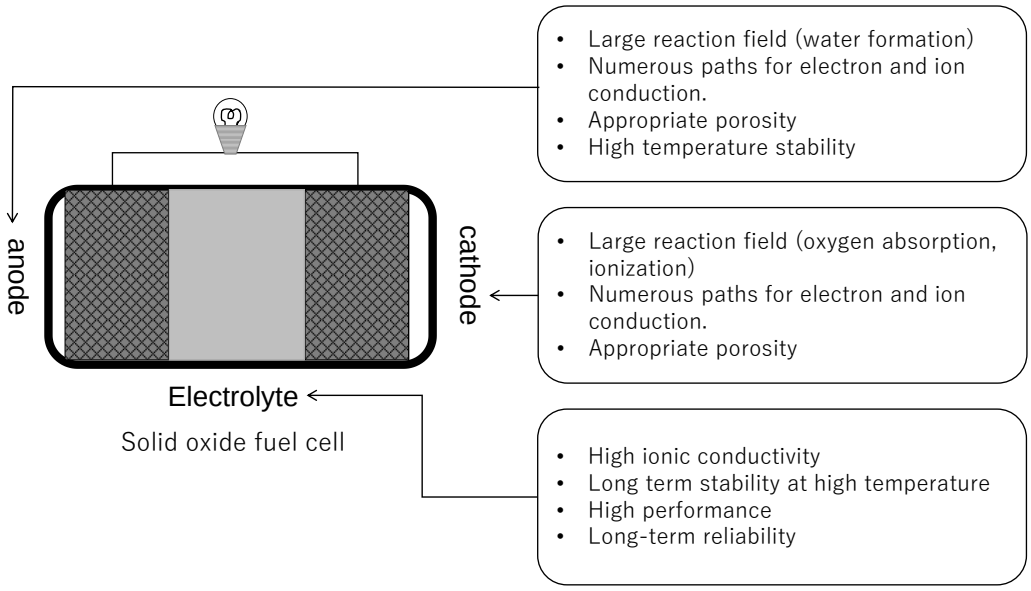

Figure A-11. Related issues for SOFCs [A-54].

Although SOFCs have various issues in the respective components, they are of particular interest due to their potential efficiency in comparison with other types of fuel cells and combustion-based technologies. The flexibility allows them to use hydrocarbon fuels and hence act as a bridging technology between hydrocarbon- and future hydrogen-based economies (hydrogen society). The operating temperature range for SOFCs is currently between 700 ºC and 1000 ºC because it depends on the characteristics of the electrolyte. One of the electrolyte of SOFCs is oxide ions conductor, and this conductor mainly determines the operating temperature. To achieve the operating high ion conductivity, it requires the high temperature over approximately 700°C. Ideally, target ionic conductivities for the electrolyte is expected exceed 0.1 S/cm [A-55]. Because high operating temperature requires start-up time and stability of components, using other materials to reduce the operating temperature are desirable. Accordingly, one of the important challenges to improve the performance of SOFCs is to reduce the operating temperature below 700 ºC. To overcome the challenges, proton conducting oxides (proton

conductor) become the candidate. In fact, Yamazaki et al. suggested that proton conductor could reduce operating temperature to 350°C [A-56]. Figure A-12(a) shows schematics to compare oxide ion conductor with proton conductor. Lower working temperature is advantageous in terms of long-term operation, materials stability, cost, and safety. The role of materials science is to fundamentally find and develop the electrolyte materials. They should support high ion conductivities (and negligible electronic conductivities) at lower temperatures, together with good chemical stability, and low thermal expansion [A-57]. Such breakthroughs underpin applied research, and depend simultaneously upon exploring new classes of compounds. Therefore, it is quite important to understand the structural and mechanistic properties of ion conductors at the atomic level [A-57].

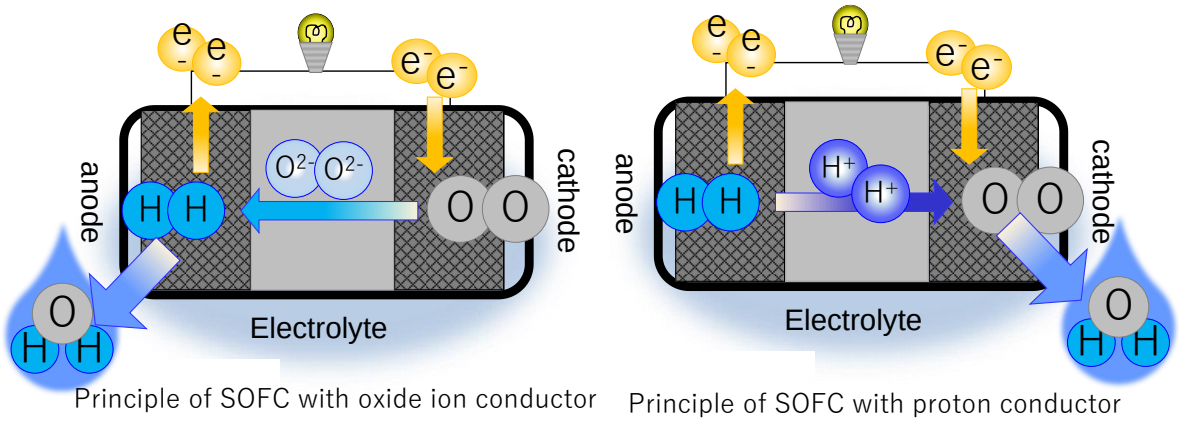

Figure A-12. Schematic model of (a) oxide ion conducting electrolyte, and (b) proton conducting electrolyte in SOFC [A-55].

A-5-2-1 Oxide-ion conductors

Oxide ion conductors are used for electrolyte of SOFCs as shown in Figure A-12(a). There are several types of crystal structures for oxide-ion conductors. Most conventional oxide-ion conducting materials have fluorite type, AO_2, where A is a tetravalent cation.

In this structure, the cations occupy face-centered positions in a cubic unit cell with anions in the eight tetrahedral sites between them. The best known fluorite-type oxide-ion conductor is acceptor-doped ZrO_2. The reaction can be described following Kröger–Vink notation,

$$MO + Zr_{Zr}^{\times} + O_O^{\times} \rightleftarrows M_{Zr}^{'} + V_O^{\cdot\cdot} + ZrO_2 \quad \text{(A-6)}$$

$$R_2O_3 + 2Zr_{Zr}^{\times} + O_O^{\times} \rightleftarrows 2R_{Zr}^{'} + V_O^{\cdot\cdot} + 2ZrO_2 \quad \text{(A-7)}$$

,where M is a divalent cation, R is a trivalent cation, and $V_O^{\cdot\cdot}$ is a compensating oxygen vacancy. Typical subvalent dopants are Ca^{2+} (as M) and Y^{3+} (as R) which produce calcia-stabilized zirconia (CSZ) and yttria-stabilized zirconia (YSZ), respectively. The latter exhibits good oxide-ion conductivity above 700 °C [A-58,A-59].

On the other hand, the conductivity of YSZ is presented in Figure A-13 (This figure has several other materials, which is discussed in previous research [A-55]). YSZ is the most common oxide electrolyte material, and has been the mainstay of commercially SOFCs [A-58,A-59]. However, its high operating temperature (800-1000 °C) makes it problematic in small-scale applications [A-60]. Extensive research has also been carried out into Sc-doped ZrO_2 (ScSZ), which exhibits superior ionic conductivity [A-61, A-62, A-63], but its utilization is limited on account of the high cost of scandium [A-55].

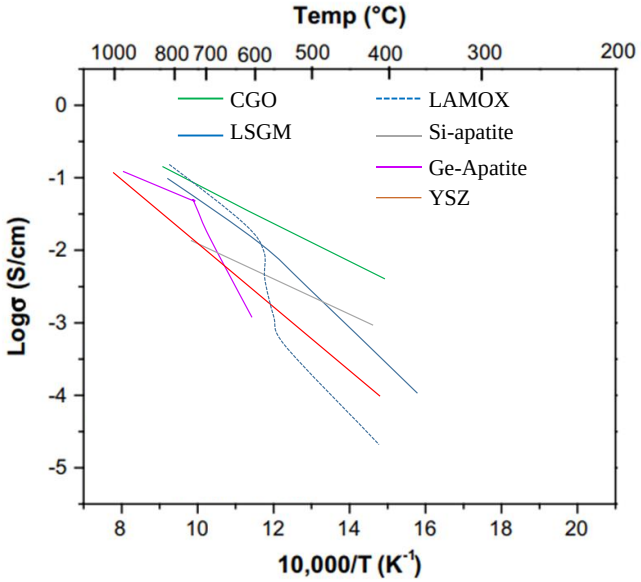

Figure A-13. Total conductivities of several oxide-ion conductors as a function of inverse temperature: YSZ, $(ZrO_2)_{0.92}(Y_2O_3)_{0.08}$; CGO, $Ce_{0.8}Gd_{0.2}O_{1.9}$; LSGM, $La_{0.9}Sr_{0.1}Ga_{0.8}Mg_{0.2}O_{2.85}$; LA*M*OX, $La_2Mo_2O_9$, Si-apatite, $La_{10}(SiO_4)_6O_3$, and Ge-apatite, $La_{10}(GeO_4)_6O_3$ [A-55].

Some perovskite structure can also be oxide ion conductors. The structure is typically described as ABO_3. Two representations of the cubic perovskite structure of $laGaO_3$; (a) La centered unit cell, and (b) corner-shaped GaO_6 octahedra with La centered on 12-coodinate sites. Large red sphere is O^{2-}, light green sphere is La^{3+} and small blue sphere is Ga^{3+} [A-55]. The large *A* cation is coordinated by twelve anions, with the *B* cation occupying a six-coordinate sites, forming a network of corner-sharing BO_6 octahedra. Tilting of these octahedra leads to deviations from the ideal cubic symmetry. A widely studied perovskite-structured oxide with possible applications is doped lanthanum gallate ($LaGaO_3$). The high ion conductivity of (Sr,Mg)-doped $LaGaO_3$ (general formula is $La_{1-x}Sr_xGa_{1-y}Mg_yO_{3-\delta}$ and it is often termed LSGM) was first reported in 1994 by Ishihara *et al.*[A-64], and by Feng and Goodenough [A-65]. This material exhibits pure

ionic conductivity over a very wide range of oxygen partial pressure ($10^{-20} < pO_2 < 1$), with values higher than those of YSZ even at relatively low temperatures for composition $La_{0.9}Sr_{0.1}Ga_{0.8}Mg_{0.2}O_{3-\delta}$, as shown in Figure A-13 [A-55]. In comparison to the fluorite oxides, there have been fewer studies on defect clustering in perovskite oxides. In addition, there are other several types of crystal structure for oxide-ion conductors, and they are more summarized by Malavasi *et. al*.[A-55].

A-5-2-2 Proton Conducting oxides

Proton conducting oxides (sometimes they are called “proton conductors”.) can be expected to apply to the electrolyte of SOFCs (See Figure A-12(b)) [A-66,A-67]. The proton conducting oxides are metal oxides, and they were found by Iwahara *et al.* in 1981. They reported strontium and barium cerates based proton conducting oxides [A-68, A-69]. After more than 20 years of active research, the perovskite-type cerates and zirconates have been widely accepted as well-established proton conducting oxides [A-70,A-71,A-72]. The crystal structures of these materials are based on the perovskite structure. Protonic defects (protons) are formed by the dissociative absorption of water at the surface of oxide-ion vacancies. One water molecule from the gas phase dissociates into a hydroxide ion and a proton. The oxygen of hydroxide fills an oxide-ion vacancy, and a covalent bond was formed between proton and lattice oxygen. In Kröger-Vink notation, this reaction can be written as Equation A-8.

$$H_2O + V_O^{\bullet\bullet} \rightleftarrows O_O^{\times} + 2H_i^{\bullet} \qquad \text{(A-8)}$$

,where $V_O^{\bullet\bullet}$, $O_O^{\times}$, and $H_i^{\bullet}$ denote oxide ion vacancy, oxide ion at its regular site, and proton, respectively, in Kröger-Vink notation. Due to this hydration reaction, cell volume of proton conducting oxides expands [A-73]. Pure $SrCeO_3$, $BaCeO_3$, $CaZrO_3$ and

$SrZrO_3$ hardly exhibit proton incorporation unless doped with subvalent cations. In the $BaCeO_3$ system, for example, replacing Ce^{4+} ions with M^{3+}cations (typically Y^{3+}) is charge-compensated by formation of an oxygen vacancy:

$$2Ce_{Ce}^{\times} + M_2O_3 + O_O^{\times} \rightleftarrows 2M_{Ce}^{\cdot} + V_O^{\cdot\cdot} + 2CeO_2 \qquad \text{(A-9)}$$

The energy of water incorporation in such systems has been found (from both experimentally and theoretically results) to be exothermic reaction for doped and undoped cerates and zirconates [A-74, A-75, A-76], which is consistent with the observation that proton uptake in perovskite structure increases with decreasing temperature. Furthermore, water incorporation in doped systems is more exothermic than in undoped systems. A typical conductivity as function of inverse temperature curve for 10 mol% Y-doped parent crystal is shown in Figure A-14. Obviously, in comparison with other proton conducting oxides,

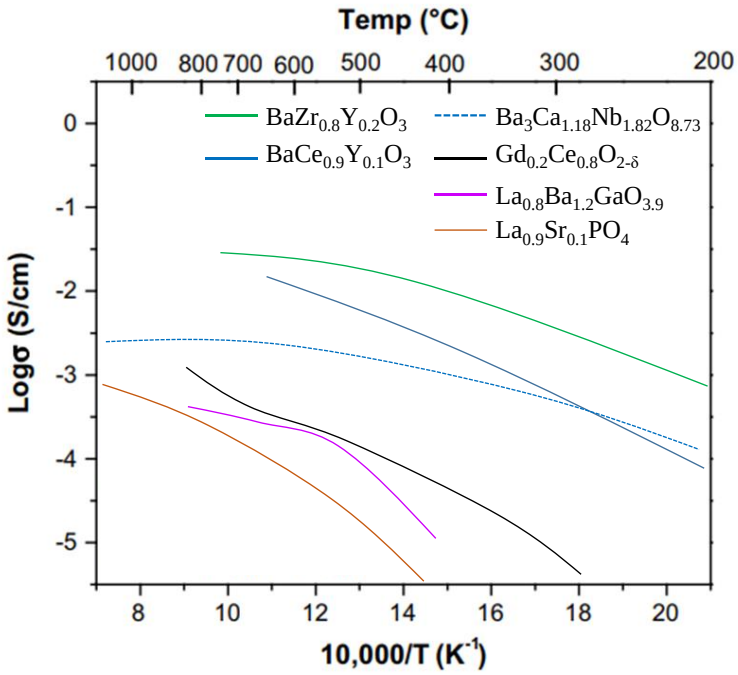

Figure A-14. Conductivities of some widely known proton conducting oxides as a function of inverse temperature:

$BaCe_{0.9}Y_{0.1}O_3$ (BCO); $BaZr_{0.8}Y_{0.2}O_3$ (BZO); $La_{0.9}Sr_{0.1}PO_4$;

$Ba_3Ca_{1.18}Nb_{1.82}O_{8.73}$ (BCN); $La_{0.99}Ca_{0.01}NbO_4$; $La_{0.8}Ba_{1.2}GaO_{3.9}$ (LBGO) [A-55].

In fact, currently yttrium doped barium cerate system shows very high proton conductivity. Detailed characterization of the structures of many cerates as a function of temperature and dopant concentration has been reported such as phase transforming [A-77, A-78, A-79, A-78].

The proton conducting mechanism has been. For example, quantum molecular dynamics simulations of these perovskite systems have shown that proton transport involves hopping of a lone proton between oxide ions, as well as rotational motion of the hydroxyl unit as shown in Figure A-15 [A-75,A-80]. Both computational simulation and experiment confirm that the rate-limiting step is the proton transfer between oxide ions, while the rotational motion is fast with a low activation barrier [A-55,A-81,A-82].

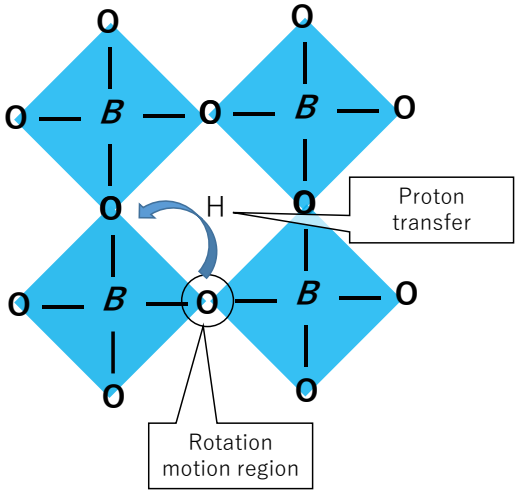

Figure A-15. Schematic model of proton transferring described in previous report[A-75].

In addition, these days, it has been found that this hopping mechanism plays an important role in determining the performance of proton conducting oxides. According to the report of Yamazaki *et. al.*, protons energetically prefers to be trapped by dopants after hydration, and the proton does not conduct freely in the perovskite structure before overcoming activation energy between dopants and *A*-site as shown in Figure A-16 [A-83]. Then, the performance is depending on the height of activation barrier between dopant and *B*-site. Although it has been nearly 40 years since the proton conductor has been found, the indicator to determine the proton conductivity of the proton conducting oxides is still unclear. The Figure A-17 summarizes the *A*-site, *B*-site, and dopant of perovskite structure of the proton conductor found so far by using the periodic table [A-84]. The composition of *A*-site, *B*-site, and dopant is biased to some extent in the periodic table, but the indicator for obtaining the desired performance still remains unclear.

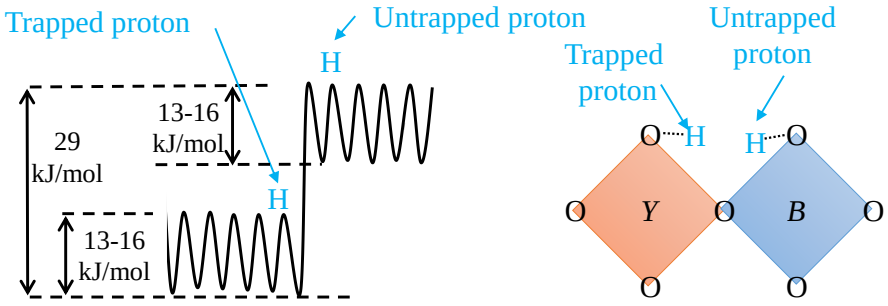

(a) Proton activation energy from Y to *B*-site (b) 2-dimentioanl image of perovskite

Figure A-16 Proton trapping model reported by Yamazaki *et.al.* (a). 2-dimentional model of trapped and trap-free H^+(b). (Y: dopant) [A-85].

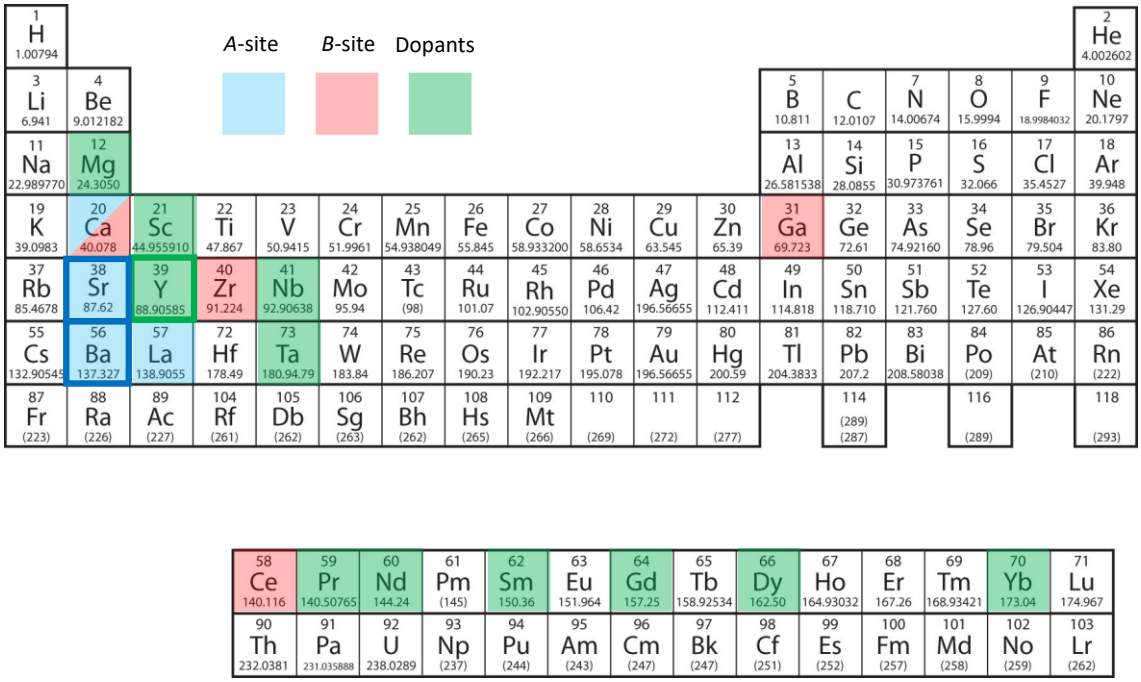

Figure A-17 Reported elements of *A*-site, *B*-site, and dopants for proton conducting oxides [A-86].

A-5-2-3 Hydride ion conducting material

It has been known that hydride ion (H^-) exists in a metal oxide, but H^- conduction had not observed in metal oxide of perovskite structure [A-87, A-88]. In this year, Kobayashi *et al.* reported another ion conduction in metal oxides. The conduction specie is hydride ion, and the report is summarized as below.

As series of composition which keep H^- stable in the lattice, $La_{2-x-y}Sr_{x+y}LiH_{1-x+y}O_{3-y}$(LSLHO) was prepared. Because H^- itself is not stable, Li, Sr, and La which have better ability to donate electrons than H^- were chosen to let it stay in lattice. The series of LSLHO were synthesized by treating the appropriate starting materials in sealed Au

capsules at high pressure and high temperature.

La_2LiHO_3 which is one of the LSLHO series had the crystal structure of K_2NiF_4 - type, and the two apical sites of LiX_6 were occupied only by O^{2-}. On the other hand, the four in plane apexes (in frame B of Figure A-18(a)) were occupied by O^{2-} and H^-.

The series of LSLHO provided the conductivity. Furthermore, with one of the LSLHO series, one cell which can be described as $Ti/La_2LiHO_3/TiH_2$ was established for analysis of the electromotive force (EMF). During this conduction, discharged capacity was also observed with fixed current as 0.5μA.

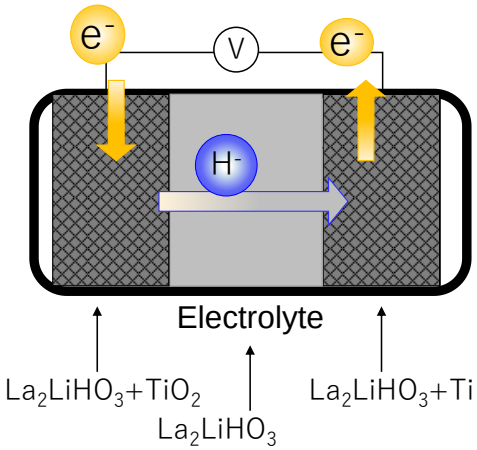

Figure A-18. Schematic model of hydride ion conduction reported by Kobayashi et al.[A-89].

The equation and schematic model of H^- conduction can be described as shown in equation A-10 and A-11 and Figure A-18 respectively. In addition, this electrolyte (La_2LiHO_3) can conduct proton when electrical current runs from the outside power source.

$$\text{(Anode) } Ti + xH^- \rightleftarrows TiH_2 + xH^- \qquad \text{(A-10)}$$

$$\text{(Cathode) } Ti + xH^- \rightleftarrows TiH_x + xe^- \quad \text{(A-11)}$$

Since hydride ion conduction in metal oxide was found in this year, a lot of properties are still unclear. Especially, H^- easily donates electrons into oxide based material as shown in Equation (A-12) [A-90], it is important to let H^- be stable in the lattice [A- 89]. Therefore, advanced research regarding H^- ion conducting materials is expected.

$$H^- + O^{2-} \rightleftarrows 2e^- + OH^- \quad \text{(A-12)}$$

A-5-3 Hydrogen internal combustion engine

In terms of hydrogen utilization, fuel cells are not only option. In fact, research on hydrogen engine which could take the place of conventional internal combustion engine (ICE) such as gasoline engine has proceeded [A-91],[A-92]. The hydrogen internal combustion engine (H_2 ICE) combines the fuel (hydrogen) and oxidant (air) to produce electricity in a multi-step process. The process involves combustion to produce thermal energy from the internal chemical energy of the fuel. This thermal energy is converted into mechanical energy and finally this mechanical energy is converted into electrical energy with a generator. Eventually, system efficiency decreases due to number of energy conversion process, and H_2ICE is limited by the carnot efficiency between low and high working temperatures [A-46].

A-6. Summary

This chapter introduced the production, storage and utilization of hydrogen that stores excess energy of renewable energy with social background. Our society has developed with dependence on fossil fuels. What we need to pay attention is not when fossil fuels dry up but when fossil fuels begin to phase out. Because the energy demand is expected to keep increasing, we need to find alternative energy to compensate the demand at some point. Using hydrogen as the energy carrier will be a promising way because it is suitable for large scale storage. Furthermore, we have to finally obtain energy source with environmentally friendly. Therefore, it is one of the most viable way to correspond to the demand expanding that producing hydrogen with renewable energy. However, the producing hydrogen currently relays on fossil fuels due to the production cost. The priority of research and development is to make the cost with renewable energy decrease less than fossil fuels.

Reference

(A-1) International Energy Agency (IEA): Key world energy Statistics, 2015.

(A-2) Energy Information Administration, International Energy Outlook 2016, U.S. Department of Energy, 2016.

(A-3) BP Statistical Review, June 2016.

(A-4) Mohr, S.; Wang, J.; Ellem, G.; Ward, J. & Giurco, D., "Projection of world fossil fuels by country", *Fuel,* **141**, pp. 120-135, 2015.

(A-5) Karl, T.R., Arguez, A., Huang, B., Lawrimore, J.H., McMahon, J.R., Menne, M.J., Peterson, T.C., Vose, R.S. & Zhang, H.M., (2015)

"CLIMATE CHANGE. Possible artifacts of data biases in the recent global surface warming hiatus", *Science,* 348(6242), pp. 1469-1472.

(A-6) Zarfl, C., Lumsdon, A.E., Berlekamp, J., Tydecks, L. & Tockner, K., (2015) "A global boom in hydropower dam construction", *Aquatic Sciences,* 77(1), pp. 161-170.

(A-7)Wang, C. & Nehrir, M.H., (2008) "Power management of a stand-alone wind/photovoltaic/fuel cell energy system", *IEEE Transactions on Energy Conversion,* 23(3), pp. 957-967.

(A-8) Elam, C.C., Padró, C.E.G., Sandrock, G., Luzzi, A., Lindblad, P. & Hagen, E.F., (2003) "Realizing the hydrogen future: the International Energy Agency's efforts to advance hydrogen energy technologies", *International Journal of Hydrogen Energy,* 28(6), pp. 601-607.

(A-9) Cetin, E., Yilanci, A., Oner, Y., Colak, M., Kasikci, I. & Ozturk, H.K., (2009) "Electrical analysis of a hybrid photovoltaic-hydrogen/fuel cell energy system in Denizli, Turkey", *Energy and Buildings,* 41(9), pp. 975-981.

(A-10) Yilanci, A., Dincer, I. & Ozturk, H., (2009) "A review on solar-hydrogen/fuel cell hybrid energy systems for stationary applications", *Progress in Energy and Combustion Science,* 35(3), pp. 231-244.

(A-11) F. Orecchini, (2006) “The era of the energy vectors”, *International Journal of Hydrogen Energy*, 14(31), pp. 1951-1954.

(A-12) O'hayre, R., Cha, S., Prinz, F.B. & Colella, W., (2016) *Fuel cell fundamentals,* John Wiley & Sons. p.22.

(A-13) Zegers, P., (2006) "Fuel cell commercialization: The key to a hydrogen economy", *Journal of Power Sources,* 154(2), pp. 497-502.

(A-14) Behling, N., Williams, M.C. & Managi, S., (2016) "Japan Has Great Expectations for a Hydrogen Society", *ECS Transactions,* 71(1), pp.1-12.

(A-15) Kasai, N., Fujimoto, Y., Yamashita, I. & Nagaoka, H., (2016) "The qualitative risk assessment of an electrolytic hydrogen generation system", *International Journal of Hydrogen Energy,* 41(30), pp.13308-13314.

(A-16) Dincer, I. & Acar, C., (2015) "Review and evaluation of hydrogen production methods for better sustainability", *International Journal of Hydrogen Energy,* 40(34), pp. 11094-11111.

(A-17) Choudhary, V., Uphade, B. & Belhekar, A., (1996) "Oxidative conversion of methane to syngas over LaNiO3 perovskite with or without simultaneous steam and CO2 reforming reactions: influence of partial substitution of La and Ni", *Journal of Catalysis,* 163(2), pp. 312-318.

(A-18) Amirshaghaghi, H., Zamaniyan, A., Ebrahimi, H. & Zarkesh, M., (2010) "Numerical simulation of methane partial oxidation in the burner and combustion chamber of autothermal reformer", *Applied Mathematical Modelling,* 34(9), pp. 2312-2322.

(A-19) Ivy, J., (2004), *Summary of electrolytic hydrogen production: milestone completion report.*

(A-20) Kodama, T. & Gokon, N., (2007) "Thermochemical cycles for high-temperature solar hydrogen production", *Chemical reviews,*107(10), pp. 4048-4077.

(A-21) Mallouk, T.E., (2013) "Water electrolysis: Divide and conquer", *Nature*

chemistry, 5(5), pp. 362-363.

(A-22) Barbir, F. 2005, "PEM electrolysis for production of hydrogen from renewable energy sources", *Solar Energy,* 78(5), pp. 661-669.

(A-23) Carmo, M., Fritz, D.L., Mergel, J. & Stolten, D., (2013) "A comprehensive review on PEM water electrolysis", *International Journal of Hydrogen Energy,* 38(12), pp. 4901-4934.

(A-24) Rashid, M., Al Mesfer, M.K., Naseem, H. & Danish, M., (2015) "Hydrogen production by water electrolysis: a review of alkaline water electrolysis, PEM water electrolysis and high temperature water electrolysis", *Int J Engg Adv Techno l,* 4, pp. 2249-8958.

(A-25) Matsumoto, H. 2016, "(Invited) Steam Electrolysis Using Proton-Conducting Perovskite", *PRiME 2016/230th ECS Meeting (October 2-7, 2016)* Ecs.

(A-26) Bi, L., Boulfrad, S. & Traversa, E., (2014) "Steam electrolysis by solid oxide electrolysis cells (SOECs) with proton-conducting oxides", *Chemical Society Reviews,* 43(24), pp. 8255-8270.

(A-27) Sharaf, O.Z. & Orhan, M.F., (2014) "An overview of fuel cell technology: Fundamentals and applications", *Renewable and Sustainable Energy Reviews,* 32, pp. 810-853.

(A-28) Bossel, U., (2003) "Efficiency of hydrogen fuel cell, diesel-SOFC-hybrid and battery electric vehicles", Technical report, European Fuel Cell Forum, Morgenacherstrasse.

(A-29) González, E.L., Llerena, F.I., Pérez, M.S., Iglesias, F.R. & Macho, J.G.,

(2015) "Energy evaluation of a solar hydrogen storage facility: comparison with other electrical energy storage technologies", *International Journal of Hydrogen Energy,* 40(15), pp. 5518-5525.

(A-30) Soloveichik, G.L., (2015) "Flow batteries: current status and trends", *Chemical reviews,* 115 (20), pp. 11533-11558.

(A-31) Zheng, J., Liu, X., Xu, P., Liu, P., Zhao, Y. & Yang, J., (2012) "Development of high pressure gaseous hydrogen storage technologies",*International Journal of Hydrogen Energy,* 37(1), pp. 1048-1057.

(A-32) Barthélémy, H., Weber, M. & Barbier, F., (2016) "Hydrogen storage: Recent improvements and industrial perspectives", *International Journal of Hydrogen Energy*

(A-33) Ahluwalia, R., Hua, T., Peng, J., Lasher, S., McKenney, K., Sinha, J. & Gardiner, M., (2010) "Technical assessment of cryo-compressed hydrogen storage tank systems for automotive applications", *International Journal of Hydrogen Energy,* 35(9), pp. 4171-4184.

(A-34) Suh, M.P., Park, H.J., Prasad, T.K. & Lim, D., (2011) "Hydrogen storage in metal–organic frameworks", *Chemical reviews,* 112(2), pp. 782-835.

(A-35) Hirose, K. & Hirscher, M., (2010) *Handbook of hydrogen storage: new materials for future energy storage,* John Wiley & Sons.

(A-36) Srinivasan, S.S. & Sharma, P.C., (2012) "*Development of Novel Polymer Nanostructures and Nanoscale Complex Hydrides for Reversible*

Hydrogen Storage", INTECH Open Access Publisher.

(A-37) Dalebrook, A.F., Gan, W., Grasemann, M., Moret, S. & Laurenczy, G., (2013) "Hydrogen storage: beyond conventional methods", *Chemical Communications,* 49(78), pp. 8735-8751.

(A-38) Perlt, E., Friedrich, J., Von Domaros, M. & Kirchner, B., (2011) "Importance of structural motifs in liquid hydrogen fluoride", *ChemPhysChem,* 12(17), pp. 3474-3482.

(A-39) Kato, Y., Otsuka, K. & Liu, C.Y., (2005) "Carbon dioxide zero-emission hydrogen carrier system for fuel cell vehicle", *Chemical Engineering Research and Design,* 83(7) A, pp. 900-904.

(A-40) Dillon, A.C. & Heben, M.J., (2001) "Hydrogen storage using carbon adsorbents: Past, present and future", *Applied Physics A: Materials Science and Processing,* 72(2), pp. 133-142.

(A-41) Schlapbach, L. & Züttel, A., (2001) "Hydrogen-storage materials for mobile applications", *Nature,* 414(6861), pp. 353-358.

(A-42) Norsko, J., (1990) "Chemisorption on metal surfaces", *Reports on Progress in Physics,* 53(10), p. 1253.

(A-43) Sakintuna, B., Lamari-Darkrim, F. & Hirscher, M., (2007) "Metal hydride materials for solid hydrogen storage: a review", *International Journal of Hydrogen Energy,* 32(9), pp. 1121-1140.

(A-44) Webb, C.J., (2015) "A review of catalyst-enhanced magnesium hydride as a hydrogen storage material", *Journal of Physics and Chemistry of Solids,* 84(1), pp. 96-106.

(A-45) Orimo, S., Nakamori, Y., Eliseo, J.R., Züttel, A. & Jensen, C.M., (2007)

"Complex hydrides for hydrogen storage", *Chemical reviews,* 107(10), pp. 4111-4132.

(A-46) Abdin, Z., Webb, C.J. & Gray, E.M., (2015), "Solar hydrogen hybrid energy systems for off-grid electricity supply: A critical review", *Renewable and Sustainable Energy Reviews,* 52, pp. 1791-1808.

(A-47) von Spakovsky, M.R. & Olsommer, B., (2002) "Fuel cell systems and system modeling and analysis perspectives for fuel cell development", *Energy Conversion and Management,* 43(9–12), pp. 1249-1257.

(A-48) Grove, W. R., (1839) “On voltaic series and the combination of gases by platinum” *Phil. Mag.*, 3 (14), pp.127-130.

(A-49) Larminie, J., Dicks, A. & McDonald, M.S., (2003), *Fuel cell systems explained,* Wiley New York, p.2.

(A-50) Steele, B.C.H., (2001) "Materials for fuel-cell technologies", *Nature,* 414(6861), pp. 345-352.

(A-51) Yamamoto, O., (2000) "Solid oxide fuel cells: fundamental aspects and prospects", *Electrochimi. Acta,* 45(15-16) pp. 2423-2435.

(A-52) Kim, Y., He, J., Biegalski, M.D., Ambaye, H., Lauter, V., Christen, H.M., Pantelides, S.T., Pennycook, S.J., Kalinin, S.V. & Borisevich, A.Y., (2012) "Probing oxygen vacancy concentration and homogeneity in solid-oxide fuel-cell cathode materials on the subunit-cell level", *Nature Materials,* 11(10), pp. 888-894.

(A-53) Wachsman, E.D. & Lee, K.T., (2011) "Lowering the temperature of solid oxide fuel cells", *Science,* 334(6058), pp. 935-939.

(A-54) Mahato, N., Banerjee, A., Gupta, A., Omar, S. & Balani, K., (2015), "Progress in material selection for solid oxide fuel cell technology: A review", *Progress in Materials Science,* 72, pp. 141-337.

(A-55) Malavasi, L., Fisher, C.A. & Islam, M.S., (2010) "Oxide-ion and proton conducting electrolyte materials for clean energy applications: structural and mechanistic features", *Chemical Society Reviews,* 39(11), pp. 4370-4387.

(A-56) Yamazaki, Y., Blanc, F., Okuyama, Y., Buannic, L., Lucio-Vega, J.C., Grey, C.P. & Haile, S.M., (2013) "Proton trapping in yttrium-doped barium zirconate", *Nature materials,* 12(7), pp. 647-651.

(A-57) Marrocchelli, D., Perry, N.H. & Bishop, S.R., (2015) "Understanding chemical expansion in perovskite-structured oxides", *Physical Chemistry Chemical Physics,* 17(15), pp. 10028-10039.

(A- 58) Haile, S.M., (2003) "Fuel cell materials and components", *Acta Materialia,* 51(19), pp. 5981-6000.

(A-59) Jacobson, A.J. (2009), "Materials for solid oxide fuel cells†", *Chemistry of Materials,* 22(3), pp. 660-674.

(A-60) Lashtabeg, A. & Skinner, S.J. (2006), "Solid oxide fuel cells—a challenge for materials chemists?", *Journal of Materials Chemistry,* 16(31), pp. 3161-3170.

(A-61) Devanathan, R., Thevuthasan, S. & Gale, J.D. 2009, "Defect interactions and ionic transport in scandia stabilized zirconia", *Physical Chemistry Chemical Physics,* 11(26), pp. 5506-5511.

(A-62) Sarat, S., Sammes, N. & Smirnova, A., (2006) "Bismuth oxide doped scandia-stabilized zirconia electrolyte for the intermediate temperature

solid oxide fuel cells", *Journal of Power Sources,*160(2), pp. 892-896.

(A-63) Badwal, S., Ciacchi, F. & Milosevic, D., (2000) "Scandia–zirconia electrolytes for intermediate temperature solid oxide fuel cell operation", *Solid State Ionics,* 136, pp. 91-99.

(A-64) Ishihara, T., Matsuda, H. & Takita, Y., (1994) "Doped LaGaO3 perovskite type oxide as a new oxide ionic conductor", *Journal of the American Chemical Society,* 116(9), pp. 3801-3803.

(A-65) Feng, M. & Goodenough, J., (1994) "A superior oxide-ion electrolyte", *European journal of solid state and inorganic chemistry,* 31(8-9), pp. 663-672.

(A-66) Kreuer, K., (2001) "On the development of proton conducting polymer membranes for hydrogen and methanol fuel cells", *Journal of Membrane Science,* 185(1), pp. 29-39.

(A-67) Norby, T., (1999) "Solid-state protonic conductors: principles, properties, progress and prospects", *Solid State Ionics,* 125(1), pp. 1-11.

(A-68) Iwahara, H., Uchida, H., Ono, K. & Ogaki, K., (1988) "Proton conduction in sintered oxides based on BaCeO3", *Journal of the Electrochemical Society,* 135(2), pp. 529-533.

(A-69) Iwahara, H., (1988) "High temperature proton conducting oxides and their applications to solid electrolyte fuel cells and steam electrolyzer for hydrogen production", *Solid State Ionics,* 28, pp. 573-578.

(A-70) Yajima, T., Kazeoka, H., Yogo, T. & Iwahara, H., (1991) "Proton conduction in sintered oxides based on CaZrO3", *Solid State Ionics,* 47(3-4), pp. 271-275.

(A-71) Yajima, T., Suzuki, H., Yogo, T. & Iwahara, H., (1992) "Protonic conduction in SrZrO3-based oxides", *Solid State Ionics,* 51(1), pp. 101-107.

(A-72) Katahira, K., Kohchi, Y., Shimura, T. & Iwahara, H., (2000) "Protonic conduction in Zr-substituted BaCeO3", *Solid State Ionics,* 138(1–2), pp. 91-98.

(A-73) Basbus, J., Arce, M., Prado, F., Suescun, L., Caneiro, A. & Mogni, L., (2016) "A High Temperature Study on the Structure, Linear Expansion, Thermodynamic Stability and Electrical Properties of the BaCe0.8Pr0.2O3-δ Perovskite", *Journal of the Electrochemical Society,* 163(6), pp. F516-F522.

(A-74) Islam, M.S. & Slater, P.R., (2009) "Solid-state materials for clean energy: insights from atomic-scale modeling", *MRS Bulletin,* 34(12), pp. 935-941.

(A-75)Kreuer, K., (2003), "Proton-conducting oxides", *Annual Review of Materials Research,* 33(1), pp. 333-359.

(A-76)Kreuer, K., Münch, W., Ise, M., He, T., Fuchs, A., Traub, U. & Maier, J., (1997) "Defect interactions in proton conducting perovskite-type oxides", *Berichte der Bunsen-Gesellschaft,* 101(9), pp. 1344-1350.

(A-77)Knight, K., (2000) "Powder neutron diffraction studies of BaCe0.9Y0.1O2.95 and BaCeO3 at 4.2 K: a possible structural site for the proton", *Solid State Ionics,* 127(1), pp. 43-48.

(A-78)Malavasi, L., Ritter, C. & Chiodelli, G., (2008) "Correlation between thermal properties, electrical conductivity, and crystal structure in the

BaCe0.80Y0.20O2.9 proton conductor", *Chemistry of Materials,* 20(6), pp. 2343-2351.

(A-79)Oishi, M., Yashiro, K., Sato, K., Mizusaki, J., Kitamura, N., Amezawa, K., Kawada, T. & Uchimoto, Y., (2008) "Oxygen nonstoichiometry of the perovskite-type oxides BaCe0.9*M*0.1O3-δ (M Y, Yb, Sm, Tb, and Nd)", *Solid State Ionics,* 179(15), pp. 529-535.

(A-80)Münch, W., Seifert, G., Kreuer, K.D. & Maier, J., (1996) "Proceedings of the 10th International Conference on Solid State Ionics A quantum molecular dynamics study of proton conduction phenomena in BaCeO3", *Solid State Ionics,* 86, pp. 647-652.

(A- 81)Shimojo, F., Hoshino, K. & Okazaki, H., (1997) "First-Principles Molecular-Dynamics Simulation of Proton Diffusion in Sc-Doped SrTiO3", *Journal of the Physical Society of Japan,* 66(1), pp. 8-10.

(A-82)Mather, G.C. & Islam, M.S., (2005) "Defect and dopant properties of the SrCeO3-based proton conductor", *Chemistry of materials,* 17(7), pp. 1736-1744.

(A-83)Yamazaki Y, Blanc F, Okuyama Y, Buannic L, Lucio-Vega JC, Grey CP, Haile SM. Proton trapping in yttrium-doped barium zirconate. Nature materials. 2013 Jul;12(7):647.

(A-84)Hossain S, Abdalla AM, Jamain SN, Zaini JH, Azad AK. A review on proton conducting electrolytes for clean energy and intermediate temperature-solid oxide fuel cells. Renewable and Sustainable Energy Reviews. 2017 Nov 1;79:750-64.

(A-85)Yamazaki Y, Blanc F, Okuyama Y, Buannic L, Lucio-Vega JC, Grey CP, Haile SM. Proton trapping in yttrium-doped barium zirconate. Nature materials. 2013 Jul;12(7):647.

(A-86)Hossain S, Abdalla AM, Jamain SN, Zaini JH, Azad AK. A review on proton conducting electrolytes for clean energy and intermediate temperature-solid oxide fuel cells. Renewable and Sustainable Energy Reviews. 2017 Nov 1;79:750-64.

(A-87)Kobayashi, Y., Hernandez, O.J., Sakaguchi, T., Yajima, T., Roisnel, T., Tsujimoto, Y., Morita, M., Noda, Y., Mogami, Y. & Kitada, A., (2012) "An oxyhydride of BaTiO3 exhibiting hydride exchange and electronic conductivity", *Nature materials,* 11(6), pp. 507-511.

(A-88)Hayashi, K., Sushko, P.V., Hashimoto, Y., Shluger, A.L. & Hosono, H., (2014) "Hydride ions in oxide hosts hidden by hydroxide ions", *Nature communications,* vol. 5.

(A-89)Kobayashi, G., Hinuma, Y., Matsuoka, S., Watanabe, A., Iqbal, M., Hirayama, M., Yonemura, M., Kamiyama, T., Tanaka, I. & Kanno, R., (2016) "Pure H- conduction in oxyhydrides", *Science,* 351(6279), pp. 1314-1317.

(A-90) Hayashi, K. & Hosono, H. 2016, "Green apatites: hydride ions, electrons and their interconversion in the crystallographic channel", *Physical Chemistry Chemical Physics,* 18(11), pp. 8186-8195.

(A-91) Roy, M.K., Kawahara, N., Tomita, E. & Fujitani, T., (2013) "Jet-guided combustion characteristics and local fuel concentration measurements in a hydrogen direct-injection spark-ignition engine", *Proceedings of the*

Combustion Institute, 34(2), pp. 2977-2984.

(A-92) Fayaz, H., Saidur, R., Razali, N., Anuar, F.S., Saleman, A.R. & Islam, M.R., (2012) "An overview of hydrogen as a vehicle fuel", *Renewable and Sustainable Energy Reviews,* 16(8), pp. 5511-5528.

Appendix B

Evaluation of Green Paradox: Case Study of Japan

This appendix explains a social scientific topic which is known as Green Paradox. This paradox suggests that introducing renewable energy could accelerate the global fossil fuel consuming and emission of toxic gas. In this appendix, influence of the Green Paradox in Japan is evaluated whether it has taken place, or not.

B-1. Introduction

Our society has consumed fossil fuels and generated electricity to promote our economic growth. The amount of natural gas, coal/petroleum, and oil consumption known for typical fossil fuels accounted for over 80% shown in Figure.B-1[B-1]. The amount of consumption is estimated to keep growing up as shown in Figure B-2 [B-2]. When we take into account of the mining limitation, minable years as reserves-to-production (R/P) rate tends to decrease [B-3]. Although natural gas could keep supporting the demand of our society near future, the minable years will face the limitation in the long term.

Although the fossil fuels will be exhausted in the future, we could afford to keep consuming for several hundred years. However, what we have to consider is not the year when fossil fuels dried up, but when fossil fuels are mined with the largest amount. As long as we no longer increase the amount of mined fossil fuels, the economic growth will not be maintained because our society relays on the fossil fuels. Mohr *et.al.* suggest that the year when the amount of fossil fuels becomes the most so-called “production peak” of primary fossil fuels will come by 2025 [B-4]. Although the estimation is significantly earlier than reality, we will not be able to avoid the production peak in the future. Our economy is relying on the fossil fuels. Before the production peak comes, we need to build society which does not relay on fossil fuels. Otherwise our social situation depending on them will be very unstable.

It seems introducing renewable energy with solar power and wind power is the promising way for our future. The renewable energy does not directly emit harmful

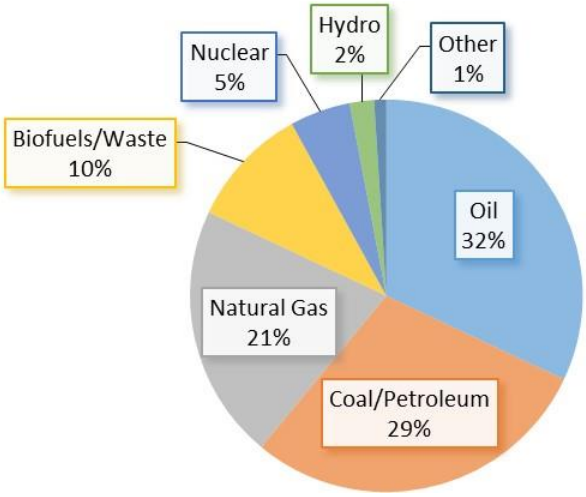

substance such as CO_2 which could lead to global warming [B-5]. Indeed, hydropower as a renewable energy could be increased to supply electricity in the future [B-6]. However, the amount will not be able to cover total energy demand for future due to the limited location for new installation sites.

Figure. B-1: World's fuel shares of total primary energy supply [B-1].

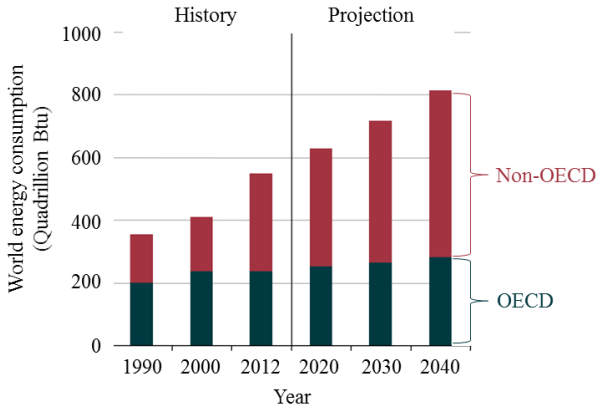

Figure. B-2: World energy consumption from 1990 to 2040(Estimated) [B-2]

Source: U.S. Energy Information Administration (May Oct 2016). Permission to reproduce is obtained by U.S. Energy Information Administration.

B-2. Hydrogen Society

These days, the usage of hydrogen as energy carrier has attracted attention because it is good at storing huge amount of energy. Combination of solar/wind energy and hydrogen can be a bright candidate to establish sustainable society because they can be combined as a closed energy cycle with water and hydrogen (,and oxygen in air) [B-7]. Figure. B-3 shows schematic system of society combined with fuel cells, water electrolyzers and renewable energy. This system is called “Hydrogen Society”, which is completely dependent on consumption of fossil fuels to obtain electricity.

However, the hydrogen itself currently has to be isolated or produced from other chemical compounds such as carbon hydride (C_xH_y). It is because producing hydrogen with water electrolyzers is much more expensive than fuel reforming with fossil fuels [B-8]. The amount of production of fossil fuels will begin to phase out after the production peak explained in introduction part. The system in Figure. B-3 to be substituted for our conventional energy supply with fossil fuels will be necessary. In fact, this system has already begun to be adopted to produce hydrogen by electrolyzing water to realize a sustainable society [B-9,10]. Recently, renewable energy markets, technologies, investment and policy frameworks have been rapidly developed. The ratio of global energy supplied by renewable energy in 2010 was 16.7%. The consumption has strongly increased year by year [B-11]. However, there are remaining issues for widespread utilization of renewable energy sources. For instance, the installation cost is expensive, and the amount of hydrogen which can be stored at a time is small. To overcome both issues, the success depends on the result of research and development. Especially,

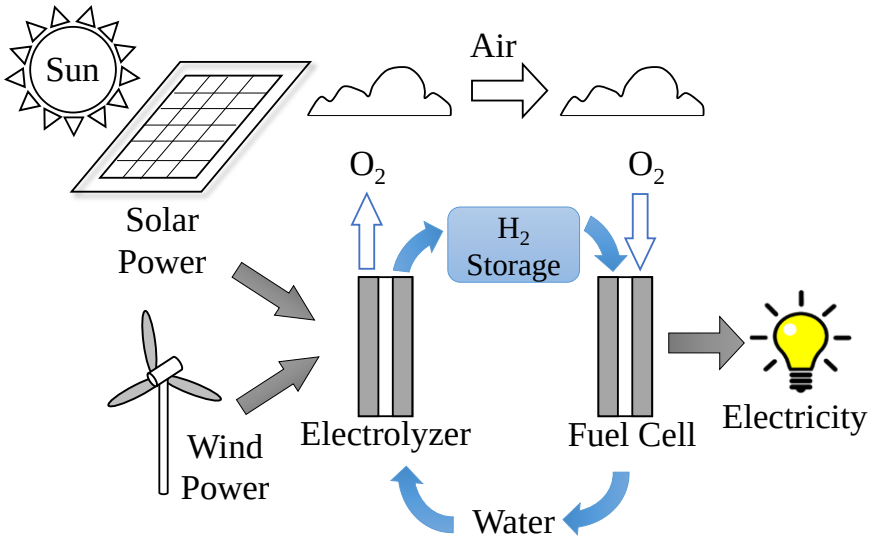

Japanese government has established the roadmap which is composed of three steps.

Figure. B-3: Schematic model of hydrogen society [B-12,13]

B-3. Roadmap for Hydrogen Society in Japan

Figure. B-4: Three phases to get out of dependence on fossil fuels in Japan [B-14]. Permission to reproduce is confirmed by Ministry of Economy, Trade and Industry of Japan.

To get out of dependence on the fossil fuels, Japan has energy policy to build hydrogen

society as shown in Figure B-3. It is composed of three phases as shown in Figure B-4. Firstly, it is to spread home-type fuel cell and fuel cell vehicle by 2020. Secondary, it is to make the hydrogen supply chain between Japan and other countries with unused hydrogen by 2030. Finally, with the supply chain and hydrogen from renewable energy, Japan will aim to get out of dependence on the fossil fuels by 2040 [B-14]. The above plan is really challenging because Japanese government also attempts to cover around 20 % electricity of Japan by 2030 with renewable energy. In short, still Japan will provide 80 % electricity with fossil fuels until 2020. If Japan follows above plan shown in Figure. B-5, Japan will be required to cover entire electricity demand by 2040 with renewable energy in 10 years from 2030. Such a rapid installation of fossil fuels, it may lead to accelerate the consumption of fossil fuels and the amount of emitted harmful substances due to the fossil fuel consumption, which is called “Green Paradox”.

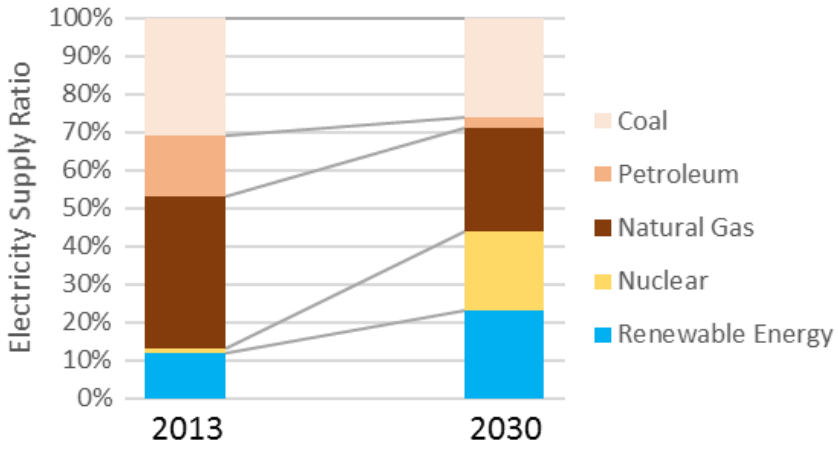

Figure. B-5: The component ratio for electricity supply between 2013 and 2030(Target Value) [B-15]. Permission to reproduce is confirmed by Ministry of Economy, Trade and Industry of Japan.

B-4. Green Paradox

According to Jensen *et al.*, the green paradox refers to an outcome in which climate

policies such as carbon taxes, which are aimed at reducing carbon emissions, instead have the opposite effect: emissions increase, at least for some period of time."[B-16]. Green paradox hypothesis comes to receive attention from 2008 when Sinn *et al.* pointed out [B-17]. Sinn *et. al.* suggest the mechanism that introducing renewable energy is likely to increase the amount of CO_2 emission as follows. As shown in Figure B-6, in case that the price of electricity in both country A and country B, companies in respective countries will not be affected by the electricity price. However, when country A actively introduces renewable energy, the price in the country A will increase. Therefore, companies in Country A will relocate factories to Country B. Thus, introducing renewable energy in specific country such as this Country A induces to have factories which used to be in country A increase the amount of CO_2 emission and shortage the term for minable years of fossil fuels in the world. This is the example of Green Paradox.

Because fossil fuels are finite, as long as we continue economic activity, the fossil fuels will be exhausted at some point in the future. Although we somehow need to seek the alternative energy resources and we have kept expecting renewable energy can be a promising, the Green Paradox suggests introduction of renewable energy does not have a positive effect. In addition, there is concern that people in the country where factories relocated are confronted with employment issue. What above Green Paradox insists is

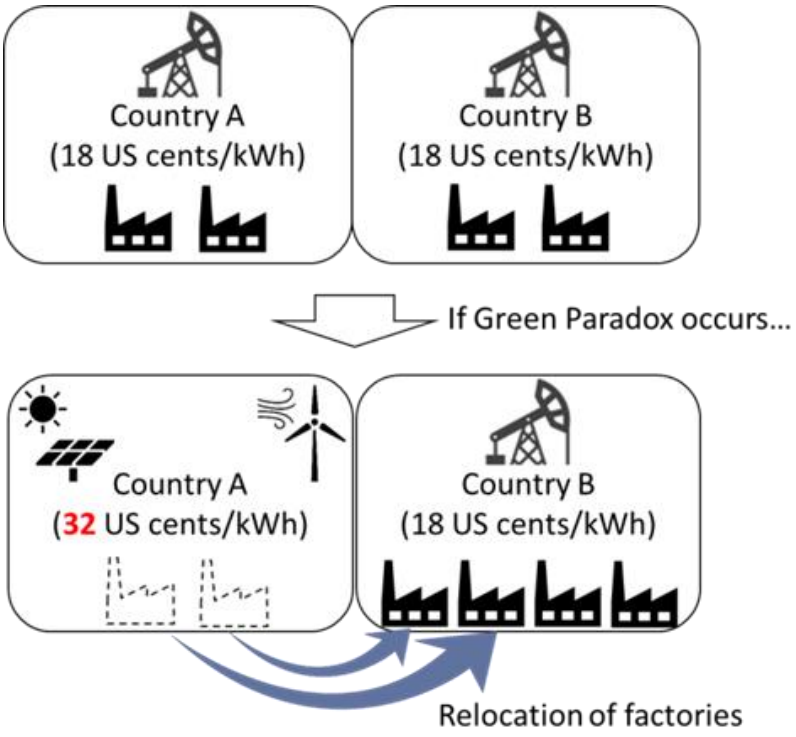

that introduction of renewable energy is not the suitable solution to reduce dependence on fossil fuels.

Figure B-6: The result of Green Paradox between Country A and Country B.

B-5. Literature Review

Before evaluation of the Green Paradox in Japan, this paper summarizes previous studies. As mentioned, the previous studies pointed out the cases consisting with Green Paradox hypothesis. In case of Ghana, previous research addressed the possibility that assumption of Green Paradox was realized. After refined oil subsidies finished from 2010, the import cost of oil rises. The result shows that the removal of subsidies on refined oil imports in Ghana would lead to the increase of CO_2 emissions in Ghana. This is an evidence of the Green Paradox [B-18]. In addition, in case of China, previous research addressed that the policy of central government prevents Green paradox, but that of local government does not prevent it. The previous research compares the emission of SO_2 to evaluate the amount of CO_2 emmision [B-19]. Furthermore, another research implies that Germany also occurs because the country increased the price of electricity to introduce renewable energy [B-20]. However, evaluation methods to clarify if Green Paradox occurs are not in common and unclear in several points. Therefore, in order to clarify Green Paradox in Japan, it is necessary to needs to establish advanced and sophisticated evaluation method.

B-6. Evaluation Method

Just a few reports related to the investigation of Green Paradox in each country have been published. Then, to examine whether Green Paradox occurs in Japan, this section explains the evaluation procedure for Green Paradox in Japan. As mentioned above, the Green Paradox refers to that introducing renewable energy eventually leads to increase the amount of harmful substances emission due to expensive electricity price and relocation of factories. This study collected following there types of data between 1996

and 2015 in Japan. The first is the amount of electricity price, the second is the renewable energy ratio in total electricity production, and the third is the trend in overseas production. All data obtained from Ministry of Economy, Trade and Industry, and Ministry of Land, Infrastructure, Transport and Tourism in Japan [B-20,21,22].

B-7. Results and Discussion

Table.B-1 summarizes the data for the amounts of electricity price, renewable energy ratio in total electricity production, and the trend in overseas production. Some data are missing because of lack of original data. It is considered that renewable energy introduction leads to electricity price, whose change cause eventually to move factories in Japan to move to other countries. From this analysis when the values of all indices increase in same year, it is seemed that Green Paradox occurs in Japan.

Figure B-7 shows the graphical data of summarized table1. In the three terms shown by red band (1996, 1999, and between 2012 and 2014) the price of electricity, ratio of renewable energy, and trends in overseas production ratio increased, suggesting that the Green Paradox may occur in Japan in that above three terms [B-20,21,22].

Because renewable energy is higher cost than conventional primary energy, it is thought that the increase in the ratio of renewable energy causes a bad influence on electricity charges. In addition, some Japanese industries say that raising the electricity price can be considered as a cause of overseas relocation. Therefore, these are phenomena are matching to the green paradox. In addition to the factors mentioned above, there seems to be other factors that affect each of them, but it can be proposed as one criterion for determining the green paradox.

Table B-1. Summarized data of trends in overseas production ratio, price of electricity, and ratio of renewable energy in Japan.

year	Trends in overseas production ratio (%)	Price of Electricity (JPY)	Ratio of Renewable Energy (%)
1965			0.109
1966			0.109
1967			0.112
1968			0.123
1969			0.132
1970		4.968	0.139
1971		5.089	0.143
1972		5.115	0.147
1973		5.328	0.156
1974		9.301	0.151
1975		10.276	0.145
1976		11.753	0.157
1977		12.955	0.159
1978		12.428	0.161
1979		13.114	0.179
1980		20.829	0.176
1981		21.295	0.176
1982		21.608	0.188
1983		21.586	0.201
1984		21.562	0.215
1985		21.908	0.221

1986		19.994	0.226
1987		18.695	0.238
1988		17.719	0.248
1989		17.152	0.260
1990		17.145	0.577
1991		17.327	0.582
1992		17.548	0.574
1993		17.536	0.570
1994	7.907	17.134	0.584
1995	8.259	16.943	0.612
1996	10.403	16.503	0.622
1997	11.049	16.749	0.634
1998	11.589	15.895	0.598
1999	11.393	15.468	0.613
2000	11.781	15.443	0.623
2001	14.319	15.457	0.609
2002	14.604	14.392	0.622
2003	15.579	14.075	0.641
2004	16.219	13.754	0.637
2005	16.734	13.512	0.674
2006	18.123	13.618	0.723
2007	19.055	13.655	0.679
2008	17.004	15.215	0.626
2009	17.041	13.768	0.613

2010	18.132	13.646	0.944
2011	18.004	14.592	0.960
2012	20.290	15.727	0.891
2013	22.889	17.525	0.916
2014	24.255	18.864	0.944
2015			0.970

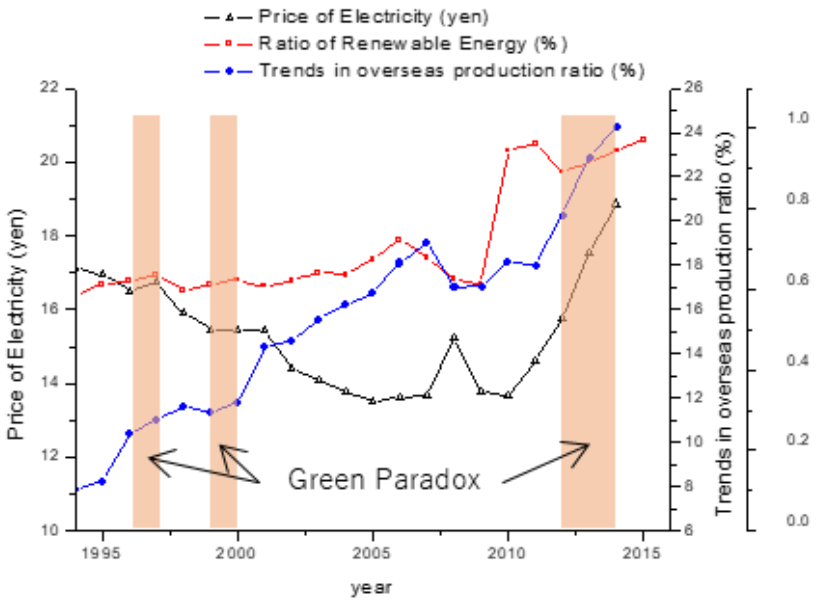

Figure B-7 Changes in electricity rates, introduction of renewable energy, overseas production ratio as function of year in Japan. Pale pink means the term that price of electricity, ratio of electricity, and trends in overseas production ratio increased simultaneously.

B-8. Conclusion

This study summarized previous paper evaluating several countries for the Green Paradox, and showed that there is no unified criteria to evaluate whether the Green Paradox occurs, or not. Then, this paper suggested novel criteria to determine if the Green

Paradox occurs in specific country. Form the viewpoints of electricity rates, introduction of renewable energy, overseas production ratio, Japan is also determined that Green Paradox occurred 3 times in 1996, 1999, and between 2012 and 2014.

References

(B-1) International Energy Agency (IEA): Key world energy Statistics (2015).

(B-2) Energy Information Administration, International Energy Outlook 2016, U.S. Department of Energy, May 2016.

(B-3) BP Statistical Review, June 2016.

(B-4) Mohr, S., Wang, J., Ellem, G., Ward, J. & Giurco, D., "Projection of world fossil fuels by country", *Fuel,* **141**, pp. 120-135 (2015).

(B-5) Karl, T.R., Arguez, A., Huang, B., Lawrimore, J.H., McMahon, J.R., Menne, M.J., Peterson, T.C., Vose, R.S. & Zhang, H.M., "CLIMATE CHANGE. Possible artifacts of data biases in the recent global surface warming hiatus", *Science,* **348**(6242), pp. 1469-1472 (2015).

(B-6) Zarfl, C., Lumsdon, A.E., Berlekamp, J., Tydecks, L. & Tockner, K., "A global boom in hydropower dam construction", *Aquatic Sciences,* **77**(1), pp. 161-170 (2015).

(B-7) Wang, C. & Nehrir, M.H., "Power management of a stand-alone wind/photovoltaic/fuel cell energy system", *IEEE Transactions on Energy Conversion,* **23**(3), pp. 957-967 (2008).

(B-8) Elam, C.C., Padró, C.E.G., Sandrock, G., Luzzi, A., Lindblad, P. & Hagen, E.F., "Realizing the hydrogen future: the International Energy Agency's efforts to advance hydrogen energy technologies", *International Journal of Hydrogen Energy,* **28**(6), pp. 601607 (2003).

(B-9) Cetin, E., Yilanci, A., Oner, Y., Colak, M., Kasikci, I. & Ozturk, H.K.,

"Electrical analysis of a hybrid photovoltaic-hydrogen/fuel cell energy system in Denizli, Turkey", *Energy and Buildings*, **41**(9), pp. 975-981 (2009).

(B-10) Yilanci, A., Dincer, I. & Ozturk, H., "A review on solar-hydrogen/fuel cell hybrid energy systems for stationary applications", *Progress in Energy and Combustion Science*, **35**(3), pp. 231-244 (2009).

(B-11) F. Orecchini, "The era of the energy vectors", *International Journal of Hydrogen Energy*, **14**(31), pp. 1951-1954 (2006).

(B-12) Mori, D., & Hirose, K.. "Recent challenges of hydrogen storage technologies for fuel cell vehicles", *International journal of hydrogen energy"*, **34**(10), pp. 4569-4574 (2009).

(B-13) O'hayre, R., Cha, S., Prinz, F.B. & Colella, W., *Fuel cell fundamentals*, John Wiley & Sons. p.22 (2016).

(B-14) Ministry of Economy, Trade and Industry of Japan "Points of reservation for roadmap of hydrogen and fuel cell strategy"

（http://www.meti.go.jp/committee/kenkyukai/energy/nenryodenchi_fukyu/pdf/002_01_00.pdf） （Access: March 31. 2017）

(B-15) Ministry of Economy, Trade and Industry of Japan, "Reform of policy for encouraging to introduce renewable energy"

（http://www.enecho.meti.go.jp/category/saving_and_new/saiene/kaitori/dl/kaisei/0628tokyo.pdf） （Access: March 31. 2017）

(B-16) Jensen, S., Mohlin, K., Pittel, K., & Sterner, T.. "An introduction to the Green Paradox: The unintended consequences of climate policies". *Review of Environmental Economics and Policy*, **9**(2), pp.246-265 (2015).

(B-17) Sinn, H.W., “The green paradox”, CESifo forum (Vol. **10**, No. 3, p. 10), 2009 October, Institut für Wirtschaftsforschung.

(B-18) Wesseh, Presley K., Boqiang Lin, and Philip Atsagli.(2016). "Environmental and welfare assessment of fossil-fuels subsidies removal: A computable general equilibrium analysis for Ghana." *Energy* **116** (2016): 1172-1179.

(B-19) Zhang, Kun, Zong-Yong Zhang, and Qiao-Mei Liang. "An empirical analysis of the green paradox in China: From the perspective of fiscal decentralization." *Energy Policy* **103**, pp. 203-211 (2017).

(B-20) Agency for Natural Resources and Energy “Section 4: Trends in Secondary Energy”

（http://www.enecho.meti.go.jp/about/whitepaper/2016html/2-1-4.html）（Access: May 19. 2018）

(B-21) Ministry of Land, Information, Transport and Tourism “Trend of Overseas Production Ratio (Manufacturing Industry)”

（http://www.mlit.go.jp/hakusyo/mlit/h27/hakusho/h28/html/n1113000.html）（Access: May 19. 2018）

(B-22) Agency for Natural Resources and Energy “Electricity price change”

（http://www.enecho.meti.go.jp/about/whitepaper/2016html/2-1-4.html）（Access: May 19. 2018）